AN EXPERIMENTAL AND THEORETICAL WORK ON THE SEISMIC BEHAVIOR OF A REINFORCED CONCRETE FRAME

CHRISTABEL AKOSUA S. OSEI AGYEMANG

IŞIK UNIVERSITY
2019

AN EXPERIMENTAL AND THEORETICAL WORK ON THE SEISMIC BEHAVIOR OF A REINFORCED CONCRETE FRAME

CHRISTABEL AKOSUA S. OSEI AGYEMANG
B.S., Civil Engineering, IŞIK UNIVERSITY, 2016

Submitted to the Graduate School of Science and Engineering
in partial fulfillment of the requirements for the degree of
Master of Science
in
Civil Engineering

IŞIK UNIVERSITY
2019

IŞIK UNIVERSITY
GRADUATE SCHOOL OF SCIENCE AND ENGINEERING

AN EXPERIMENTAL AND THEORETICAL WORK ON THE SEISMIC BEHAVIOR OF A REINFORCED CONCRETE FRAME

CHRISTABEL AKOSUA SAKYIWAA OSEI AGYEMANG

APPROVED BY:

Prof. Dr. Faruk Karadogan Işık University _____
(Thesis Supervisor)

Prof. Dr. Esin Inan Işık University _____

Prof. Dr. O. Cem Celik Istanbul Technik University _____

APPROVAL DATE: ..../..../....

AN EXPERIMENTAL AND THEORETICAL WORK ON THE SEISMIC BEHAVIOR OF A REINFORCED CONCRETE FRAME

Abstract

Corrosion of reinforcements embedded in concrete is one of the numerous causes of deterioration in reinforced concrete structures. In an earthquake prone region, corroded structures become more vulnerable to early failure within its life cycle.The major difficulty for experimental work on corrosion is related to the preparation of a naturally corroded specimens because it is time consuming hence accelerate corrosion is utilized in many researches. In this study, a 15 year old naturally corroded one storey one bay frame specimen and several standout cylindrical specimens were constructed using unseived sea sand containing seashells and to represent structures built during the rapid urbanization period in last 5 decades.

The specimen was tested under reversed cyclic loads and the test results were compared to results achieved previously with no corrosion. Furthermore, a numerical analysis was conducted by existing computer programs (SAP2000 and SeismoStruct) and a pushover algorithm was adapted considering lumped plasticity to obtain the structural response of the specimen by different techniques for two theories of analysis including an algorithm for determining stability loads and period at different states of plastic deformations. All numerical results were compared with the experimental results.

15 year old frame showed moderate corrosion at the lower ends of the columns with the lateral load capacity and ultimate displacement not extremely affected by the corrosion. However, higher energy dissipation capacity was observed and with low lateral stiffness at low levels of displacement. Aside the study on corrosion on the frame specimen, this thesis developed a correlation between Poisson's ratio and nonlinearity index β based on the gathered empirical data on the uniaxial compression test of 15 year old cylindrical specimens.

Keywords: Reinforced concrete Corrosion, Natural corrosion, Poisson's ratio, Cyclic loading, Nonlinearity index

AN EXPERIMENTAL AND THEORETICAL WORK ON THE SEISMIC BEHAVIOR OF A REINFORCED CONCRETE FRAME

Özet

Betona gömülen donatı korozyonu, betonarme yapılarda bozulmaların sayısız nedenlerinden biridir. Deprem eğilimli bir bölgede aşınmış yapılar yaşam döngüsü içindeki erken başarısızlığa karşı daha savunmasız hale gelir. Korozyonla ilgili deneysel çalışmalar için en büyük zorluk, doğal olarak aşınmış bir numunenin hazırlanması ile ilgilidir, çünkü zaman alıcıdır, dolayısıyla korozyonu hızlandırmak birçok araştırmada kullanılmaktadır. Bu çalışmada, 15 yaşında, doğal olarak aşınmış, bir katlı bir bölme çerçevesi numunesi ve birkaç kabartmalı silindirik numune, deniz kabukları içeren ve kullanılmamış deniz kumu kullanılarak ve son 5 yılda hızlı kentleşme döneminde inşa edilmiş yapıları temsil etmek için yapılmıştır.

Ayrıca, mevcut bilgisayar programları (SAP2000 ve SeismoStruct) tarafından sayısal bir analiz yapıldı ve numunenin stabilite yüklerini ve periyodu belirlemek için bir algoritma içeren iki analiz teorisi için farklı tekniklerle yapısal tepkisini elde etmek için yığılı plastisite dikkate alınarak farklı plastik deformasyon durumlarında bir itme algoritması uyarlandı.

15 yıllık çerçeve, yanal yük kapasitesine sahip kolonların alt uçlarında orta derecede korozyon ve korozyondan aşırı derecede etkilenmeyen nihai yer değiştirme göstermiştir. Bununla birlikte, düşük deplasman seviyelerinde daha yüksek enerji yayılma kapasitesi ve düşük yanal sertlik gözlenmiştir. Çerçeve örneğindeki korozyon çalışmasının yanı sıra, bu tez, 15 yaşındaki silindirik numunelerdeki toplanan emperyal verilere dayanarak Poisson oranı ile doğrusallık endeksi, β arasında bir kolerasyon geliştirilmiştir.

Anahtar kelimeler: Betonarme korozyon, Doğal korozyon, Poisson oranı, Döngüsel yükleme, Doğrusallık indeksi

Acknowledgements

First and foremost, I would like to thank the almighty God for the strength he granted me through out my thesis.

My deepest gratitude also goes to my supervisor, Prof. Dr. Faruk Karadogan for your patient guidance, time and effort you put in making me undertstand all the things you taught me through this journey. I say thank your for all the useful criticisms and encouragement throughout my research study.

My special thanks to Prof. Dr. Ercan Yuksel , Mr. Hakan Saruhan and the staff of the Structural and earthquake engineering laboratory of Istanbul Technical University in aiding me throughout out the test setup, testing and data collection during the experimental works.

I also wish to acknowledge PHD students, Mr. Ergun Binbir for his help in the experimental test and interperation of data and also Mr. Arasto for his heart warm help in the experimental work and advice in using SeismoStruct for theoritical analysis.

I wish to thank Prof. Dr. Esin Inan and the staff of the Civil engineering department of Isik University, including for their patience and encouragement during my thesis.
My gratitude to Isik University for the financial support to undertake experimental work in Istanbul Technic University.

Last but not the least, I would like to thank my family: my mother and sisters for the moral support and supporting me spiritually throughout writing this thesis.

To my family and friends

Table of Contents

List of Tables

List of Figures

List of Abbreviations

LVDT	Linear Variable Displacement Transducers
RC	Reinforced Concrete
PF	**P**article **F**iltering
CFRP	Carbon Fiber Reinforced Polymer
μ	Displacement ductility
$f_c^{'}$	Compressive strength of concrete
ξ_{eq}	Equivalent damping ratio
$\xi_{elastic}$	Elastic damping ratio
ξ_{hys}	Hysteretic damping ratio
θ	Bond slip rotation
β	Nonlinearity index
β_D	Nonlinearity index of the descending branch of stress strain curve.
ν_i	Initial Poisson's ratio
ν_f	Poisson's ratio at the ultimate stress
K_U	Unconfined corrosion specimen
E	Modulus of elasticity
$F^+{}_{j,max}$	Maximum positive lateral load of one cycle of same displacement
$F^-{}_{j,max}$	Maximum negative lateral load of one cycle of same displacement
$\Delta^+{}_j$	Maximum positive lateral displacement of one cycle of same displacement
$\Delta^-{}_j$	Maximum negative lateral displacement of one cycle of same displacement
$P^+{}_{max}$	Maximum positive lateral load
$P^-{}_{max}$	Maximum negative lateral load
$P^+{}_{Ult}$	Ultimate positive lateral load
$P^-{}_{Ult}$	Ultimate negative lateral load

δ	Structural lateral displacement
δ_{max}	Maximum lateral displacement
$\delta^-{}_{Ult}$	Ultimate negative lateral displacement
$\delta^+{}_{Ult}$	Ultimate positive lateral displacement
R_θ	Rotational stiffness
R_i	Rotational stiffness at node i
EI	Flexural rigidity
EI_{eff}	Effective flexural rigidity
L_P	Length of plastic hinge zone
$m_{i\theta_i}^{i-j}$	Moment at node i due to rotation at node i in member i-j
$m_{i\theta_j}^{i-j}$	Moment at node i due to rotation at node j in member i-j
$t_{i\theta_i}^{i-j}$	Shear force at node i due to rotation at node i in member i-j
$t_{i\delta}^{i-j}$	Shear force at node i due to lateral structural displacement of member i-j
C_e	Correction stiffness factors
g_e	Correction factor on geometric stiffness matrix
r	Rigidity factor
χ	Curvature
M_i	Moment at section i
M_u	Ultimate moment at section i
P_b	Buckling load parameter

Chapter 1

Introduction

1.1 Introduction

Five decades ago, unseived seasand was highly used as an aggregate in concrete mix composition in Turkey but seasand is known to have a high salt content which can induce initiation phase of corrosion at an early time ans also due to the smoothness of the aggregates it is known to cause a lower compressive strength in concrete. Corrosion of reinforcements in concrete has a detrimental effect on the structural response of reinforced concrete structures during its life cycle. The corroded reinforcements in concrete cannot be detected during the early stages of corrosion but if corrosion proceeds without control, it affects the serviceability and ultimate limit states of the structure. Formation of rust (corrosion product) has a volume higher than that of the original steel results in cracks and hence spillage. The entrance of carbon dioxide and chlorides are the two major causes of corrosion of reinforcement steel in concrete. Concrete has a natural ability to provide a passive layer for the reinforcing steel which breaks down once the presence of corrosion factors in the concrete are high enough to cause depassivation of the protective layer. Hence detrimental effects are initiated immediately active corrosion of steel occurs. The products of corrosion forms on the surface of the reinforcement, increasing the cross-sectional area of reinforcement. As expansions of the reinforcement occurs, it compresses the concrete causing tensile forces to

build up in the concrete, leading to crack formation on the surface of the reinforced concrete.

Many researches or studies has been made on corrosion and its effect on reinforced concrete structure. The conclusion drawn from these numerous studies show that corrosion affects the bond strength which in turn affects the strength of the whole structure, crack width, aesthetic, stiffness, the energy dissipation and load carrying capacity of concrete structure. Amry et al [1] concluded from a 40 year old corroded beam experiment that, 1% loss of cross-sectional area of the reinforcement reduces the load bearing capacity by 0.9% and beams with pre cracks had a low bond strength than corroded specimens without cracks. Jiang and Lui [2] reported that low axial compressive load reduces the lateral strength and the energy dissipation capacity.The strength and stiffness of the reinforced concrete structures can be reduced because corrosion affects the bond between concrete and reinforcing steel [3]. The bond loss is very difficult to study in the field so this causes it to be a major problem so it is rather studied from the cracks caused on the surface as a result of the corrosion

From various research done to discover the effect of the corrosion on the bond strength of affected RC structure, it is observed that the bond strength increases at lower levels of corrosion which is during the initiation phase. Irina [4] explains that the increase in bond strength between concrete and reinforcement steel attributes from the increase in bar diameter causing an increase in the radial stress hence increasing the friction and bond but after the surface cracks are formed the bond strength decreases since confinement of reinforcement is broken, leading to an aggressive attack by the agents of corrosion. She also concluded that other factors that affect the bond is also the transverse reinforcement and the ratio of cover to rebar diameter.

The Poisson's ratio of concrete is considered to be 0.2 in the ascending region of the stress strain curve before the peak stress. Very few studies have been done on Poisson's ratio of concrete on the descending branch of the stress strain curve relationship due to the severity of cracks which can create severe errors in data

collection. The study of Poisson ratio by Candappa [5] derived a correlation between nonlinearity index and secant Poisson's ratio of which he observed that the Poisson ratio of the descending branch is independent on the strength of the concrete.

Poisson's ratio of the post-peak branch of concrete is importatnt for retrofitting purposes. In CFRP wrapping retrofitting technique of concrete, the confinement pressure provided by the CFRP is affected by expansion of the concrete. Yeh etal [6] stated that the Poisson's ratio of concrete affects the confinement effect on concrete. As the confining pressure increases, there is an increase of compressive stress on the concrete causing internal cracks to develope in the concrete hence making Poisson's ratio no more a constant value because of an increase in lateral expansion.

1.2 Scope of this Research

Turkey is known to be one of the earthquake prone countries as seen in Figure 1.1. From various research on the investigations on the collaspe of exisitng builings in Turkey due to earthquakes like the 1999 izmit earthquake of magnitude 7.4 which caused a devastating collapse of major buildings (Figure 1.2) resulting in an awful loss of many lives, one of the common belief was corrosion due to the use of low strength concrete and the type of aggregate used.

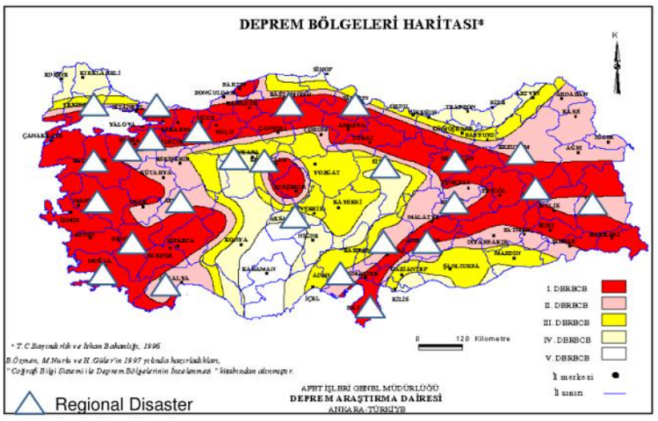

Figure 1.1: Turkish earthquake map

Figure 1.2: 1999 Izmit earthquake aftermath

In high seismic regions, such as Izmit, buildings can weaken as a result of corrosion of rebar and concrete strength degradation making the structure wide open to earthquake hazards.This study helps or contributes to the knowledge accumulated on the effects of corrosion on reinforced concrete structures. Many researches have been conducted for this same purpose but most are done on members (beam or columns) under accelerated corrosion and just a few has been made on naturally corroded reinforced concretes. However, there is no evidence of a research conducted on a naturally corroded frame which mimics the real response of in-situ buildings which brings me to the aim of this study.

The aim of this study is to investigate the effect of reinforcement corrosion on the structural performance on already existing buildings. Analytical models and

thoeritical works are developed to mimic the behaviour of the frame understudy.The results of this work can be used by engineers to assess the structural performance of existing structures and to help preseve the integrity and rehabilitation of existing old structures like historic buildings affected by corrosion and in seismic regions.

The aim is to obtain a model for the Poisson's ratio of the descending branch of the stress strain curve under uniaxial compressive loading.

1.3 Thesis Layout

In this present thesis, there are two topics being investigated. The effect of corrosion and the Poisson's ratio in the post peak region (also known as the strain softening regime) of the stress strain curve. Of these two topics, this thesis is sectioned into 4 chapters. Every Chapter covers both topics under different subchapters. Chapter 1 entails a brief introduction to the corrosion of Reinforced concrete and Poisson's ratio of the descending branch and the reasons for the investigation of these two topics.

Literature review is outlined in chapters 2. It covers the concrete composition and its contribution to corrosion, definition and process of corrosion, the types and phases of corrosion and known concrete stress-strain models. It also entails the literature review on the effect of corrosion on the bond and Poisson's ratio based on past research and conclusions drawn from their study.

The experiments are discussed in Chapter 3. It describes the types of specimens used and their strength, comparison of 28 day old concrete strength with 15 year old concrete specimen and Turkish earthquake code requirements, test setup, the instruments used for the testing and measuring, the loading protocols and the results of all tests performed. It also includes the comparison of experimental results with results from past research.

Chapter 4 covers the theoretical aspect of this thesis for both the 15 year old frame and the specimens tested for Poisson Ratio. The theoretical work for the Poisson

ratio, it includes the generated model for the stress strain curve of the concrete. Algorithm developed for the comparisions of pushover analysis is discussed in this chapter. Further discussion of the comparison of experimental works with theoretical works is done in this chapter.

Chapter 2

Literature Review

2.1 Concrete Composition

Concrete is composite material made up of aggregates and the cement paste. The cement pastes acts as a binder which constitute cement and water that literally sticks the filler together while the aggregates known as the filler maybe fine or course aggregates. The cement has the following major compounds Tricalcium silicate, Dicalcium silicate, Tricalcium aluminate, Tetracalcium aluminoferrite and Gypsum. When mixed together with water (H_2O) a hydration process begins which is the hardening of the concrete. This chemical reaction between the cement and the moleclues of water occurs to produce products of hydration plus hydroxide compounds. After the hydration of cement, the pH of the concrete increases above 12 because of the hydroxide (OH^-) ions in the pore solutions of concrete. In the pores of the concrete dense structure are soluble calcium, Ca, sodium, Na, and potassium, K, which reacts with the hydroxide ion to form hydroxides [7].

Concretes weakness in tension is dealt with by incoporating steel reinforcements to improve the tensile strength because it is known for its high ductility. In the next sections, corrosion of the steel in concrete will be discussed in details. In reinforced concrete, it is known that because of the high alkalinity, a protective passive layer of the release of alkaline hydroxide ions(Figure 2.1). Alkalinity is the opposite of acidity and steel in an acidic environment induces corrosion. This

passive film is a protective oxide layer of a few nanometres thick formed around the reinforcement and is composed of hydrated iron oxides with Fe^{2+} and Fe^{3+}, [8]. Water is an essential component in concrete. Nevertheless, the quantity of water is a factor that can affect the porosity of the reinforced concrete. High water to cement ratio causes high porosity, making it highly permeable which can decrease the strength.

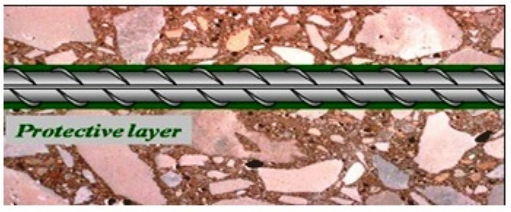

Figure 2.1: Protective layer on reinforcements provided by concrete

2.2 Concrete Stress-Strain Relationship Model

The stress strain responses of concrete for both confined and unconfined concrete will be discussed in this part of the literature review. several models have been suggested by various researchers amongst them are kent and park model, mander etal model, Kappos and Konstantinidis nonlinear concrete model, chang- mander model, Sheikh and Uzumeri and several others. In this study, we will elaborate on mander nonlinear concrete model.

The confinement of concrete is provided by the spiral or rectangular tie and cross ties. These reinforcements are known to influence the ductility of columns. Research shows that the more stirrups used, decreases the spacing, increases confinement hence increasing the ductility of the column.

2.2.1 Mander and Priestly

Mander proposed a model for both unconfined and confined concrete based on a modification of Popovics [9] expressions of the response of the stress and strain in concrete under compression. This model is suitable for both circular and rectangular column sections, monotonic or cyclic loading. This is illustrated in Figure 2.2. The modified popovics equations used in this model is given in equations 2.1, 2.2,2.3 and 2.4:

$$f_c = \frac{f'_{cc} \times \frac{\epsilon_c}{\epsilon_{cc}} \times r}{r - 1 + \frac{\epsilon_c}{\epsilon_{cc}}} \tag{2.1}$$

$$r = \frac{E_c}{E_c - E_{sec}} \tag{2.2}$$

$$E_{sec} = \frac{f'_{cc}}{\epsilon_{cc}} \tag{2.3}$$

$$\epsilon_{cc} = \epsilon_{co}\left[1 + 5\left(\frac{f'_{cc}}{f'_{co}} - 1\right)\right] \tag{2.4}$$

f_c ,ϵ_c is the compressive strength of concrete and its corresponding strain, E_c is the modulus of elasticity of conctrete ,E_{sec} is the secant modulus of confined concrete, ϵ_{co} is the strain of the unconfined concrete and its taken as 0.002.

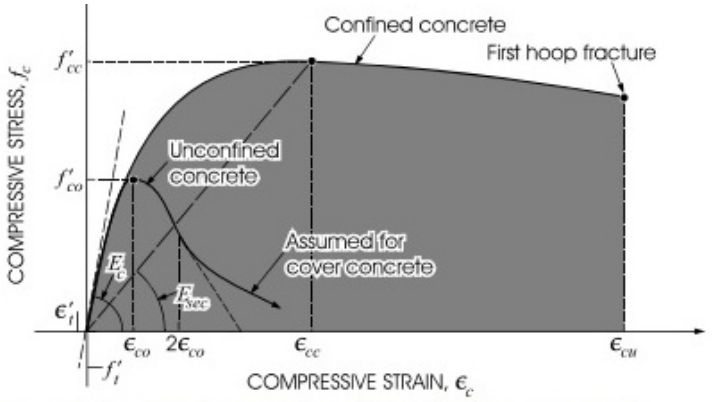

Figure 2.7b : Mander, Priestly, and Park Confinement Model

Figure 2.2: Manders proposed unconfined and confined concrete model

The lateral confining pressure was adopted from Sheikh and Uzumeris' research which explains that for both circular and rectangular stirrups, not all the core concrete is effectively confined. The ineffective part of the confined concrete acts at 45^o between two stirrups and forms and arch of a second order parabola. The effective confined core concrete has a lateral confining pressure defined by $f_l{}' = f_l \times K_e$. K_e is the confinement effectiveness coefficient. K_e for rectangular and circular hoops are given in mander etal [10]. f_l is the lateral confining stress on concrete.Mander later verified this model by performing experiments.

2.3 Corrosion of Steel Reinforcement in Concrete

Corrosion in reinforced concrete is an electrochemical process which occurs when corrosion agents penetrate the concrete cover to the rebar. Corrosion of concrete is successful when there is availability of electrochemical potential and this arises when [11];

- The surface of the steel embedded in the concrete is different or the presence of two different metals in the concrete [11].

- There is concentration of cells because of the variability of dissolved ions throughout the concrete [11].

The two electrochemical reactions in equations 2.5 and 2.6 are called the anodic and cathodic reactions in the anode

$$Anode: \quad Fe \rightarrow Fe^{2+} + 2e^{-} \tag{2.5}$$

$$Cathode: \quad 1/2O_2 + H_2O + 2e^{-} = 2OH^{-} \tag{2.6}$$

The two main factors of corrosion are chlorides and carbon dioxides in the presence of moisture (electrolyte) and oxygen in the concrete. These factors do not alter the electrochemical reaction given above. Once corrosion occur, the iron in the steel dissolves in the pore solution producing electron ions.

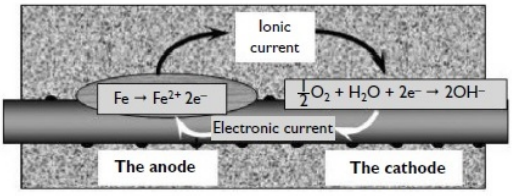

Figure 2.3: Mechanism of corrosion in reinforced concrete

For maintenance of electrical neutrality, these ions must be consumed elsewhere on the steel that is the cathode region. The cathode reaction is only possible in the presence of water (humidity) and oxygen (dissolved oxygen molecules). It produces the hydroxide ions. This process creates an electronic current as seen in Figure 2.3.

Once excessive mode of transport occurs, depassivation gradually occurs and corrosion product begins to form on the rebar surface. The reactions that lead to the formation of rust of the surface of reinforcements is outlined in equation 2.7, 2.8and 2.9.

$$Fe^{2+} + 2OH \rightarrow Fe(OH)_2(Ferroushydroxide) \tag{2.7}$$

$$4Fe(OH)_2 + O_2 + 2H_2O \rightarrow 4FeOH_3(Ferrichydroxide) \tag{2.8}$$

$$2FeOH_3 \rightarrow Fe_2O_3.H_2O(HydratedFerrichydroxide(rust)) + H_2O \tag{2.9}$$

The mode of transport can be either by capillary action and diffusion. Carbonization causes general corrosion but chloride induce corrosion causes pitting corrosion. This will be explained in details in the following section.

2.3.1 Carbonation Induced Corrosion

Carbonization is the process where carbon dioxides in the surrounding environment ingress the concrete and react with the compounds present in the pore solution. Carbon dioxide in a moist environment reacts (dissolves) with water molecules to form an acid. The pore solution in concrete contains soluble substances as stated above. They form hydroxide compounds like $Ca(OH)_2$ in the pore solution. The pore solution is concentrated with soluble hydroxide compounds. Once the acid is formed in the moist environment, it neutralizes the pore solution in a chemical reaction 2.10

$$CO_2 + H_2O \rightarrow H_2CO_3 \quad H_2CO_3 + Ca(OH)_2 \rightarrow CaCO_3 + 2H_2O \tag{2.10}$$

another neutralisation reaction can occur directly 2.11.

$$Ca(OH)_2 + CO_2 \rightarrow CaCO_3 + 2H_2O \tag{2.11}$$

Equations 2.11and 2.10 produces the same products but one occurs when the hydroxides dissolve in the carbon dioxides directly and the other when the environment is moist. The calcium carbonate ($CaCO_3$) produced is insoluble and neither a base nor an acid so it reduces the pH of the pore solution to about 9. Carbonization is a slow process based on [7]:

- The impermeability of the concrete : when the $CaCO_3$ are formed in the pores they begin to crystallize in the pore since they are insoluble, rendering the concrete impermeable.
- The low concentration of carbon dioxides in the air – the global average concentration of CO_2 is 400 parts per million by volume (ppm). This make the process slow.
- The reserve of hydroxides : due to the above reasons, CO_2 will be limited for the dissolution of the hydroxides in the pore solution

According to Bertolini [12] ,carbonization, on the other hand can occur rapidly if;

- the concrete cover is very small: With a thin concrete cover, the time of transport of the ingressed CO_2.
- well connected pores: rate of ingress of carbon dioxide increases.
- limited alkaline products: when the alkaline product mention above in the pores are limited the ingress of CO_2 becomes very high. limited alkalinity can result in the rapid breakdown of the protective passive oxide film. The limited alkalinity occurs either when the cement content is low, so during hydration there will be limited reserve of the alkaline reaction products, also when high water to cement ratio, increase porosity hence increasing permeability, and when curing is done poorly.

2.3.2 Chloride Induced Corrosion

Years before 1950, carbonation was the dominant cause of corrosion [13] but currently chloride induced corrosion is observed to be dominant cause of corrosion in chloride containing environments like sea water. Chlorides can enter into the

concrete by so many ways. In the production of concrete, chlorides can introduced by adding accelerator, using sea water as a binder and chloride containing aggregates. And way to chlorides can diffuse into a structure is indirectly which includes wetting and drying cycles, sea salt spraying or immersing it in sea water, de-icing salts etc. Chloride induced corrosion are more dominant in coastal regions.

Mode of transport of chloride ions starts with capillary action when the concrete is immersed in water and diffusion occurs. Unlike carbonization, there is a front and reaction, chlorides penetrate though the concrete easily through pore networks or micro cracks making corrosion more aggressive. The passive film on the embedded reinforcement is formed due to the alkalinity of the pore solution. In carbonization, this passive film becomes unstable when the pore solution is neutralized, but in chloride induced corrosion there is no neutralisation hence no drop in the pH level of the pore solution. Hussein [14] shows that the broke down of the passive layer is depends on the ratio of chloride concentration to hydroxyl concentration.

Once the passive layer is broken down the chlorides move to the steel and reacts with the iron. The type of corrosion normally observed in chloride induced corrosion is pitting corrosion.

2.3.3 Phases of Corrosion

The service life of a corrosion prone reinforce concrete structure can be categorized in two stages namely the initiation and propagation phase [15]. Initiation phase is the stage at which the quantity of corrosion product on the surface of the rebar is small to commence corrosion (partial depassivation) and the propagation phase is stage where rebar corrosion occurs after the passive oxide layer is permeated (steel depassivation) shown in Figure 2.4).

Intiation Phase

This phase is where corrosion agents (Cl or CO_2) penetrate the concrete cover, but its quantity is not enough to initiate corrosion. Corrosion is a slow process but

when the reinforced concrete is constructed with chloride containing component of concrete (like admixtures, salt water, aggregates) the initiation phase occurs for a short period of time.

i) Carbonization initiation phase : the ingress of CO_2 is gradual. the alkalinity of concrete is high but CO_2 neutralizes the pore solution to a pH to about 9. The reason behind this is concrete pore solution contains some soluble substance like CaO, Na_2O, K_2O as stated above. These produce base compound (ie, $Ca(OH)_2$, NaOH AND KOH) with the hydroxyl ions in the pores of concrete. $Ca(OH)_2$ compares to the other hydroxides has a limited solubility [7]. Once carbon dioxide diffuses into the concrete, $Ca(OH)_2$ is neutralised (equation 8).$CaCO_3$ is neither acidic nor basic. This neutralizes the pore solution hence making the passive oxide film unstable.

ii) Chloride induced initiation phase : The ingress of chlorides is unlike carbon dioxides. Accordiong to tuutti [7], when chloride concentration is high in the surrounding environment of the concrete compared to the pore solution, there is a gradual increase in the concentration in the pore solution. during the initiation phase the ingress of chloride can be increased by the wetting (rain) and drying (sunny) of concrete.

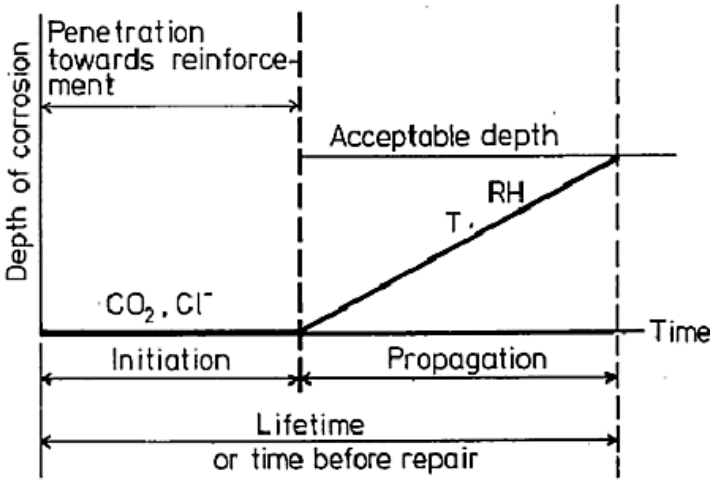

Figure 2.4: The service life of reinforced concrete model [7]

Propagation Phase

The gases or liquids are enough to breakdown the protective passive film to initiate corrosion, cracking and spalling of concrete cover. In the presence of water (humidity) and oxygen, the corrosion can start. Corrosion occurs when the iron in steel is oxidized. The iron oxide has a low strength and ductility and also has a low density compare to the steel. The corrosion products (iron-oxide) have lower density compared to a pure metal, causing radial stresses to be exerted on surrounding concrete, resulting in damage to the concrete ,which is explained in the reactions noted in the above chapters. Carbonization brings about general corrosion which occurs all over the entire surface and causing longitudinal cracks along the surface of the concrete while chloride induced corrosion causes pitting corrosion (not all over the reinforcement).

According to tuutti [7], "The general corrosion becomes particularly noticeable at very high OH concentrations since high chloride concentrations are not capable of giving rise to pitting". The common corrosion product in RC is rust (Fe_2O_3) which is insoluble. The volume is approximately 2 - 6 times that of solid steel.The concrete cover thickness and its permeability property determines how the concrete can resist the ingress of chloride.

2.4 Corrosion

Corrosion is a naturally occurring gradual process as explain in chapter (2). To determine the influence of corrosion on the structural or mechanical performance on existing structures, laboratory test must be performed. Corrosion in Reinforced concrete is one of the hot topics in structures. It is quiet difficult to determine the level of corrosion in an already existing structure. Majority of the research conducted on corrosion are based on accelerated corrosion performed in the lab. Concrete is the most popular construction material with river sand (fine aggregate) as the well known component. Sea sand has been used as a substitute of river sand in most of the Asian regions. As evident in earthquake damaged

buildings in Avcilar- Istanbul, after the 1998 Ceyhan-Adana earthquake, sea sand was used in the construction of the buildings.

Figure 2.5: Seasand as aggregates with large amount of sea shells - 1999 Izmit earthquake

Sea sand is more economical as compared to river sand. The effect of sea sand on reinforced concrete will be discussed in this section and how corrosion is induced by this sea sand.

2.4.1 Seasand as a Fine Aggregate

The demand for river sand is high making the price exorbitant hence the use of sea sand. Sea sand unlike river sand has shells and the aggregates have smooth surfaces and also known for its high salinity(alkalinity) and if not treated before used for construction purposes; it can lead to problems in the structural integrity. Sea water is known to be high in chloride and sodium ions [16]. Sea sand used in concrete has a low compressive strength as compared to normal concrete. Mehendran [17] using concrete cubes observed that when 100% river sand was replaced the

percentage decrease was 10.5% but when 50% sea sand was used, 6.24% decrease in the compressive strength however the tensile strength and flexural strength are not affected that much as compared to the compressive strength. Çağatay [18] research on the other hand shows more than 50% decrease in the compressive strength. This difference can be attributed to mix proportions used nevertheless both research concludes that sea sand results in low compressive strength compared to river sand. The presence of chloride content can accelerate corrosion of reinforcement. The presence of chlorides may cause swell, precipitate, sulphate and other adverse consequences.

Corrosion as discussed above can negatively affect structural durability. The standard threshold amount of chloride present in aggregate is 0.2% by weight to prevent corrosion[18]. Once corrosion is above the threshold, localized corrosion or general corrosion can occur which can affect the bond between concrete and reinforcement and also decrease the effective reinforcement bar size. Sea water is usually absorbed by the aggregate and in the process, the salts my get deposited in the porous microstructure of the aggregate, which ultimately cannot be removed by physical treatment completely.

2.4.2 Effects of Corrosion on Bond

Past studies have indicated that corrosion has a good effect on RC at the onset of corrosion but once corrosion cracks begins to form on the surface of concrete, corrosion rate escalates due to the easy access of corrosion agents to the surface of the rebar. Previous studies have observed that corrosion goes a long way to affect the durability of RC members, the strength, stiffness, energy dissipation ability and the load carrying capacity which will be discussed in details. These effects are linked to the bond deterioration and bond loss at the interface of concrete and reinforcement once corrosion is initiated. FIB [3] stated that the strength and stiffness of the reinforced structure can be reduced because corrosion affects the bond between concrete and reinforcing steel. Concrete is known to be weak in tension hence the reinforcements which are used in the tensile zone to take care of

the tensile stress developed in the concrete. The bond formed between concrete and reinforcement can be either mechanical interaction, fiction or chemical adhesion as stated in section 2. A study by Yafei et al [19] concludes that the bond between concrete and the reinforcement differ by the reinforcement type (plain or deformed). Plain reinforcement is mainly by frictional force and deformed is by mechanical interaction and they affect the bond deterioration in different ways. During corrosion, the formation of the resulting product on the surface of the reinforcement is about 2-3 times larger in volume than the pure steel. The products formed on the surface of the reinforcements exerts radial compressive stress causing the concrete to be in tension hence increasing friction [4]. Studies by Yafei et al [19], observed that at low corrosion level, the friction coefficient increases to 2-3 times that of uncorroded reinforcements. Once the tensile strain of the concrete is exceeded, corrosion cracks extend to the surface of the concrete. Before these cracks are observed, studies by various researchers say that al low levels of corrosion, the bond strength at the interface of the concrete and reinforcement increases [4], [19], [20], [21].

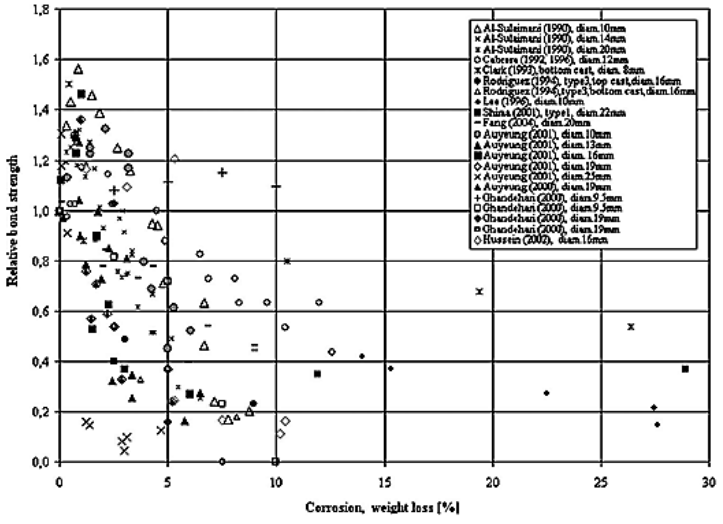

Figure 2.6: Bond strength deterioration by various researchers[4]

Plain bars of 18 mm diameter, at low levels of corrosion (1.62%), increases in bond

stress at about 83.1% as compared to uncorroded rebars [19]. In deformed rebars, at corrosion loss of 3.27%, the bond stress increase 17% compared to the uncorroded reinforcements. Lundgren's studies [21] also shows that uncorroded specimen that do that exhibit cracks during pullout test, shows an increase in bond strength when the reinforcements are corroded but once cracks are observed the bond strength decreases. This is because the expansion of the reinforcement literally means rebar diameter increases hence the raidial stress developed increases the friction and the bond. When the cracks are observed the bond strength decreases because of the energy release by the corrosion cracks [19]. The corrosion products weakens the bond between the steel and concrete which can leave the reinforcements as the only element to bear the loads. The repercussion is low serviceability and performance of structures. The factors that influences bond deterioration are the corrosion rate, the ratio of concrete cover to bar diameter.

2.5 Poisson's Ratio Of Concrete

Poisson's ratio being one of the mechanical properties of concrete will be studied in this present research. It is defined as the ratio of the transverse stain to the longitudinal strain. Considering the stress strain curve of concrete, many research has been done about the Poisson's ratio of pre-peak region but very little has been done on the post peak region. The current study is about the Poisson's ratio at the post peak region/ the softening region of the stress strain curve of both plain concrete. The research articles found on the Poisson's ratio of concrete related to this study will be discussed here.

Candappa [5] generated a correlation between the nonlinearity index and the secant Poisson's ratio of the descending branch of the stress strain curve of confined concrete. By using the constitutive model generated by Ottosen (1969) which defines the relationship between the nonlinearity index and the secant Poisson ratio of concrete. The model is presented in equations 2.12 & 2.13.

$$\nu = \nu_i \qquad when \qquad \beta \leq \beta_1 \tag{2.12}$$

$$\nu = \nu_f - (\nu_f - \nu_i)\sqrt{1 - \left(\frac{\beta - \beta_1}{1 - \beta_1}\right)^2} \qquad when \qquad \beta > \beta_1 \tag{2.13}$$

where β is the nonlinearity index, ν_i is the Poisson's ratio at the initial stages, ν_f is the Poisson's ratio at the ultimate stress as shown in Figure 2.7.

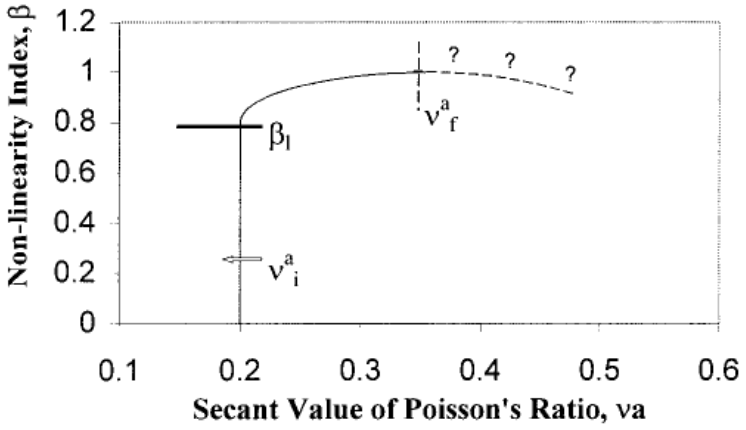

Figure 2.7: Ottosens model for relationship of β and ν [5]

The nonlinearity index is defined as the ratio of the axial stress to the ultimate stress. This model is limited to the failure point when nonlinearity index is higher than 1. For trilinear stress strain curve, the correlation Candappa [5] generated between the nonlinearity index β_D and secant Poisson's ratio of the descending part of the curve is given in equation 2.14.

$$\beta_D = -0.5(\nu)^2 + 0.45\nu + 0.9 \tag{2.14}$$

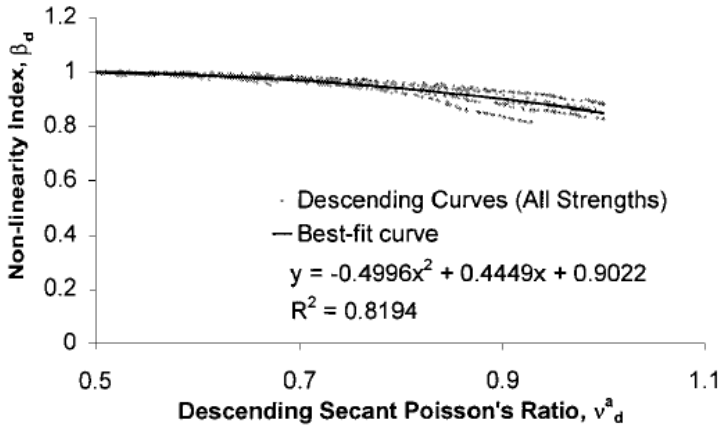

Figure 2.8: Relationship of β_D and ν [5]

Candappa [5] concluded that the uniaxial strength of concrete does not have an effect of the post-peak region of the nonlinearity index vs the secant Poisson's ratio at low levels of confinement.

Jinlong Pan [22] came up with a cracking Poisson's ratio which quantiies the damage in concrete when cracks form on the concrete by considering the three stages which are (1)linear stage- from the onset of loading to 30% ultimate load capacity. At this stage, the cracks are defined as bond cracks between mortar and aggregates. This zone was considered the elastic zone and the Poisson ratio was taken as constant. (2) Nonlinear stage – occurs within 30% to 70% / 90% ultimate strength. Bond cracks enlarge and propagate but does not decrease the strength. The Poisson ratio for this stage which is defined by Jinlong et al [22] a cracking Poisson ratio is expressed as a second order polynomial shown in equation (3) post- failure stage - from 90% of ultimate strength till failure. The crack in this stage are visible on the surface.

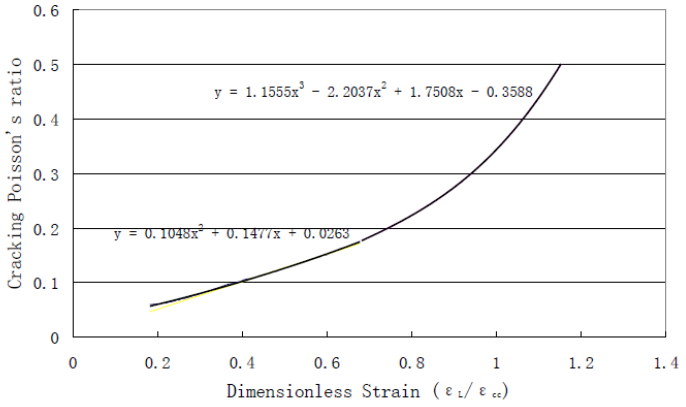

Figure 2.9: Relationship of β_D and ν [22]

Through curve fitting, he proposed a model shown in Figure fig:ottosen1 but it does not account for the descending branch of the stress-strain curve. Since less research is done on the Poisson's ratio of descending branch of the stress strain cruve, one of the aim of this study is to derive a correlation between nonlinearity index and the Poisson's ratio of concrete for uniaxial compressive stress.

Poisson's ratio of the post-peak branch of concrete is importatnt for retrofitting purposes. In CFRP wrapping retrofitting technique of concrete, the confinement pressure provided by the CFRP is affected by expansion of the concrete. Yeh etal [6] stated that the Poisson's ratio of concrete affects the confinement effect on concrete. As the confining pressure increases, there is an increase of compressive stress on the concrete causing internal cracks to develope in the concrete hence making Poisson's ratio no more a constant value because of an increase in lateral expansion.

Chapter 3

Experiments

3.1 Specimens

This present study is based on an experiment conducted in an earthquake laboratory of Istanbul technical University in 2003. Several frame specimens and corresponding cylindrical standard sized were cast and most were used for the study of retrofitting. Five of the frames were left to go undergo corrosion under natural conditions and the cylindrical specimens were stored indoors. The experimental study on seismic behavior of existing structures was conducted on three of theses 15 year old one-bay one-story 1/3 scale bare frame. It should be noted that this frame was constructed using unseived sea sand containing seashells and mild steel to reinforce the specimen to represent most of the vulnerable existing structures built during the rapid urbanization period in last 5 decades.

Based on past research by Pinar [23], this frame was constructed to portray the weak column -strong beam analogy used in still existing structural buildings which was a habitual way of construction in Turkey before the Turkish earthquake code of 1997 became effective.

The aim is to study the compressive strength, deformation capacity and Poisson ratio of the descending region on the stress strain curve of concrete cylinder specimens after 15 years of casting and the load bearing capacity, stiffness degradation, energy dissipation and damping capability of the 15 year old frame subjected to

cyclic lateral displacement reversals while under uniform axial loading from fictitious upper story. In this chapter, only the experimental results obtained from one frame specimen will be discussed and compared with a previous research carried out on a bare frame [23] since the same frame was used in that study with a smiliar displacement protocol.

3.1.1 Material Characteristics

The concrete composition and mix proportions are expressed in weight per cubic meter outlined in the table A.2. The density of the concrete is approximately $22KN/m^3$. The test on three unconfined standard cylindrical (150 mm $\times$ 300 mm) concrete specimens were performed after 28 days of casting. The corresponding compressive stress-strain diagram obtained after the test is shown in Figure 3.4(a). Properties of the longitudinal reinforcement obtained 15 years ago from a tensile test performed using Amsler machine of 200 KN capacity is shown in Table 3.2.

Concrete composition (kg/m^3)	
Mix component	
Concrete	300
Water	140
Sand	690
Gravel	1070

Table 3.1: Concrete composition, [23]

Mechanical properties of reinforcement			
Diameter	ϕ16	ϕ10	ϕ6
Yeild strength,f_y	270	290	325
Ultimate Strength, f_u	420	450	481
Ultimate Strain, ϵ_u	0.25	0.3	0.35

Table 3.2: Reinforcement mechanical properties, [23]

3.1.1.1 Concrete

In existing buildings, the concrete strength can be determined by either hammer test or by concrete core extraction which is suggested by TSC [24] or ultrasonic pulse velocity. Considering this frame, nine cylindrical concrete core samples of 93 mm diameter shown in Figure 3.3 were drilled at various positions from the frame after the experiment. Before the extraction, a pachometer shown in Figure 3.3(b) was used to locate the position of the reinforcement to prevent drilling into the reinforcements. The standard length to diameter ratio(slenderness ratio) of a cube and cylinder are 1 and 2 respectively, since the core concretes L/D ratio was less, an extrapolation was needed. An estimated in-situ compressive strength of cubic concrete was calculated according to BS1881 [25] by the formula as follows:

$$estimated\, in-situ\, cubic\, strength, f_{c_{cube}} = \frac{D}{1.5+\alpha} * f_{c_{concrete}} \tag{3.1}$$

D is 2.5 for cores drilled horizontally or 2.3 for cores drilled vertically and α is the inverse of length to diameter ratio (D/L). The compressive strength of the standard size cylinder is approximately 0.8 of the compressive strength of the cube (BS1881 [25]). Figures 3.5(a) & 3.5(b) represents the compressive stress strain curves obtained from the computed estimated compressive strength of the extracted core samples, mean compressive stress and the corrected mean compressive strength using manders formula. In the the stress strain curves, the assumed strain corresponding to the ultimate compressive stress and the failure strain are 0.002 and 0.005 respectively. The mean value was corrected by the tolerance factor method obtained by ACI 214.4R-10 [26], which is given in Table 3.3 assuming that the probability of obtaining a test with strength less than f_c is less than approximately 10%. K is the correction factor which depends on the number of specimens and the confidence level. Figure 3.1 shows possible correction factors accoring to the american standard. The correction factor, K was taken as 1.28 based on past research [27].

Extraction point	**core**	**L/D**	**Compressive Strength (MPa)**	
			Tested core	Cylinder 150 × 300
Column	I	1.14	24.99	22.34
	II	1.04	25.27	21.84
	III	1.11	27.79	24.58
	IV	1.12	26.10	23.16
Beam	I	1.17	24.21	23.90
	II	1.10	31.56	30.33
slab	I	1.15	28.79	28.21
	II	1.10	28.03	26.93
	III	1.11	27.12	26.16
Average (MPa)				25.27
Standard deviation, St.dev (MPa)				2.85
corrected Strength ($f_{c,avg} - K \times St.dev$) **(MPa)**				21.63

Table 3.3: Data on extracted core concrete and tested compressive strength

	Confidence level		
n	75%	90%	95%
3	2.50	4.26	6.16
4	2.13	3.19	4.16
5	1.96	2.74	3.41
6	1.86	2.49	3.01
8	1.74	2.22	2.58
10	1.67	2.06	2.36
12	1.62	1.97	2.21
15	1.58	1.87	2.07
18	1.54	1.80	1.97
21	1.52	1.75	1.90
24	1.50	1.71	1.85
27	1.49	1.68	1.81
30	1.48	1.66	1.78
35	1.46	1.62	1.73
40	1.44	1.60	1.70

Figure 3.1: Concrete strength correction factors,K [26]

3.1.1.2 15 year old Unconfined Standard Concrete Specimen

Three cylindrical specimens of the same material characteristics as the frame under study were cast in 2003 with a slenderness ratio (l/d) of 2. All specimens were tested under uniaxial compressive forces, but they vary based on the type of load control. K_U-1 , where K means corrosion, the subscript U signifies unconfined concrete and 1 is the specimen number,was tested with Besmark equipment where the loading parameter was force controlled, Table 3.4. The two remaining

specimens, K_U-2 & K_U-3, were tested with an Instron equipment under displacement control having a loading capacity of 4900 KN. The rate of loading of the specimen was 0.3 mm/min.

Linear variable transducers (LVDT's) were used as the displacement measuring instrument for deformations in both the axial and lateral directions. Two symmetrically positioned LVDT's for axial strain and three LVDT's positioned at 120^o apart in contact with the central zone of the concrete. The stress strain

Specimen	**Load Control**
$K_U - 1$	force
$K_U - 2$	displacement
$K_U - 3$	displacement

Table 3.4: Type of Load control performed on 15 year old cylindrical specimens

curves in Figure 3.6(a) represents the experimental data of three 15 year old unconfined cylindrical specimens. The experimental strain data accumulated for the first specimen, K_U-1, was not reliable since it displays a high scatter of strain data, although the ultimate load was achieved. This can be attributed to the fact that the control parameter was force and also confirms the conclusions made by past researchers. Therefore, force controlled test is utilized when only the

Figure 3.2: Uniaxial compressive Cylindrical test setup and measuring instrument

ultimate stress is demanded. Due to this, with the attained ultimate stress, the stress strain curve for K_U-1 was obtained by the proposed manders unconfined concrete model, assuming the strain corresponding to the ultimate stress is 0.002. The ultimate stress obtained for K_U-1,K_U-2 and K_U-3 are 30.5, 21.49 and 31.0 MPa,repectively, having a mean value and standard deviation of 27.66 MPa and 5.35 MPa. The mean value was corrected by the standard deviation correction factor of 1.28.

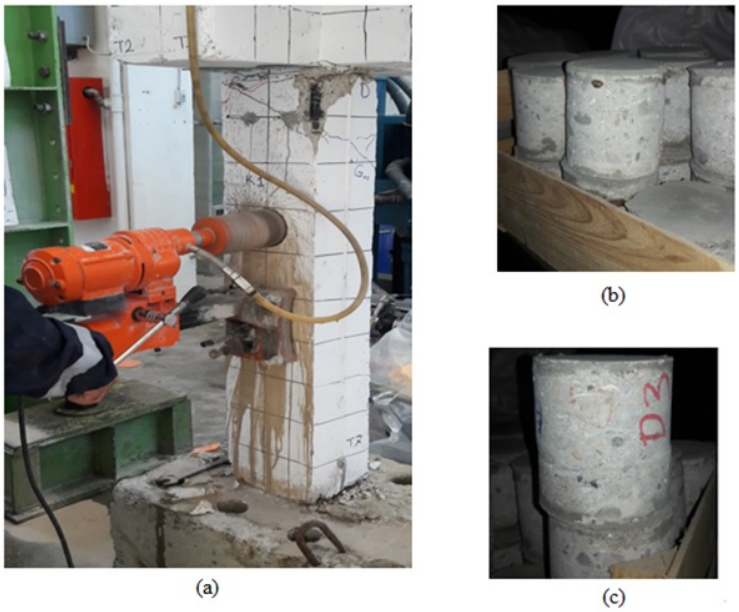

(a)

(b)

Figure 3.3: (a) Extration of core by drilling; (b) core specimens with capping; (c) Pachometer

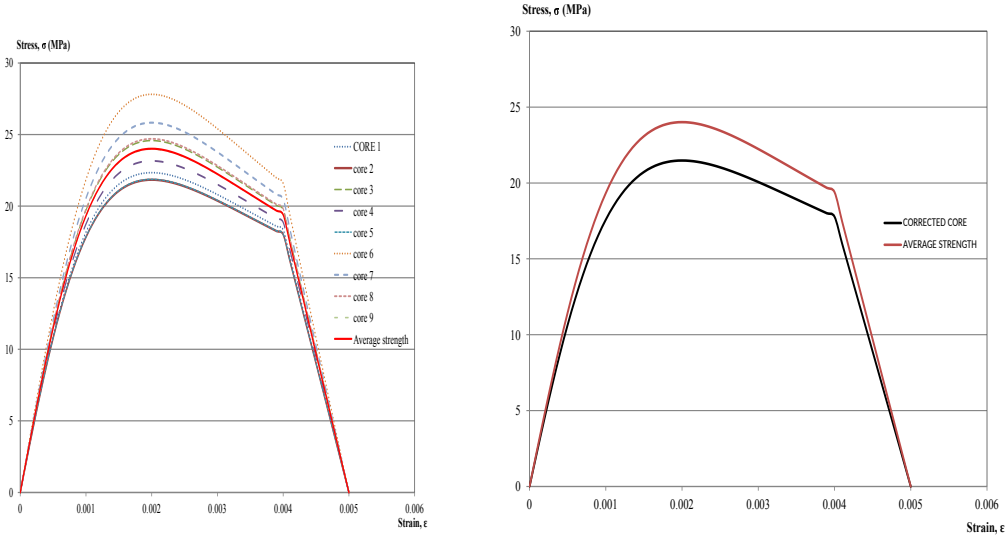

(a) Frame core specimens

(b) core specimens mean and corrected mean strength

Figure 3.5: Stress- Strain relationship of extracted concrete cores

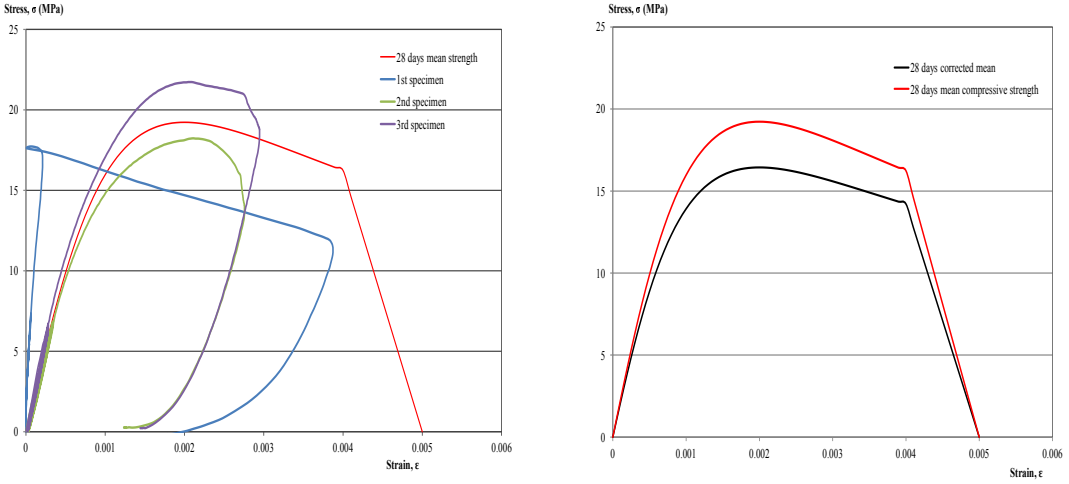

(a) 28 days cylinder specimen

(b) 28 days mean and corrected mean strength

Figure 3.4: Stress- Strain relationship of 28 day cylinder specimens

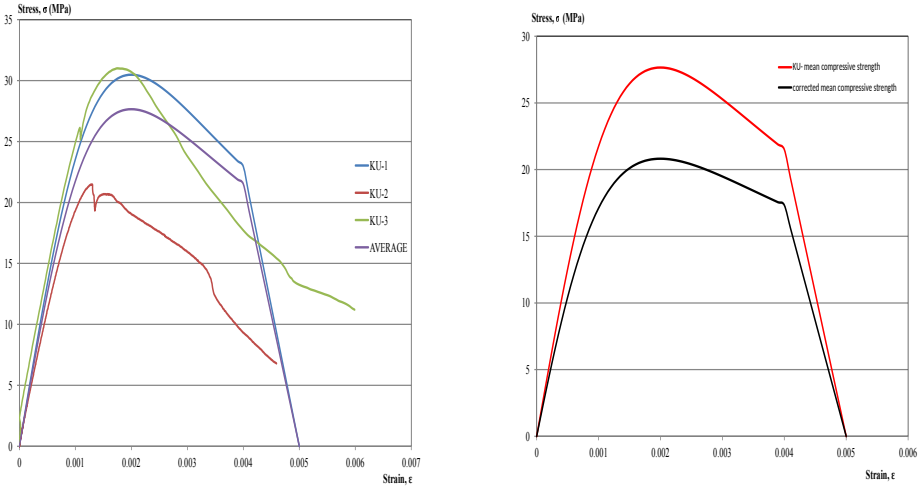

(a) 15 year old specimens

(b) mean and corrected mean strength

Figure 3.6: Stress- Strain relationship of 15 year old concrete cylinders

3.1.1.3 Comparision of Results of Core and Standard Cylinders

As mention earlier, core extraction is used to determine the compressive strength of in-place (existing) structures. In this section, a comparision of parameters like

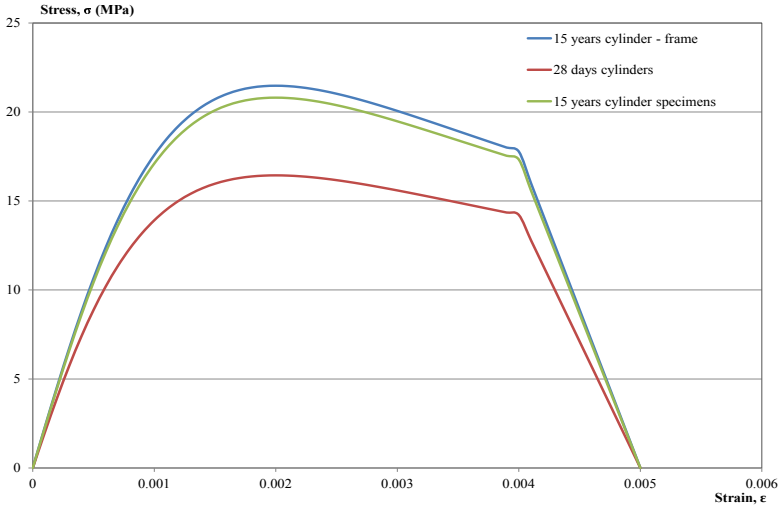

Figure 3.7: Comparision of corrected compressive strength

the modulus of elasticity, E, and the compressive strength (stress) of concrete will be discussed. Comparing the results of the standard sized cylinder with the test results of the core concrete samples , the observations were the average of the estimated cylinder strength of the core specimen test results is 25.71 MPa and the average of the standard cylinder is 27.66 MPa. The stress- stain curve is represented in Figure 3.7. The cylinder strength of the core is approximately 13% lower compraed to the standard cylinders, meaning the it is 86% of the standard cylinder test. Accordnig to ACI [26], the average of three core specimens must be higher than $0.85f'_c$ and individually higher than $0.75f'_c$, hence the compressive strength of the core samples is acceptable. This decrease might be attributed to the damages caused during drilling.

Considering the 15 year old standard cylinder specimen and the 28 days standard cylinder test, the average compressive strength is 27.66 MPa and 16.4 MPa respectively. Over 5475 days (15 years), the compressive strength of the concrete is approximately 68.65% higher therefore with age there is always strength development. Within the scope of our knowledge, concrete is known to increase in strength rapidly with days until about 56 days and then with months and years the growth of age increases more slowly. Also considering the modulus of elasticity, which is a factor for estimating the deformation of structural elements and also known to be proportional to the square root of the compressive strength of concrete according to TS500 [28], the modulus of elasticity for 28 days specimen is 27161 MPa while the 5475 days old specimen is 31092 MPa which is approximately 14% higher.

To conclude, age causes the development of the compressive strength of concrete and the modulus of elasticity. Concrete extracted core samples aid in the estimation of the compressive strength of existing structures.

3.1.1.4 Reinforcements

Plain longitudinal reinforcements were used in this experiment and no lap splice from column to foundation. Eight of 50 cm length reinforcements were extracted

after the damage of the frame. After extraction of the reinforcement, it was observed that the minimal to no corrosion had occured. In other words, the protective layer was not totally breached. The samples were taken from the column.

The nominal diameters of the reinforcements were calculated and used in the

Diameter	$\phi 16$
Yeild strength,f_y (MPa)	313
Ultimate Strength, f_u (MPa)	426
Fracture Stress, f_u (MPa)	376
Fracture Strain, ϵ_f	0.34

Table 3.5: Mechanical properties of the corroded longitudinal reinforcements

tensile test experiment. Amsler equipment of 200 kN tension capacity was used in the tensile test of the reinforcement. The corroded longitudinal reinforcements were tested until the facture point. The mechanical properties of the corroded reinforced obtained from the test is shown in Table 3.5.

3.1.2 Geometry and Reinforcement Detailing of Frame Specimen

The corroded frame under study is one a bay, one story which consists of all parts of a beam (precisely a T-beam) and columns. The column cross-sectional dimension is 200 by 250 mm and the T-beam has a flange width of 820 mm and a height of 120 mm and its web has a dimension of 200 by 205 mm. The span of the beam is 1950mm from the column centreline and the height of the column is 1417.206 mm from the centroid of the T-beam. Geometry of the frame is given in Figure 3.11.

The reinforcement detailing for both column and beam is shown in Figure 3.11. The arrangement of longitudinal reinforcement along the height of the column is not symmetric. Columns longitudinal reinforcements extend into the foundation without a lap splices. The total longitudinal reinforcement ratio is 16%. Single beam reinforcement is extended into the column until almost half of the column height. Pinar [23] stated that this specimen was built on a weak column strong

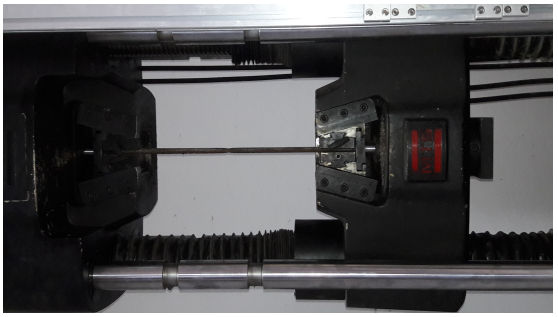

(a)

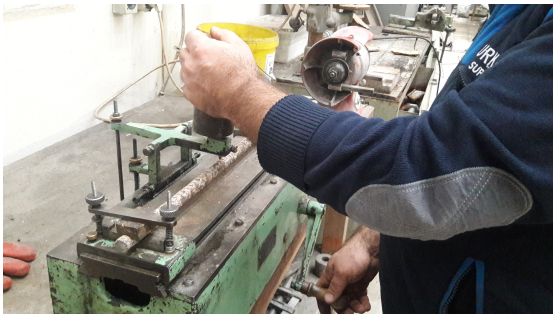

(b)

(c)

(d)

Figure 3.8: Test setup of reinforcments

beam notion to represent building constructed before the 1982 turkish earthquake code was enveloped. This is obvious from the arrangement of stirrups in the column in Figure 3.10.

3.2 Test Setup

3.2.1 Frame

The specimen is tested under cyclic lateral displacement while simultaneously being subjected to a constant axial load. The test setup is illustrated in Figure 3.11. Lateral load was issued to the specimen by an MTS hydraulic Actuator of $\pm$250 KN and $\pm$300 mm capacity by displacement control which was connected on the beam level together with a rod to ensure the load reversals were transferred all over the frame. A steel beam was placed on the frame with pinned support on the columns to transfer only axial forces to the column.

The constant axial force applied on each column was 172 kN. (20% of axial capacity of the column + half of a load from steel beam). The 20% axial capacity was issued by another steel beam mounted on a adjustable hydraulic jack to regulate the amount of axial load transferred to the columns. The axial loads onthe column is the equivalent of assumed loads transfered from the upper storey. The specimen was fixed to an adapter foundation with 21ϕ38 anchorage bolts through a 50mm hole to prevent any rotation or displacement of the foundation (fixed support).

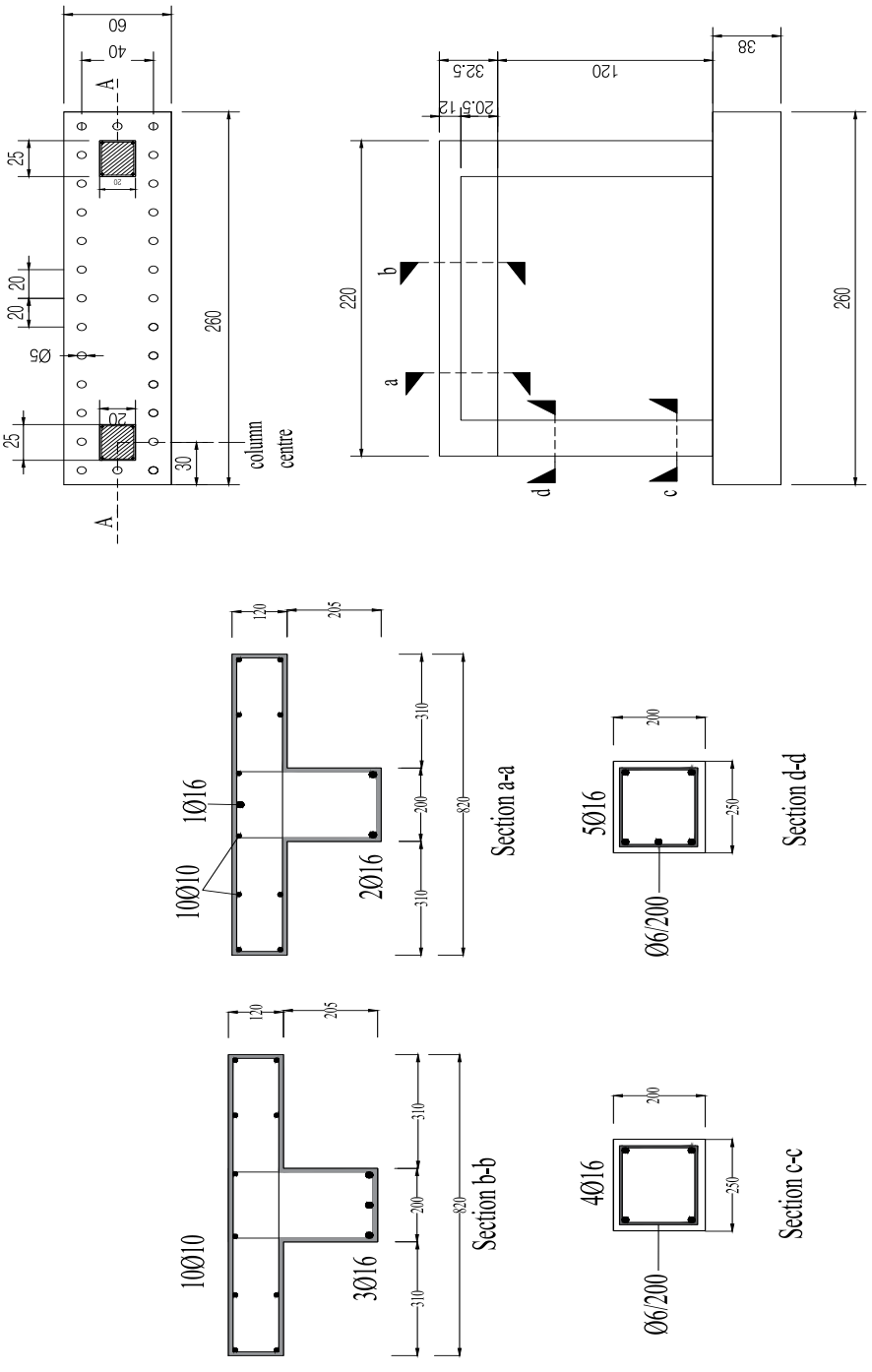

Figure 3.9: Frame dimensions and detailing

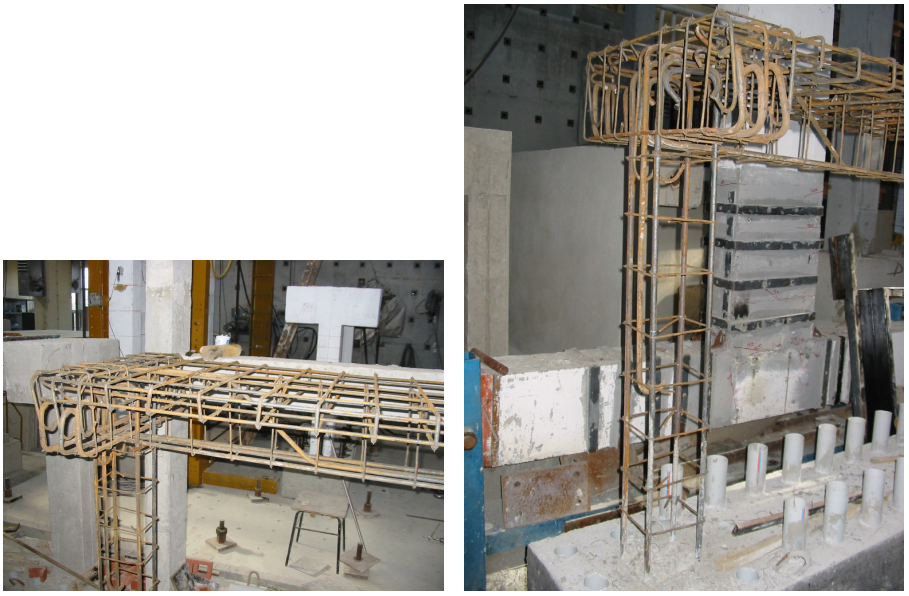

(a) (b)

Figure 3.10: Reinforcement detailing

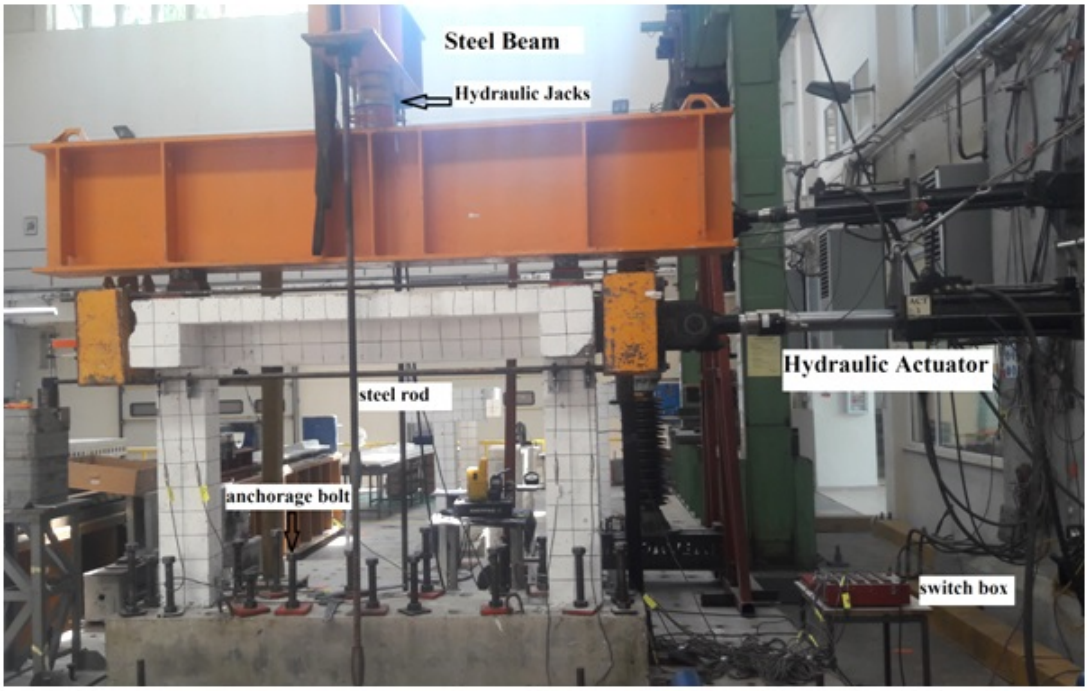

Figure 3.11: Test setup for Frame specimen

3.2.2 Specimens for Expansion Ratio Test of the Post-Peak Branch of the Stress Strain Curve

In the study of the Poisson's ratio of the descending branch of the stress strain curve, three specimens will be considered. They are standard cylindrical unconfined concrete specimens of over 5475 days old. The concrete cylinder specimens are 150 mm in diameter and 300 mm in height. The mix proportions of the cylinder specimen is the same as the frame specimen prepared 15 years ago.

The testing of the cylindrical specimens were done by Instron with a loading capacity of 4900 kN force. The test setup is shown in Figure 3.12. Three linear variable displacement transducers, LVDT's were positioned at 120 degrees apart supported by a magnet and perpendicular to the specimen to record the lateral deformation occured during the experiment. A load cell was used to measure the force transfered to the specimen and between the load cells and the specimen are steel plates, to ensure uniform distribution of the force to the upper and lower surface of the specimen. To record the axial deformation, two LVDT's mounted on magnets to prevent disturbance were placed parallel to the specimen at 180 part and perpendicular to the steel plate. The specimen were tested under displacement control for both the pre-peak and post peak regions of the stress strain curve with a loading rate of 0.3 mm/min.

Figure 3.12: Uniaxial compressive Cylindrical test setup and measuring instruments

3.3 Instrumentation - Frame Specimen

The instruments used in the test were linear variable displacement transducers (LVDT) and a crack width ruler, Figure 3.15. 12 LVDTs' were fixed to the specimen with the help of anchorages fixed with epoxy in a hole drilled in the specimen at specific positions to avoid contact with the reinforcement. Table 3.13 provides specific functions of each LVDT placed. Figures 3.14 and 3.16 shows the positions of the LVDT on the specimen (units in cm).

NAME	FUNCTION	TYPE OF LVDT
T1	Top displacement of the structure	SDP 100
T2	Top rotation of the column	CDP 10
T3	Top rotation of the column	CDP 10
T4	Top rotation of the column	CDP 10
T5	Top rotation of the column	CDP 10
T6	Bottom rotation of the column	CDP 10
T7	Bottom rotation of the column	CDP 10
T8	Bottom rotation of the column	CDP 10
T9	Bottom rotation of the column	CDP 10
T10	Displacement of whole system	CDP 25
T11	Out of plane displacement	CDP 25
T12	Out of plane displacement	CDP 25

Figure 3.13: Functions of LVDT's

The LVDT was in contact with a glass shown in Figure 3.14 which is placed on the specimen with epoxy to provide a level surface for correct measurement. The initiation point of the LVDT's was the mid-stroke position to account for the measurements in both loading and unloading of the cyclic displacement loading pattern. These measuring instruments were connected to a switch box connected to the control room to record all the data in this experiment.

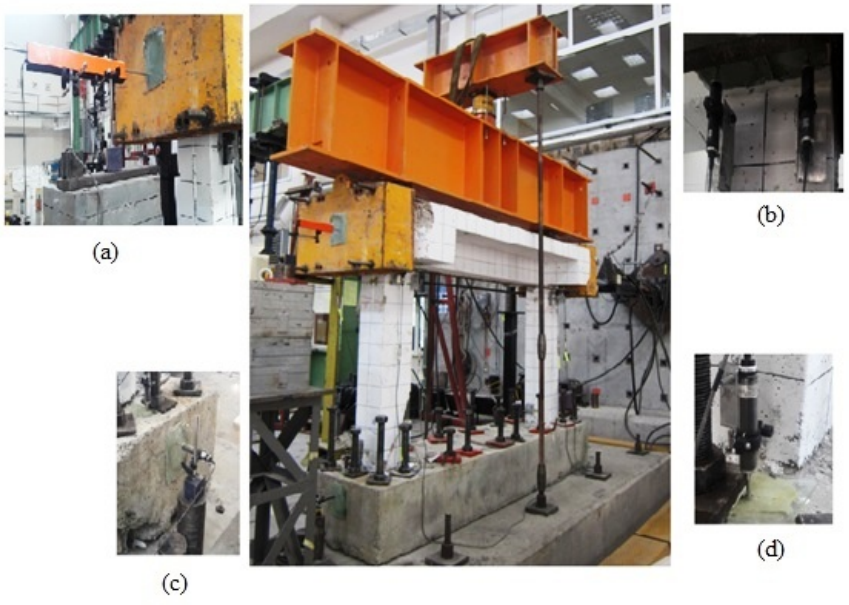

Figure 3.14: LVDT's on the frame

Figure 3.15: Crack width measuring card

3.4 Loading Pattern - Frame (Displacement Protocol)

Loading histories of structure are selected based on earthquake ground motion records. The two widely known ground motions are far field / fault ground motion and near field ground motion. These ground motion records (ground shaking) is expressed as ground acceleration, displacement and velocity of the ground surface as function of time. When an earthquake occurs, its effects on structures vary. The parameters used to define an earthquake are amplitude and frequency. These parameters change according to the enormity of the earthquake, the soil type, the rapture mechanism, fault geometry and direction and the topography of the land [29].

The seismic wave reduces in amplitude as it phases through soil or rocks. Hence the severity of damage to structures close to the fault. The structural response of near fault ground motion is normally small excursions followed by a very large excursion after which smaller excursions are observed. Krawrinkler [30], suggested that a monotonic loading (lateral load increments) should be considered to include the big excursions in the near field ground motion but for far field ground motion a stepwise cyclic loading should be used.

The type of loading used in this present study is displacement reversals of cyclic loading. This is to mimic the behaviour of earthquake in real life. The displacement protocol used in researches is either to mimic far field or near field earthquake effects of the loading history of the specimen. The displacement protocol

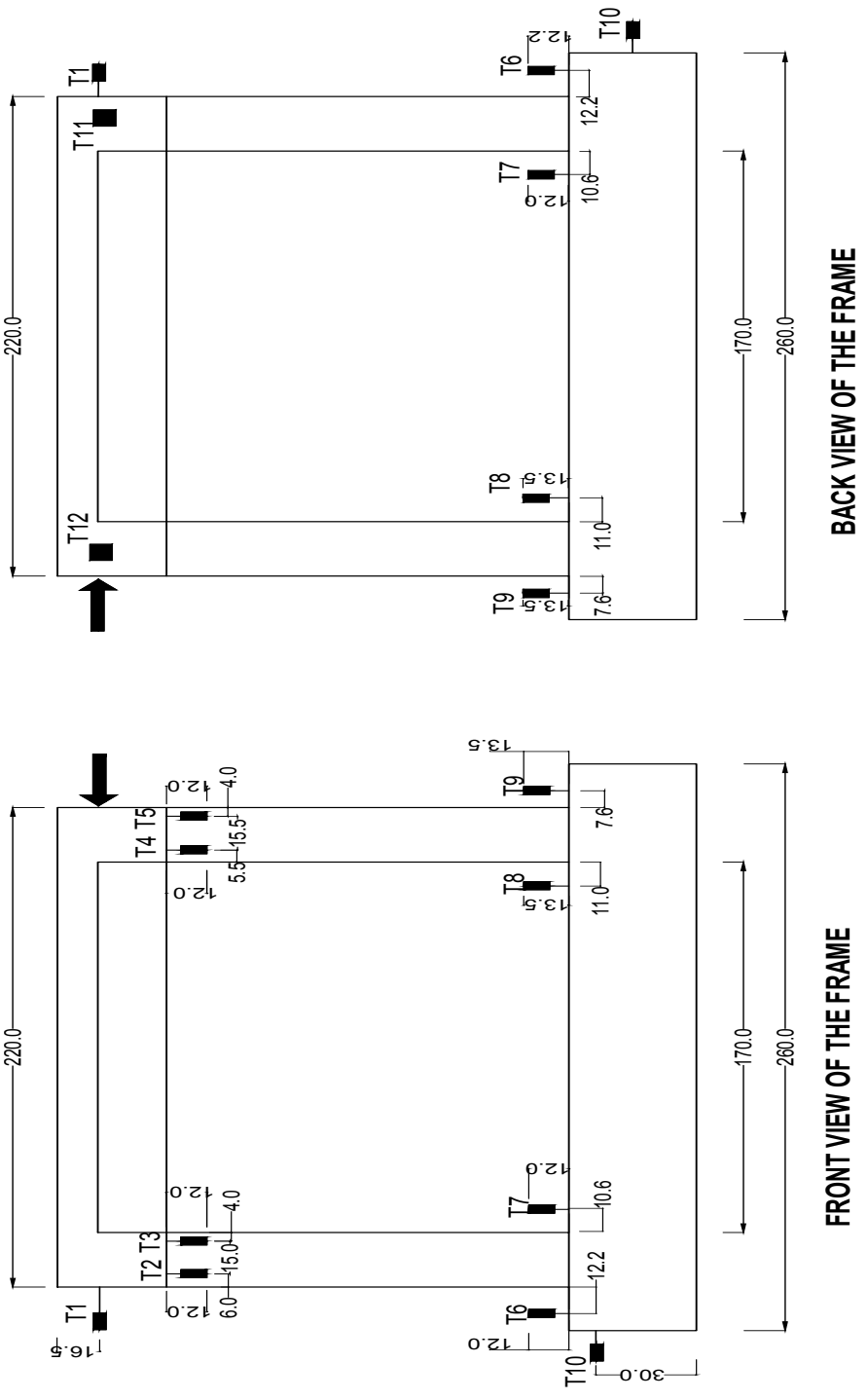

Figure 3.16: Location of LVDT's

given in Figure 3.17 is to represent a far field earthquake effect on the specimen in this present study. Wei-Jian Yi, also uses a similar loading to signify far field earthquake effect unlike PEER 2002 [31], where the displacement reversal begun with a pulse.

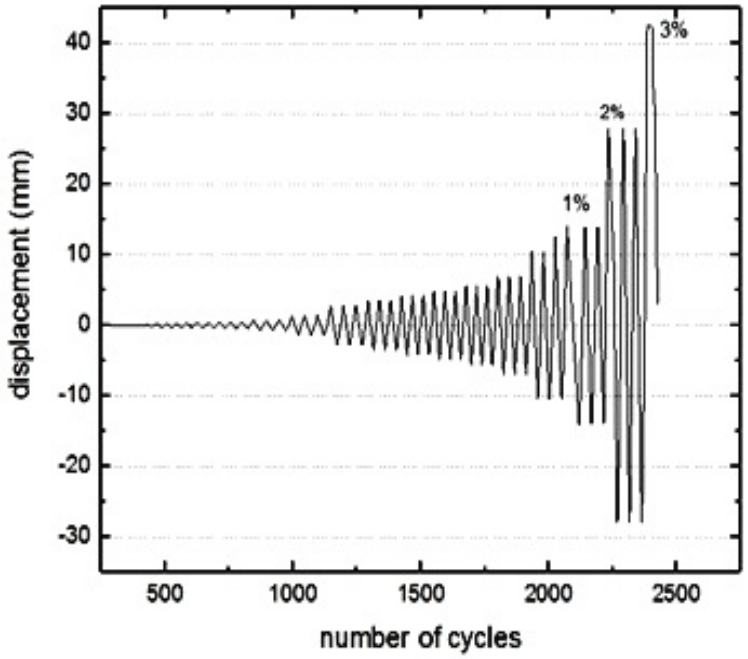

Figure 3.17: Loading Cycles

The displacement of the frame was based on storey drift which is the ratio of lateral displacement to frame height as suggested by Krawrinkler. Both positive and negative target drift was used to complete one cycle. The target drifts used in this experiment is given in Figure 3.18. For every target drift, three cycles were applied as illustrated in Figure3.17, to observe the stiffness and strength degradation of specimen under each displacement. An MTS hydraulic actuator of ±250 kN and ±300 mm was used. The highest drift introduced was 3%. According to TSC [24], the acceptable drift is 2% of the storey height.

Displacement (mm)	Story Drift
0.035	0.000025
0.07	0.0001
0.14	0.0001
0.28	0.0002
0.35	0.0003
0.467	0.0003
0.7	0.0005
1.4	0.001
2.8	0.002

Displacement (mm)	Story Drift
3.5	0.0025
4.2	0.003
4.9	0.0035
5.6	0.004
7	0.005
10.5	0.0075
14	0.01
28	0.02
42	0.03

Figure 3.18: Displacement and corresponding storey drift

3.5 Test on Frame specimen

In this section the test of both the corroded frame and the 15 year old specimens will be discussed. The analysis of the experimental results and the comparison with the previous studies by Pinar [23]. This test was conducted in an earthquake lab at Istanbul Technical University. The test begun with setting up all equipment and anchoring the frame to the solid foundation. A test run was made for all LVDT's and other equipments used in the test. During the experiment, the loading was paused at the third cycle of every target displacement to observe the cracks on the specimen. According to the PEER 2002 [31], this loading is called quasi-static cyclic test, loading is stopped at the optimum target value. At the end of third loading cycle of every target displacement, any crack observed is marked and crack width is recorded. The test continued until failure occurred.
In the process of conducting the experiment, the actuator was adjusted and tighten to apply the desired target displacement. The other instrument that was adjusted was the hydraulic jack, to increase the axial load to the desired constant axial force, which was to be mantained throughout the experiment.

3.5.1 Experimental Results

3.5.1.1 Crack Pattern

Before the experiment, corrosion surface cracks were observed on the specimen. The maximum corrosion crack width was 1.3 mm which was at the bottom of the left column. Transverse cracks was observed at the top edge of the column below the beam -column connection which could be due to shrinkage.

As the experiment was ongoing the corrosion cracks widen and spalling occurred. Spalling of concrete started at 10.5 mm target displacement. Some corrosion cracks continued to grow in length. The new concrete cover cracks started to form at 2.8 mm load displacment with corresponding force of 42.4 kN, in other owrds, the tensile strain capacity of the concrete had reach its threshold.

The specimen was tested until failure was observed. The failure mechanism was shear at the bottom of the left column which occurred during the first (push) cycle of lateral displacement 42 mm shown in Figure 3.19. The observed damages were cracking, reinforcement buckling, concrete cover spalling, bond loss. During the experiment, spalling occurred at the bottom of the columns, flexural cracks and a sudden shear failure. The location of the shear failure was unexpected. This could be attributable to either the bond loss observed after the experiment, severity of corrosion at that section or the out-of-plane displacement observed after the experiment.

Cracks begun to form on the foundation at a lateral displacement of 7 mm with corresponding load 77.8 kN with crack width of 0.2 mm. At 1% drift which corresponds to 14 mm lateral displacement, the maximum crack width was 1.9 mm and the base shear force was 102.7 kN. At 2% drift corresponding to 28 mm, maximum crack width and base shear force was 5mm and 120 kN respectively. At 3% drift (42 mm lateral displacement), maximum crack width was 10 mm at a force of 89.5 kN (push).

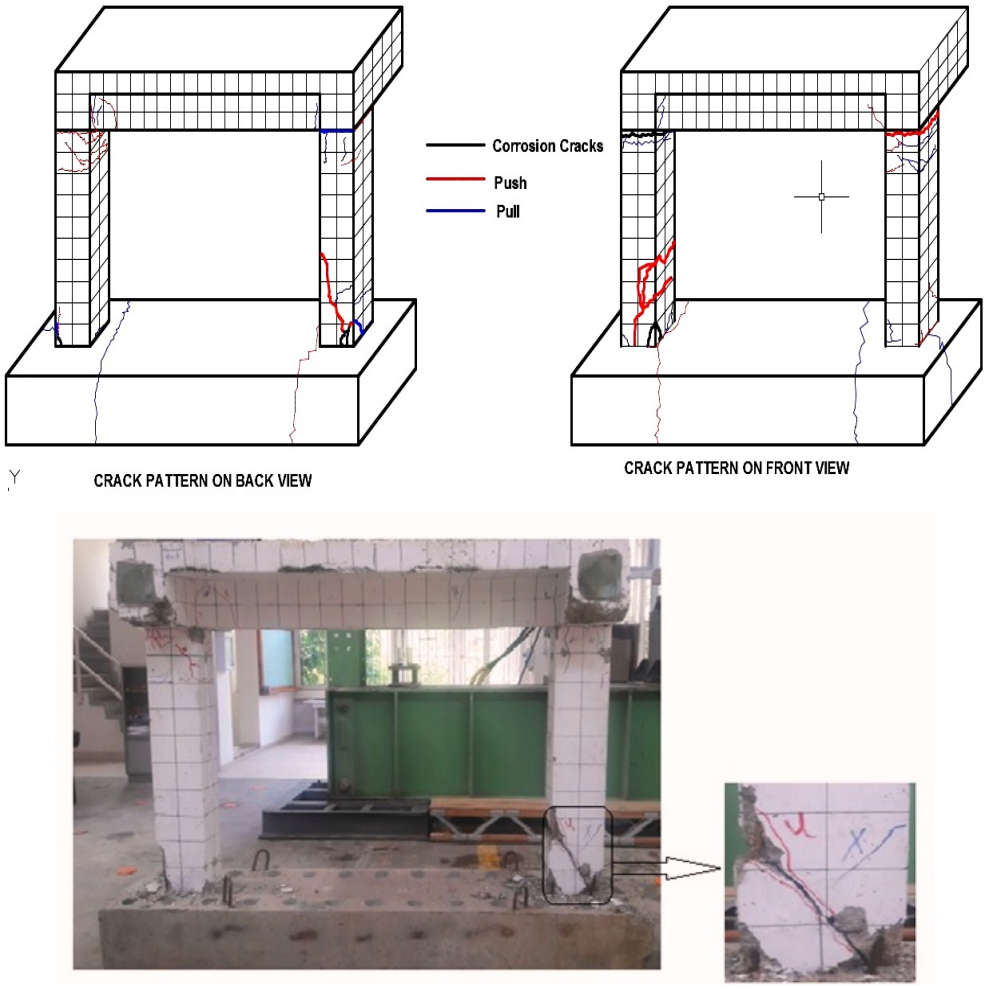

Figure 3.19: Crack pattern of the frame

3.5.1.2 Force-Displacement Relationships

The hysteretic curves of base shear force – displacement measured in this test and the envelope curve is given in Figures 3.21 & 3.20. The hysteretic loops show the displacement process on the frames and the corresponding load. The area of each loop corresponds to the energy absorbed by the structure at that specific target displacement to prevent damage. From Figure 3.21, it is seen that the peak strength of the loop corresponding to a specific story drift decreases from the first cycle to the third cycle of the same displacement. This shows the degradation in the strength and stiffness of the structure. The maximum force obtained in the push (compression) and pull (tension) are 120.2 kN and 125.7 kN respectively

which both occurred at 28 mm lateral displacement (2% drift). At 3% drift (42 mm target displacement), the corresponding loading was 89.5 kN (compression) which is about 25% decrease in the strength. The skeleton curve or the envelope curve in Figure 3.20 was obtained from the average of the peak forces of three cycles of the same displacement.

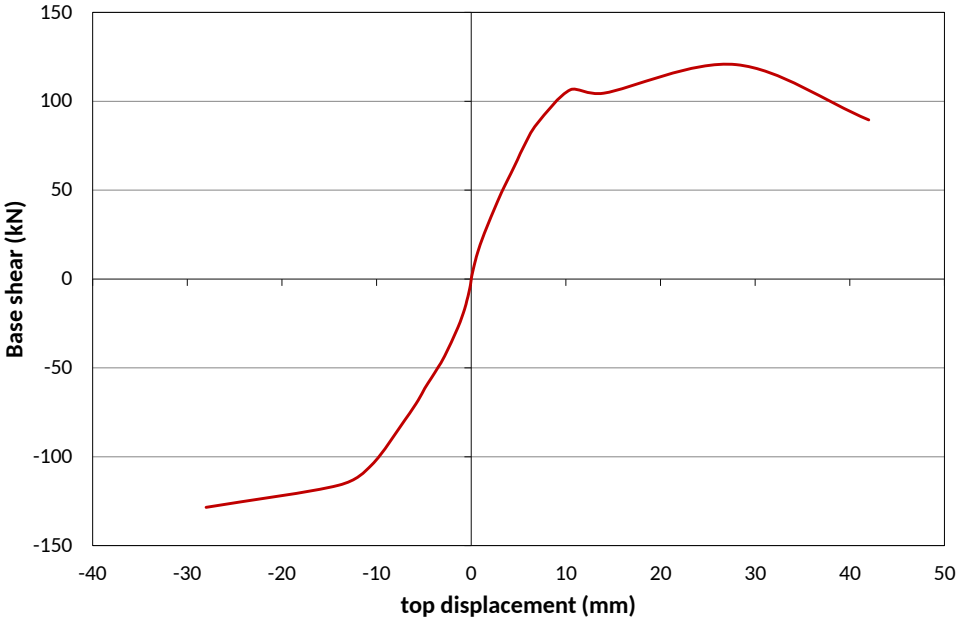

Figure 3.20: Force diplacement envelope curve of the hysteretic loops

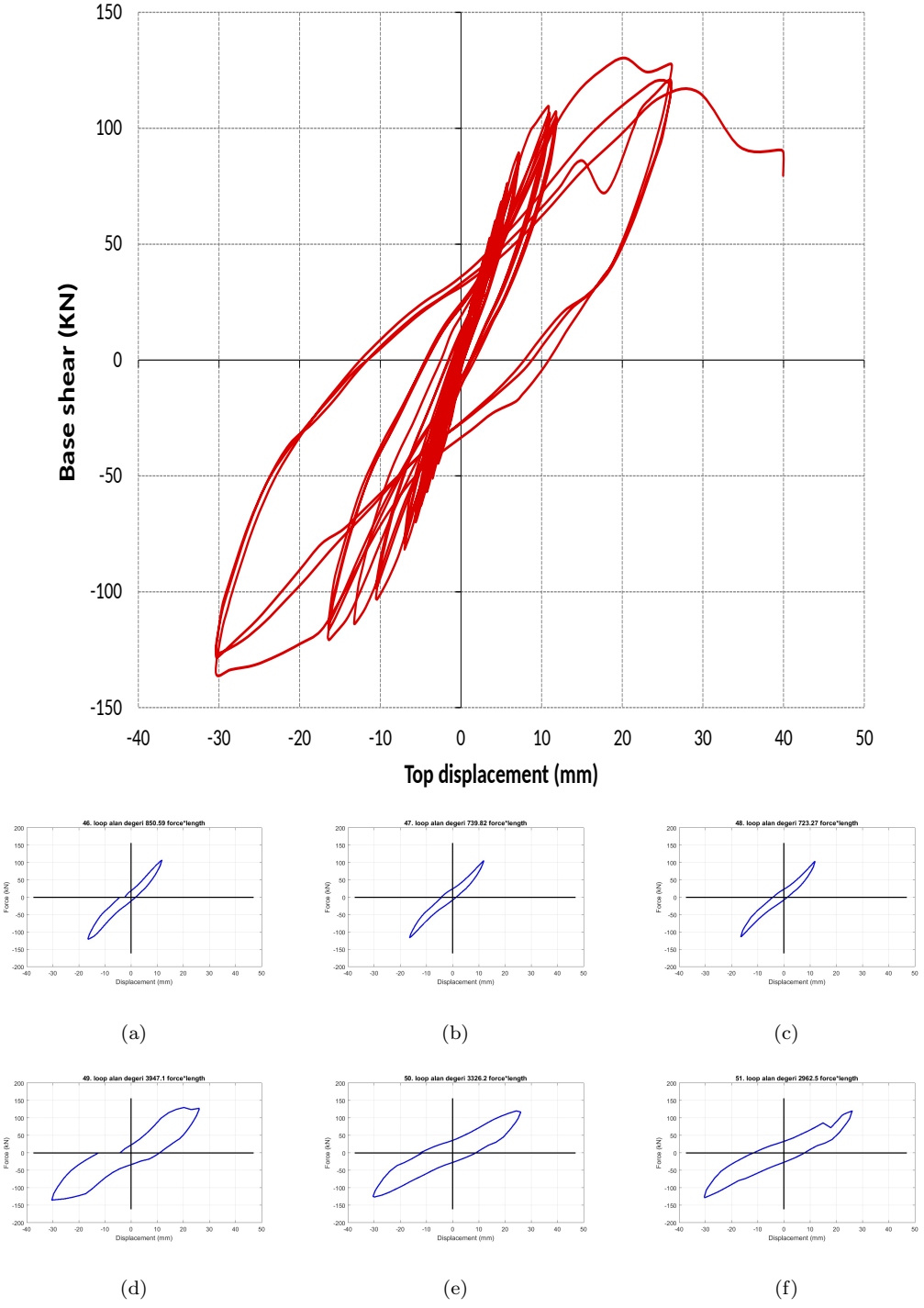

(a) (b) (c)

(d) (e) (f)

Figure 3.21: Force displacement hysteretic loops

3.5.1.3 Rotation

The rotation or the bond- slip rotation at the top and bottom of the columns is found from equation 3.2 as seen in Figure 3.22.

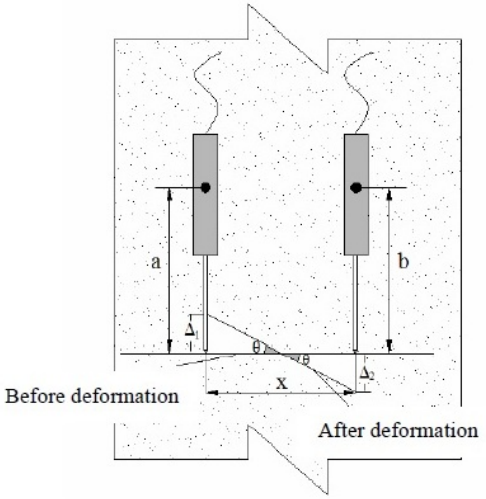

Figure 3.22: Computation of column rotation by LVDT's

$$\theta = \frac{\Delta_1 - \Delta_2}{x} \tag{3.2}$$

θ is the bond slip rotation, $\Delta_1 - \Delta_2$ is the difference between the two displacements obtained from the transducer readings and x is the distance between the two transducers. The force - rotations of the upper and lower sections of both columns are in Figure 3.23. The maximum rotation of all column end is noticed to be 0.02 radians. From the graph in Figure 3.23, at 2% drift, the maximum rotation was almost 0.02 rad.

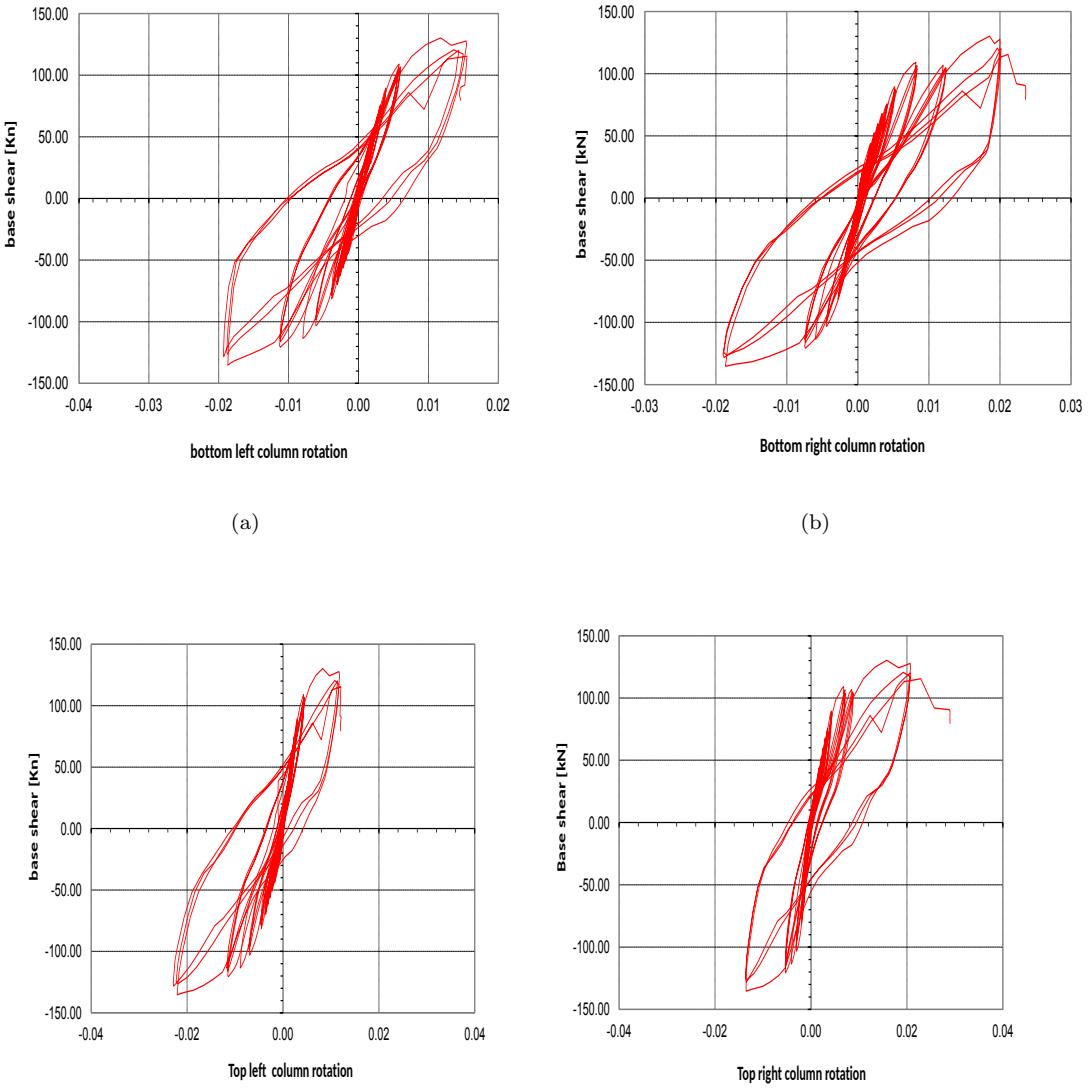

Figure 3.23: Top and bottom column rotations

3.5.1.4 Energy Dissipation

In reinforced concrete, energy dissipation occurs when the structure reaches its inelastic state when subjected to cyclic loading. During the loading stage, the area under the curve shows the energy absorbed by the frame where as the unloading stage, the area is equivalent to the energy released from the frame. In the elastic range, the energy absorbed equals the energy released. The Energy

dissipation shows how a structure is able to release / absorb energy to prevent failure. The energy absorbed in every cycle is calculated from the area engulfed by the hysteresis loop obtained by that loop which is $Area_ABCDE$.

The cumulative energy dissipation observed in this current experiment is found

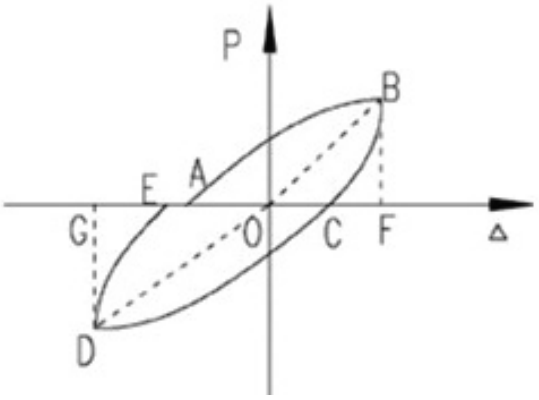

Figure 3.24: Cummulative energy dissipation

to be higher than the control specimen. At 1% drift and 2% drift of the corroded specimen, 38.7% and 35.8% increase in the cumulative energy dissipation capacity, respectively.

3.5.1.5 Equivalent viscous damping

The equivalent viscous damping is measured by the summation of the elastic damping and the hysteretic damping given in equation 3.3. There are several suggested hysteretic damping equations. One being the widely known area based formula is equation 3.4. This was found inadequate for systems with high energy absorption because the equivalent damping becomes too high.

$$\xi_{eq} = \xi_{elastic} + \xi_{hys} \tag{3.3}$$

$$\xi_{eq} = \frac{Area_{loop}}{4\pi \times strainenergy} \tag{3.4}$$

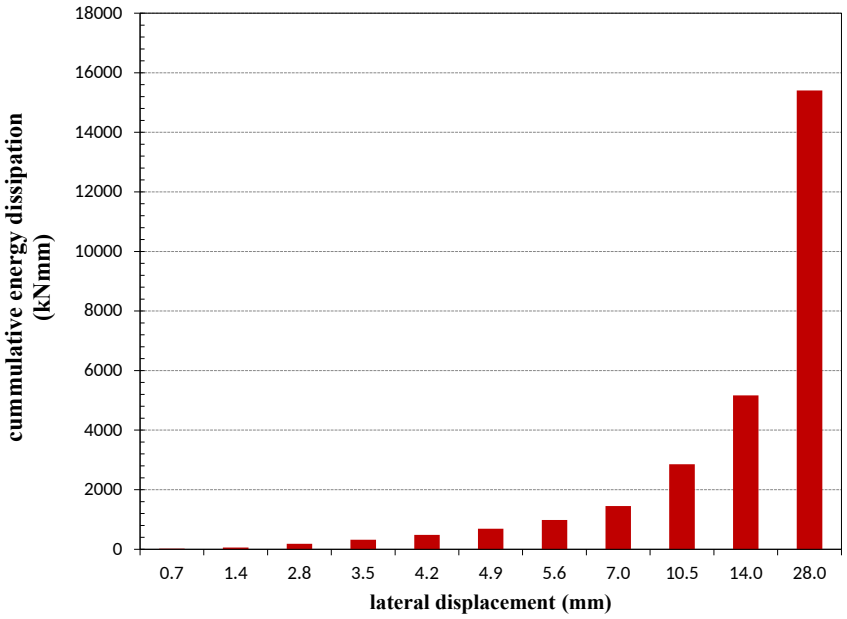

Figure 3.25: Cummulative energy dissipation

Priestly [32] suggested equations for the equivalent viscous damping by considering two case studies; i) using real earthquake accelerograms together with hysteretic rules performed by Dwairi and Kowalsky and ii) the use of artificial earthquake accelerograms together with several hysteretic rules performed by Grant

$$\xi_{hys} = C\left(\frac{\mu - 1}{\mu\pi}\right) \tag{3.5}$$

$$\xi_{hys} = a\left(1 - \frac{1}{\mu^b}\right)\left(1 + \frac{1}{T_e + c^d}\right) \tag{3.6}$$

μ is the displacement ductility which is the ratio of target displacement and yield displacement. In equation 3.6, the hysteretic damping is period dependent compared to equation 3.5. It is significant for $T_e < 1$. Priestly [32] states that the period dependent part can be ignored since regular structures have $T_e > 1$ which makes equation 3.5 similar to equation 3.6.

$$\xi_{eq} = k\xi_{elastic} + \xi_{hys} \tag{3.7}$$

$$\xi_{eq} = \xi_{elastic} + C\left(\frac{\mu - 1}{\mu\pi}\right) \tag{3.8}$$

The elastic damping component of the equivalent viscous damping equation is stiffness dependent hence its can be corrected by a coefficient k, equation 3.7, which is either tangent of initial stiffness dependent. C in equation 3.8 is modified to account for the stiffness effect on the elastic damping. For reinforced concrete frames, Priestly [32] suggested that, for an elastic damping of 0.05, C=0.565.

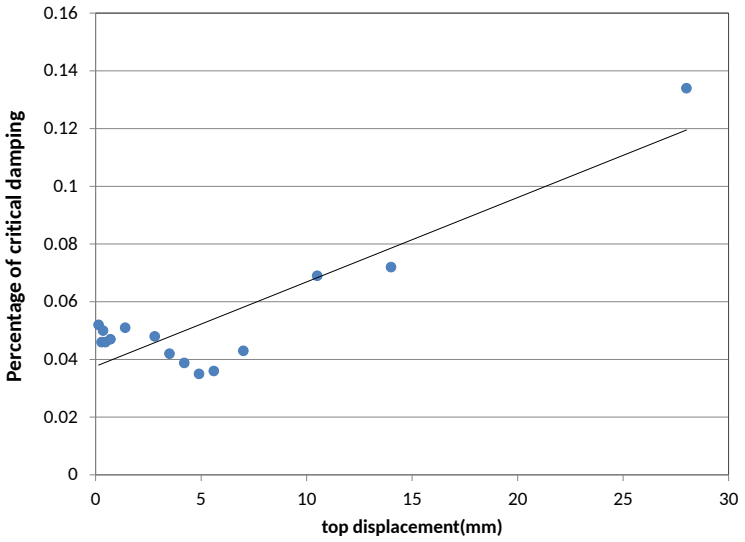

Figure 3.26: Damping of the frame

3.5.1.6 Stiffness

Stiffness degradation is observed from the hysteretic loops as explained in section 3.5.1.2. Two stiffness will be discussed in this section; initial stiffness and lateral secant stiffness. The lateral stiffness is defined as the stiffness of the frame when yielding begins or when the formation of the first plastic hinge occurs. The initial lateral stiffness obtained for the frame under study is 33 kN/mm while that of the control specimen was 22 kN/mm. Han-seung lee [33] explains this increase in stiffness on the rust formed on the surface of the reinforcements and the confining effect of the core concrete generated by the pressure caused by increase in

the volume of the rebar corrosion.

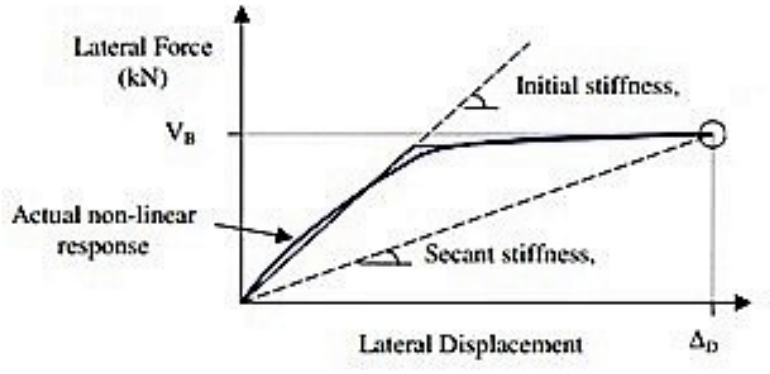

Figure 3.27: Concept of initial stiffness and secant stiffness

Lateral secant stiffness which is also known as the effective stiffness was calculated from equations 3.9 & 3.10.

$$K_\Delta = \frac{\Delta^+ + \Delta^-}{2} \tag{3.9}$$

$$K^+{}_\Delta = \frac{\sum_{j=1}^{3} F^+{}_{j,max}}{\sum_{j=1}^{3} \Delta^+{}_j}, \quad K^-{}_\Delta = \frac{\sum_{j=1}^{3} F^-{}_{j,max}}{\sum_{j=1}^{3} \Delta^-{}_j} \tag{3.10}$$

where $F^+{}_{j,max}$ is maximum positive lateral load of one cycle of same displacement, $\Delta^+{}_j$ is the corresponding lateral displacement, $F^-{}_{j,max}$ is maximum negative lateral load of one cycle of same displacement and $\Delta^-{}_j$ is the corresponding lateral displacement.

Figure 3.28 represents the normalized secant stiffness obtained at each target displacement. The stiffness is observed to degrading as expected because of the decrease in the rigidity of the members as cracks form on the fram during the experiment.

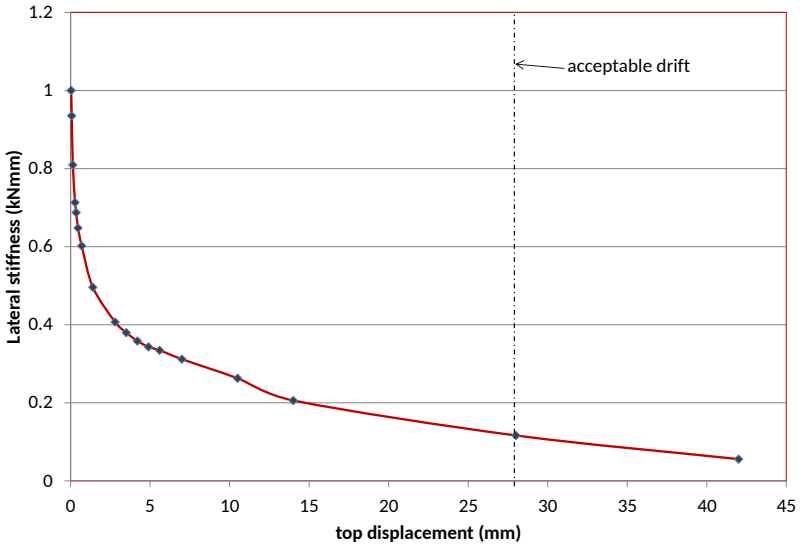

Figure 3.28: Normalized stiffness degradation

3.5.2 Evaluation of Test Results Compared with Reference Frame

The specimen of a past study by Pinar [23] is taken as the reference frame because of the similarity in loading protocol, material compositon and specimen geometry and detailing. The comparision of the experimental test results of both studies is explained here by considering the lateral load carring capacities, rotation capacity, energy dissipation and lateral stiffness .

3.5.2.1 Lateral Load Carring Capacity

From Figure 3.29, the reference frame is observed to have completed both push and pull cycles of target displacement 42 mm, on the other hand, the present frame could not complete the first cycle of 42 mm target displacement. The reference frame failed in both bending and shear and was completed after 3 cycles of 3% storey drift but in the present study, the major failure mode was shear which occur during push in the first cycle of the 3% storey drift together with bending cracks.

Specimen	$P^+{}_{max}$ (kN)	$P^-{}_{max}$ (kN)	δ_{max} (mm)	$P^+{}_{ult}$ (kN)	$\delta^+{}_{ult}$ (mm)	$P^-{}_{ult}$ (kN)	$\delta^-{}_{ult}$ (mm)
Reference frame	123	133	28	86	42	104	42
Test specimen	127.24	135	28	86	42	135	28

Table 3.6: Comparison of ultimate and maximum base shear

For a better comparison of both frames, the envelope or backbone curve in Figure 3.30 was obtained from the average of the ultimate loads obtained from all cycles pertaining to each target displacement. With reference to the tabulated results in Table 3.6, the maximum pull (tension) and push (compression) strength of the reference frame corresponds to 133 kN and 123 kN respectively while presently the maximum strength attained for pull and push is 135.27 kN and 127.74 kN respectively. The increase in strength may be attributed to the increase in strength of concrete over 15 years. The load carrying capacity in the first push cycle of the 3% storey drift (42 mm) is 86 KN. The axial load dropped considerable when the shear crack occured during the gradual lateral loading of 3% storey drift.

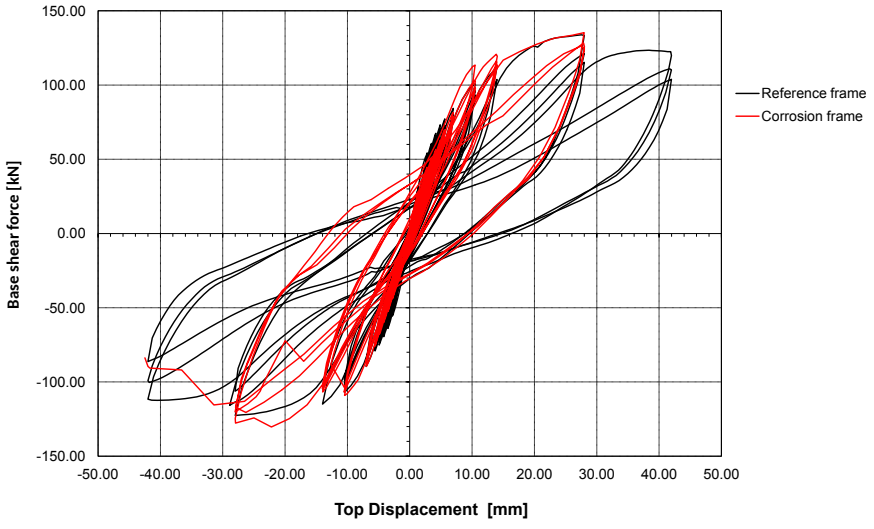

Figure 3.29: Comparison of hysteretic loops

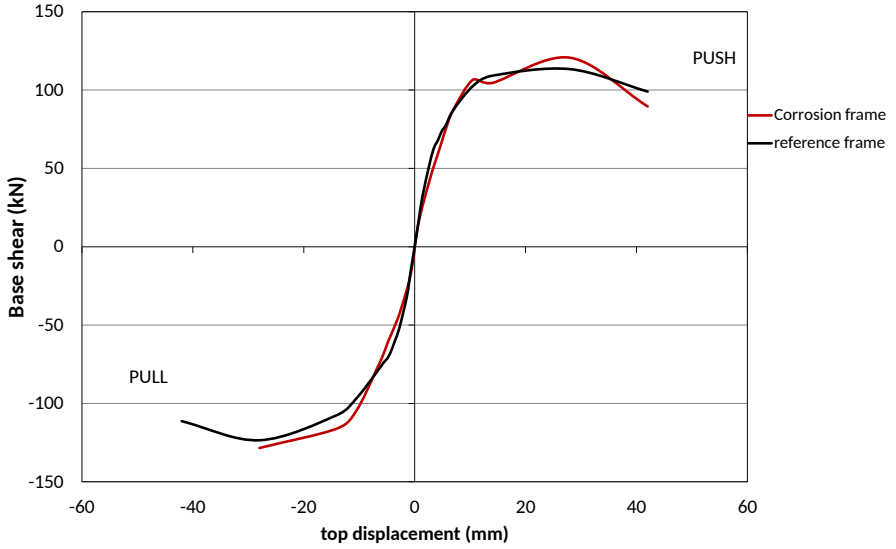

Figure 3.30: Comparison of envelope curves

3.5.2.2 Rotation

The rotations observed in the corroded frame is higher than that of the reference frame. The maximum rotation is 0.02 rad at 2% storey drift. Considering the rotation at the right column for the same target drift, both frames exhibit almost the same rotation in pull but in push, the rotation of the reference frame seems to be lower than the 15 year old frame. The experimental rotation results of both frames is shown in Figure 3.31.

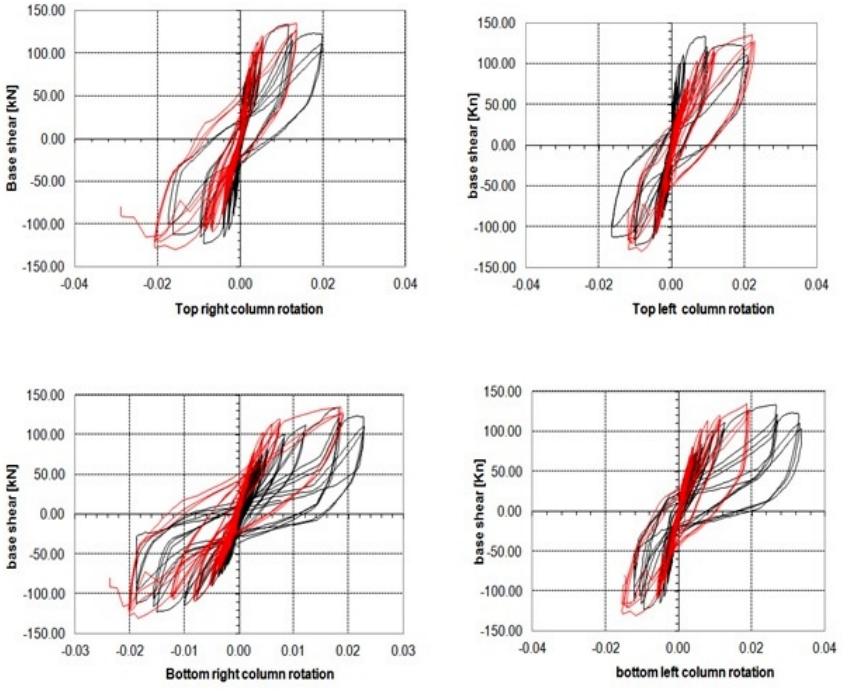

Figure 3.31: Comparison of column end rotation

3.5.2.3 Lateral Stiffness

The stiffness of the frame understudy compared with the reference frame is low as seen from Figure 3.30. The comparison of the lateral stiffness of the reference frame and the test frame specimen (15 year old frame) is given in Figure 3.32. The lateral stiffness is observed to be higher until 0.5% drift in the reference frame compared to the 15 year old frame but after 1% drift, the stiffness is almost the same.

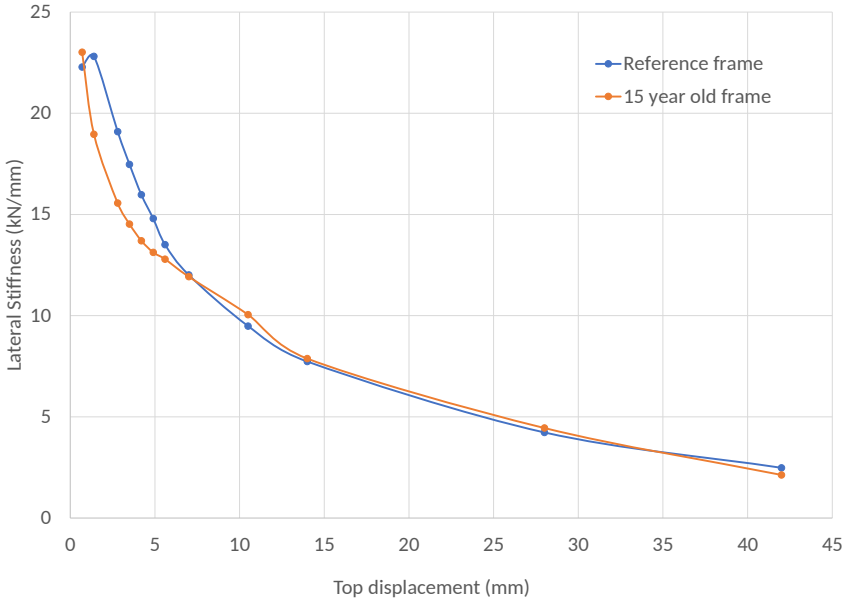

Figure 3.32: Comparison of lateral stiffness

3.5.2.4 Energy Dissipation

The comparison of the energy dissipative characteristics of both frames is given in Figure 3.33. Energy dissipation of the 15 year old frame is noticed to have increased as much as 35% compared to the corroded frame. The cummulative energy dissipation graph shows that before 0.5% drift, the amount energy dissipated is almost equal for both the reference frame and 15 year old frame but begins to increase from 0.5% drift until failure for the 15 year old frame. Therefore the hysteretic structural ennergy dissipation capacity of the 15 year old frame is higher than the reference frame.

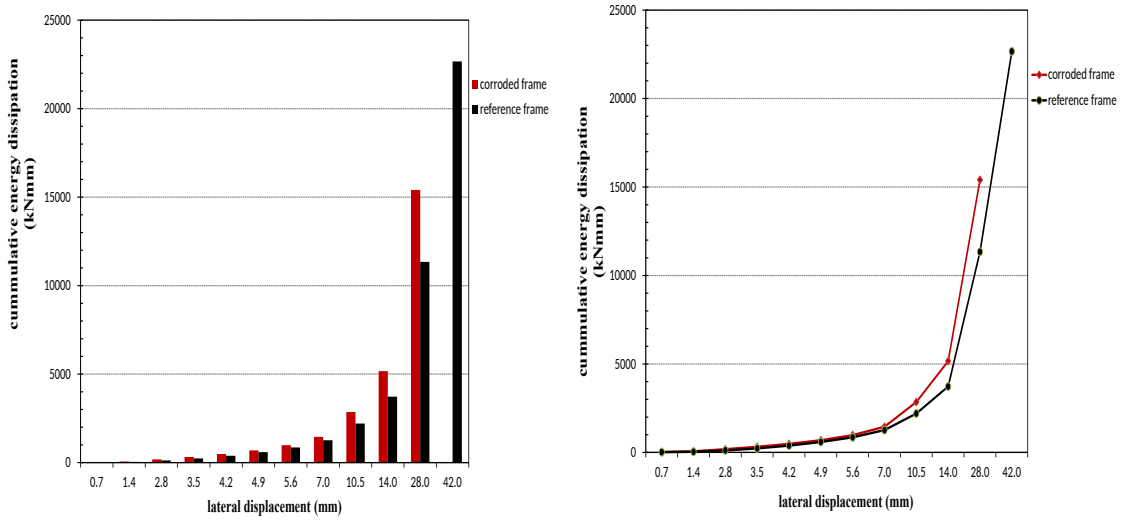

(a) (b)

Figure 3.33: Comparison of energy dissipation capacity

Summary of the observed results ;

i) The stiffness of the frame understudy compared with the reference frame is low as seen from Figure 3.30.

ii) The rotations observed in the corroded frame is higher than that of the reference frame. The maximum rotation as stated in section 3.5.1.3 is 0.02 rad at 2% storey drift. Considering the rotation at the right column for the same target drift, both frames exhibit almost the same rotation in pull but in push, the rotation of the reference frame seems to be lower than the corroded frame. The experimental rotation results of both frames is shown in Figure 3.31.

iii) Energy dissipation of the corroded frame is noticed to have increased as much as 35% compared to the corroded frame.

Chapter 4

Theoretical Works

4.1 Frame

This chapter entails the numerical and theoretical analysis of the 15 year old frame and the cylindrical specimens. The frame is discussed in this section. The aim is to obtain the load carrying capacity of the frame understudy through nonlinear analysis. Nonlinearity effects emerge from either geometric nonlinearity or material nonlinearity. Geometric nonlinearity which deals with large deformations in structures that causes a change in the geometry and material nonlinearity deals with the nonlinear behaviour of the material during deformations. Material nonlinearity will be the focus in this section since a deviation from the elastic properties of the frame was observed during the experimental work. The nonlinear or inelastic finite element analysis is takes into account the post elastic properties of the materials which are the stress and deformation. There are several software that can be used in the nonlinear modelling of structures namely, SAP2000, SeismoStruct, Opensees and Abaqus. Amongst these, SAP2000 and SeismoStruct were selected to study the structural response of the present frame under dynamic loads by nonlinear time history analysis.

Static pushover analysis was performed to observe the structural perfomance under static lateral loads by SAP2000 and adapted computer programs. One algorithm was adapted for the study of displacement based static lateral load increments on the frame which was generalized to perform first and second order

theory of analysis and to determine the buckling loads at each hinge formation stage.

Parametric works were perfomed to study the effects of various parameters on the structural perormance like structural ductility and load carrying capacity. Comparison of the analytical results of frame with experimental results are also discussed in this chapter of the study.

4.1.1 Cyclic Loading in SeismoStruct

SeismoStruct is a fibre-based structural analysis program which can be used to analyse structure under either static or dynamic loading. It considers the effect of both inelastic material properties and geometric non-linearity (second order theory) during analysis. SeismoStruct has the ablity to conduct analysis of structures subjected to nonlinear static and dynamic loads using either the pushover or incremental dynamic analysis to attain the requirements by performance-based seismic assessment. It has eleven incoporated element types that is able to create an different elements classes that are able to accurately represent structural members and non-structural components and can also model different boundary conditions.

4.1.1.1 Material Models

Seismostruct software is equipped with available material models like concrete and reinforcement. The parameters of any selected model is calibrated to fit the mechanical properties of the material obtained from on the experimental results of the material test in the laboratory. Parameters of a model that could not be found was assumed to be the default value provided by the model.

4.1.1.1.1 Concrete

The adapted concrete model is Mander et al nonlinear concrete model shown in Figure 4.1. It is a combination of several models including the uniaxial nonlinear constant confinement model and the cyclic rules proposed by Martinez-Rueda and Elnashai [1997] [34]. The suggestions of the confinement effects provided by the lateral transverse reinforcement by Mander et al. [1988] are included which is, the constant confining pressure is assumed throughout the entire stress-strain range [34]. The calibration parameters required are as follows:

i) Compressive strength, f_c : This is the cylinder compressive stress capacity of the material. Its value was taken from the experimental results [34].

ii) Tensile strength, f_t :This is the tensile stress capacity of the material. It can usually be estimated as
$f_t = k_t\sqrt{f_c}$,
where f_t varies from 2 MPa (concrete in direct tension) to 3 MPa (concrete in flexural tension), as suggested by Priestley etal [1996]. The default value is 2.2 MPa This value was taken as $0.01 f_c$ [34].

iii) Modulus of elasticity, E_c: The resistance to elastic deformation. Its value usually oscillates between 18000 and 30000 MPa[34]. Computed as per TS500[28] requirement.

iv) Strain at peak stress, ε_c: This is the strain corresponding to the point of unconfined peak compressive stress (f_c)[34]. This is taken from experimental results in section 3.1.1.

v) Specific weight, γ: This is the specific weight of the material. The default value is 24 kN/m3 [34].

4.1.1.1.2 Reinforcements

The monti-nuti steel model in Figure 4.1 was adapted for the reinforcement material. it is able to describe the post-elastic buckling behaviour of reinforcing bars under compression. It uses the Menegotto and Pinto [1973] stress-strain relationship together with the isotropic hardening rules proposed by Filippou et al. [1983] and the buckling rules proposed by Monti and Nuti [1992] [34]. The required calibration parameters required are defined as follows:

i) Modulus of elasticity, E_s; It is the elastic stiffness of the material [34]. The default value 200 GPa was used.

ii) Yield strength, f_y: It is the strength at the yielding point [34]. The experimental values was used.

iii) Strain hardening Parameter :This is the ratio between the post-yield stiffness (E_{sp}) and the initial elastic stiffness (E_s) of the material. The post-yield stiffness is defined as
$E_{sp}=(f_{ult} - f_y)/(\varepsilon_{ult} - f_y/E_s)$,
where f_{ult} and ε_{ult} represent the ultimate or maximum stress and strain capacity of the material, respectively. Its value commonly ranges from 0.005 to 0.015 [34].

iv) Transition curve initial shape parameter, R_0 :This is the initial (first loading cycle) value of the parameter R, that controls the shape of the transition curve between initial and post-yield stiffness, necessary to accurately represent Baushinger effects and pinching of the hysteretic loops [34]. The default value 20 is used.

v) Transition curve shape calibrating coefficients, a_1 & a_2 :These are the two coefficients used to calibrate the changes that must be applied to parameter R_0 in order to obtain the updated transition curve shape parameter R_n. Whilst a_1 is usually adopted with an invariable value of 18.5, a_2 might range between

0.05 and 0.15. The default values are 18.5 and 0.15 for coefficients a_1 and a_2, respectively [34]. For the transition curve shape calibrating coefficients, a_2, 0.05 was used.

vi) Kinematic / isotropic weighting coefficient, P : This is the weighting coefficient used in this model to define the degree to which kinematic and isotropic hardening are introduced in the stress-strain cyclic response characteristics of the material. A value close to unity implies a kinematic-dominated hardening behaviour, whilst a value close to zero is employed when isotropic hardening controls the response of the material [34].The default value 0.9 is used.

vii) Spurious unloading corrective parameter, r :This is the threshold for small strain reversals, defined as a percentage of the strain measured at the end of a loading cycle, used to prevent the occurrence of spurious strain unloading cycles. Typical values of r vary between 2.5 and 5 percent [34]. The default value is 2.5%.

viii) Fracture strain, ε_{ult} :This is the strain at the occurance of fracture of reinforcement [34]. The default value is 0.1.

ix) Specific weight, γ: This is the specific weight of the material. The default value 78 kN/m^3 is used

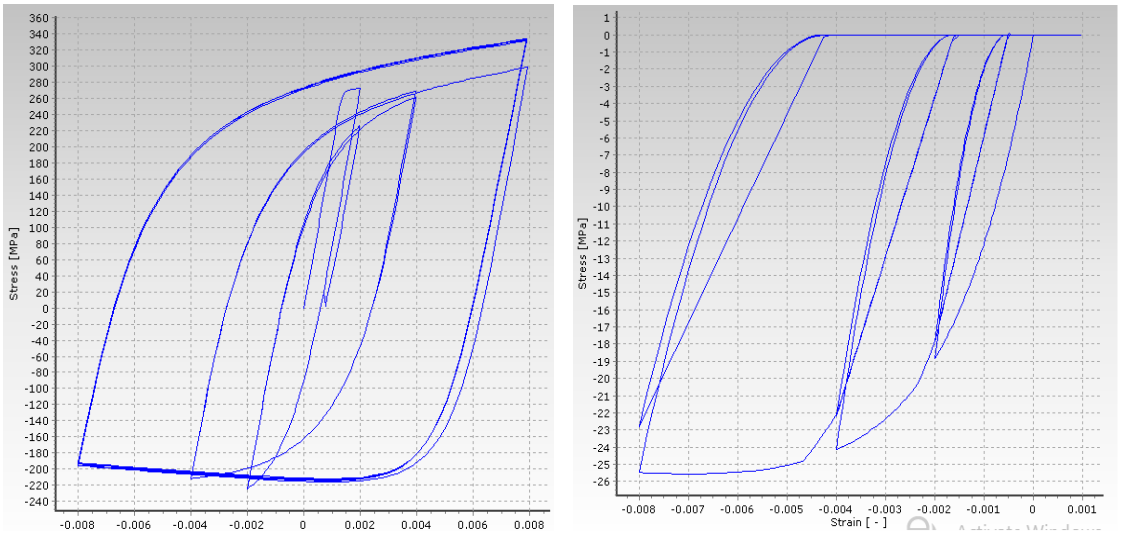

(a) (b)

Figure 4.1: a)Monti-nuti steel model for steel, b) Mander et al nonlinear concrete model

4.1.1.2 Analytical model

The model used is given in Figure 4.2. The arrangement of reinforcement is unsymmetric along the height of the column hence for each column two different sections were assigned. Potential hinge formation elements were subdivided into four sections. The column elements were defined as inelastic displacement frame elements and the beam elements were defined as elastic frame elements.

The inelastic displacement base frame elements is the displacement-based 3D beam-column element type in SeismoStruct capable of modelling members of space frames with geometric and material nonlinearities. The sectional stress-strain state is obtained through the integration of the nonlinear uniaxial material response of the individual fibres in which the section has been subdivided, fully accounting for the spread of inelasticity along the member length and across the section depth [34].

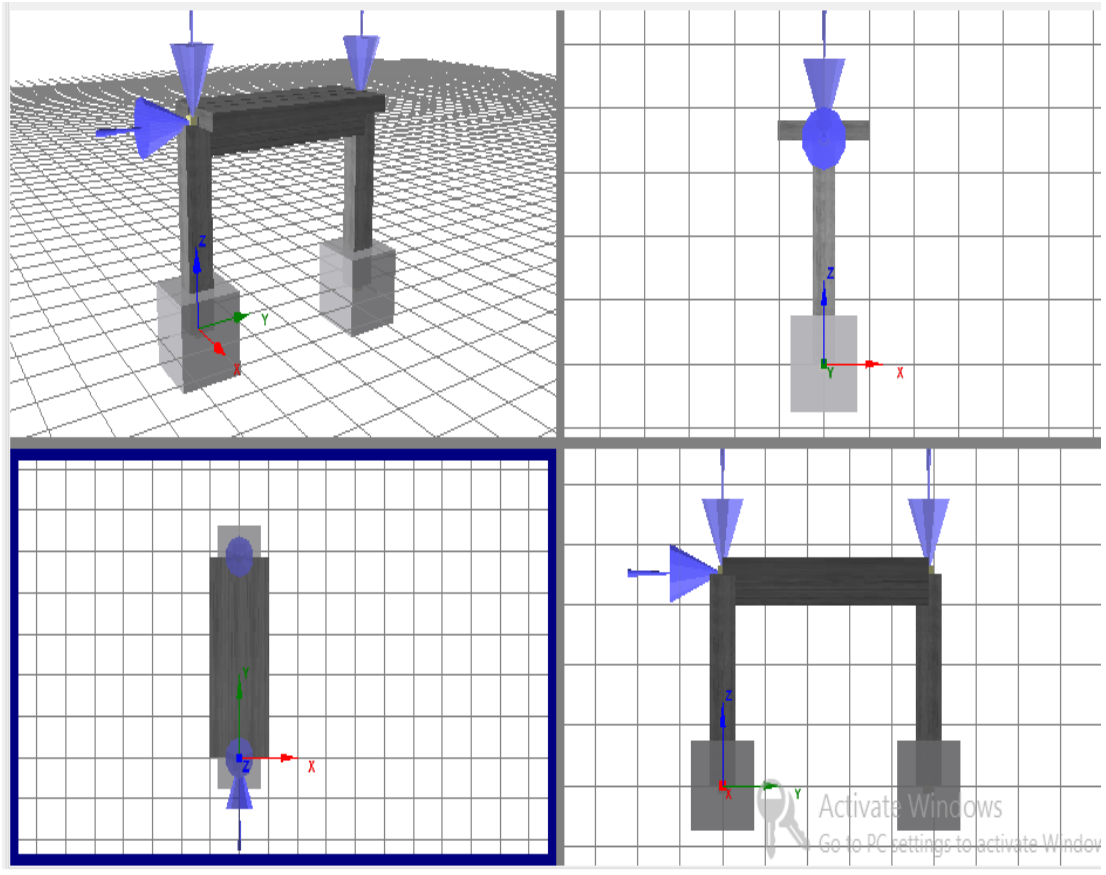

Figure 4.2: Analytical frame model in SeismoStruct

The elastic frame element was used in the beams because after the experimental work, no cracks were observed on the beams hence it remained in the elastic state. The beam was not divided into several peices, it was taken as one whole elastic element as shown in Figure 4.3. The perfomance of these segmented elements were studied during the nonlinear time history analysis of the analytical frame model.

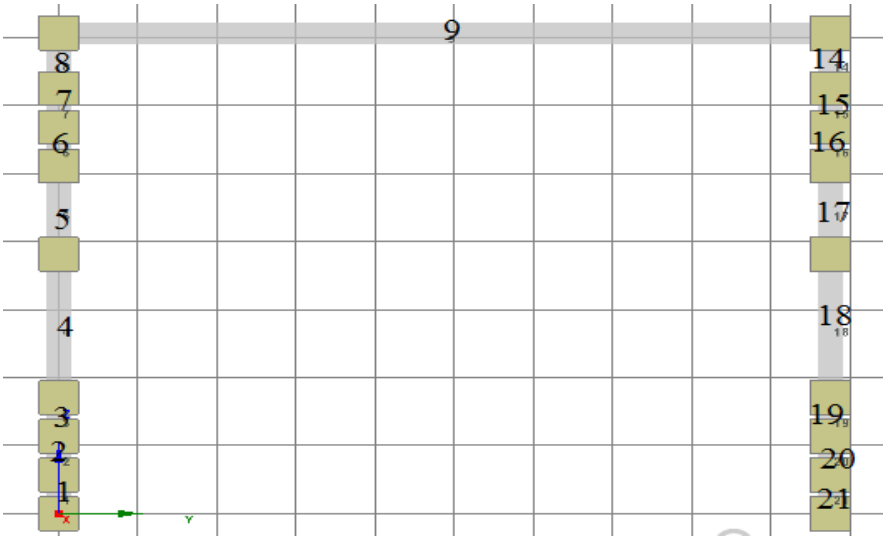

Figure 4.3: Segmented frame model in SeismoStruct

SeismoStruct helps study the Damage states of any structure during dynamic loads as the performance criteria. The Performance criteria of elements were defined by the strain limits of the materials as per the Turkish earthquake code requirements TSC [24]. For ductile elements there are three damage limit states; Minimum damage limit, MN - the behavior beyond the elasiticity, Saftey limit, GV - the behaviour beyond elasticity that the element is capable of ensuring the strength and Collapsing limit, GC - the limit before collapse. Figure 4.4 show a brief discription of the damage states defined by TSC [24].The defined element damage states is given in Table 4.1.

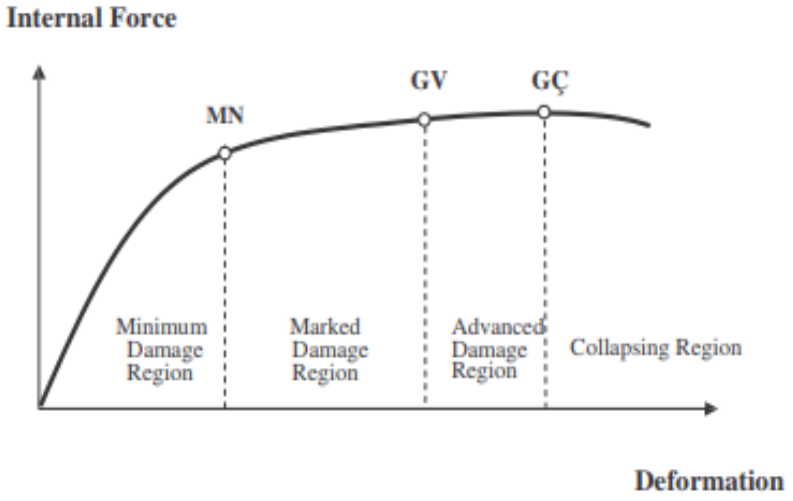

Figure 4.4: Damage states of a ductile structure.TSC [24]

Performance criteria	Strain damage boundary	Description
Yield	>0.002	Yielding of reinforcements
MNc	<-0.0035	Minimum damage of unconfined concrete
MNs	>0.01	Minimum damage limit of reinforcement
GVc	<-0.0085	Safety limit of confined concrete
GVs	>0.040	Safety limit of reinforcements
GCc	<-0.011	Collapse limit of Concrete
GCs	>0.060	Collapse limit of reinforcements

Table 4.1: Strain limit for ductile elements as per TSC [24]

4.1.1.3 Comparison of analytical results and experimental results

The analytical model was subjected to constant static loads and cyclic displacement reversal obtained from the experimental work. Figure 4.5 shows the displacement time history of the structure.

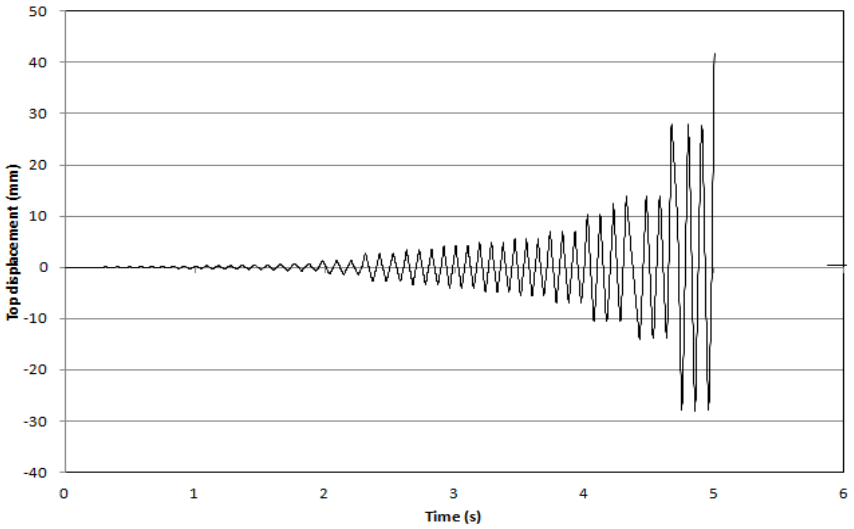

Figure 4.5: Displacement time history

The analytical result and the experimental results is plotted in Figure 4.6. The backbone curve of this analysis in Figure 4.7 is computed as the average of the three ultimate load obtained per cycle for both push and pull cycles. The backbone curve traces the path of the ultimate base shear at every stage of cyclic loading.

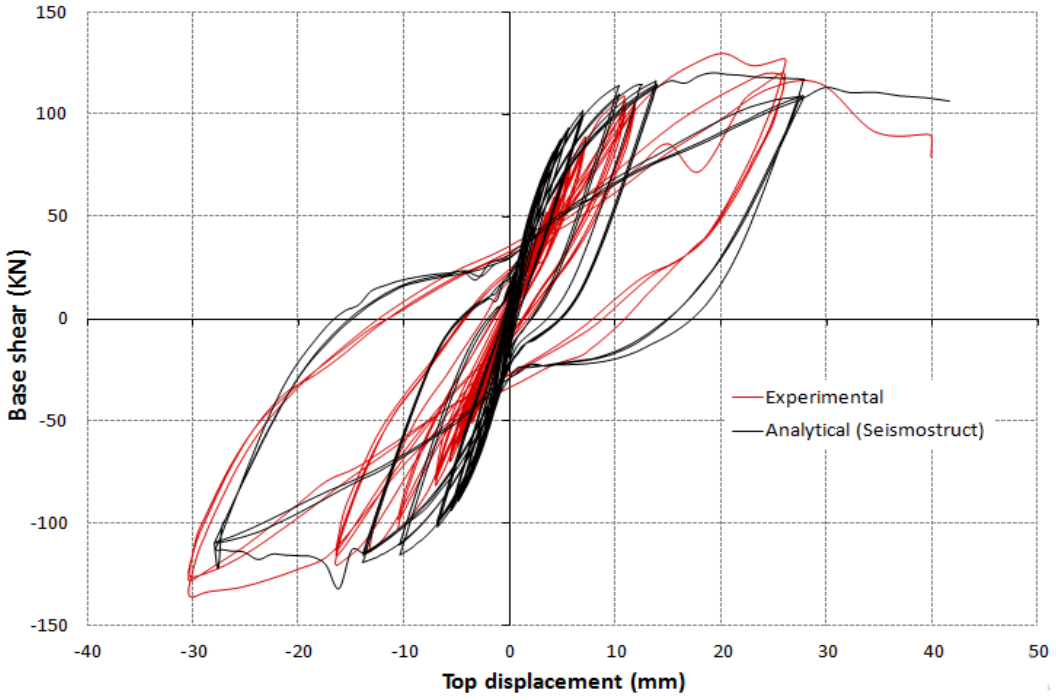

Figure 4.6: Analytical(SeismoStruct) and Experimental results of cyclic load analysis

From the envelope obtained from the cyclic structural response, the stiffness of the analytical model is high in both the push and pull cycles during the elastic state compared to the experimental results. The strength is lesser than expected at the post elastic state. The maximum load capacity of the analytical model during the push cycle is same as the results obtained experimentally but the corresponding target displacement is smaller compared to the experimental results. The softening of the structure begins after 1% storey drift is attained but in the experimental work, sotftening begins after 2% storey drift is attained.

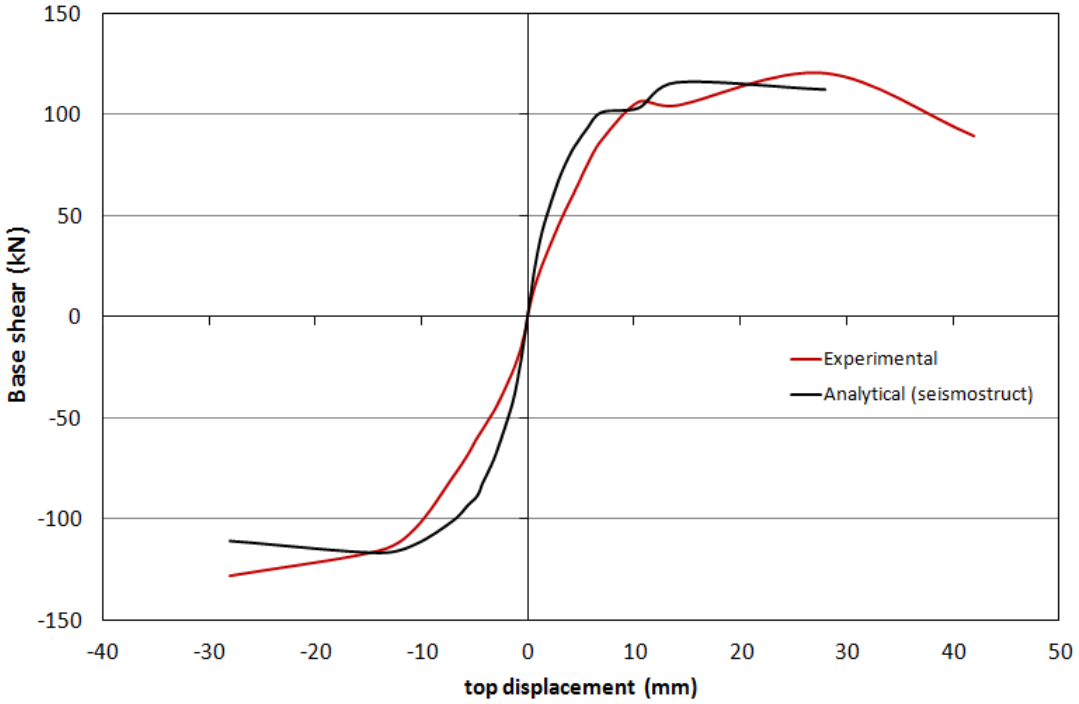

Figure 4.7: Envelope of Analytical (SeismoStruct) and Experimental results

Assessment of the damage state in the analytical work is given in Table 4.8. The onset of yielding in the structure occured during the first cycle of 4.9 mm target displacement (0.35% storey drift) in elements 21 and 1 which are bottom ends of the both columns. The definition of yielding in the analysis was taken as the onset of yielding in the longitudinal reinforcements. The yielding of longitudinal reinforcement further occured at 0.5% storey drift in elements 8 and 14 which are the elements located at the top ends of the column. The minimum damage limit of unconfined concrete was first observed at the bottom left and right of the column during the first cycle of 0.75% storey drift. The reinforcement at the bottom of the right column was first to exceed the minimum strain limit succeeded by the bottom left column during the push cycle of 14 mm (1% storey drift).

The safety limit was first exceeded at the bottom of the left column at 28 mm (2% drift) in the during the first cycle of push which was suceeded by the confined concrete reaching its safety and collapse limit in the same cycle at the bottom of the left column(Element 1). In the pull cycle of the same storey drift, the

collapse limit of confined concrete was reached in element 21.

The damage states given in the table shows that, damage or cracks was highly concentrated at the bottom of the column which was corresponds to the failure observed in the experimental works. Minimal damage was observed at the top of the columns compared to the bottom sections of the columns.

Displacement cycle	Time step	Damage state	Element	Material	Strain	Section
First cycle of +4.7mm	7.3347	yield	21	Reinf. Steel	0.00207538	Sec(b)
First cycle of +4.7mm	7.3393	yield	21	Reinf. Steel	0.00204157	Sec(a)
First cycle of -4.7mm	7.4382	yield	1	Reinf. Steel	0.00210634	Sec(a)
First cycle of -4.7mm	7.4405	yield	1	Reinf. Steel	0.00205652	Sec(b)
First cycle of +7mm	8.5744	yield	14	Reinf. Steel	0.00200985	Sec(a)
First cycle of +7mm	8.579	yield	14	Reinf. Steel	0.00204164	Sec(b)
First cycle of -7mm	8.6871	yield	8	Reinf. Steel	0.00200478	Sec(b)
Second cycle of -7mm	8.6917	yield	8	Reinf. Steel	0.0020782	Sec(a)
First cycle of 10.5mm	9.2437	MNC	1	Concrete	-0.00363426	Sec(a)
First cycle of 10.5mm	9.246	yield	20	Reinf. Steel	0.00204297	Sec(b)
First cycle of -10.5mm	9.3564	MNC	21	Concrete	-0.00354911	Sec(b)
First cycle of -10.5mm	9.3587	yield	2	Reinf. Steel	0.00202155	Sec(a)
Third cycle of +10.5mm	9.7083	yield	20	Reinf. Steel	0.00207392	Sec(a)
First cycle of +14mm	9.9337	MNC	1	Concrete	-0.00350688	Sec(b)
First cycle of +14mm	9.9337	MNS	21	Reinf. Steel	0.01008848	Sec(b)
First cycle of +14mm	9.936	MNS	1	Reinf. Steel	0.010343	Sec(a)
First cycle of +14mm	9.936	MNC	8	Concrete	-0.00354103	Sec(b)
First cycle of +14mm	9.936	MNS	21	Reinf. Steel	0.01013042	Sec(a)
First cycle of -14mm	10.1522	yield	2	Reinf. Steel	0.00202092	Sec(b)
First cycle of -14mm	10.166	MNS	1	Reinf. Steel	0.01003113	Sec(b)
First cycle of -14mm	10.1683	MNC	14	Concrete	-0.0035602	Sec(a)
First cycle of -14mm	10.1683	MNC	21	Concrete	-0.00354931	Sec(a)
First cycle of +28mm	10.7203	yield	15	Reinf. Steel	0.00200477	Sec(a)
First cycle of +28mm	10.7226	MNS	14	Reinf. Steel	0.01017706	Sec(a)
First cycle of +28mm	10.7249	GVc	1	Concrete	-0.00901159	Sec(a)
First cycle of +28mm	10.7249	MNS	14	Reinf. Steel	0.01066159	Sec(b)
First cycle of +28mm	10.7249	yield	15	Reinf. Steel	0.00210171	Sec(b)
First cycle of +28mm	10.7272	MNC	8	Concrete	-0.00364115	Sec(a)
First cycle of +28mm	**10.7295**	**GCc**	**1**	**Concrete**	**-0.01309831**	**Sec(a)**
First cycle of +28mm	10.7318	yield	7	Reinf. Steel	0.00205251	Sec(b)
First cycle of +28mm	10.7364	MNS	8	Reinf. Steel	0.01062033	Sec(b)
First cycle of -28mm	10.8997	GVc	21	Concrete	-0.01008175	Sec(b)
First cycle of -28mm	10.902	yield	7	Reinf. Steel	0.00209977	Sec(a)
First cycle of -28mm	10.902	MNS	8	Reinf. Steel	0.0104886	Sec(a)
First cycle of -28mm	10.902	MNC	14	Concrete	-0.00363822	Sec(b)
First cycle of -28mm	**10.902**	**GCc**	**21**	**Con. concrete**	**-0.01222279**	**Sec(b)**
First cycle of 42mm	11.4957	GVc	8	Con. oncrete	-0.00860885	Sec(b)
First cycle of 42mm	11.4963	GVs	1	Reinf. Steel	0.04025237	Sec(a)
First cycle of 42mm	11.5	GVs	21	Reinf. Steel	0.04165981	Sec(b)

Figure 4.8: Damage states from analytical results

4.1.2 Cyclic Loading in SAP2000

4.1.2.1 Materials Model

The material properties were obtained from the taking samples from the corroded frame. Several concrete core specimens were extracted and tested and eight longitudinal reinforcements were cut from the frame after breaking the concrete. The material properties obtained from the compressive and tensile test of the concrete and reinforcement respectively were used in the material modelling of the elements.

4.1.2.1.1 Concrete

Concrete core samples extracted from the corroded specimen were tested. The details are outlined in table 3.3. These properties were used in the concrete model in SAP2000. The nonlinear material properties were selected to be computed by Mander Stress- Strain equations. The following properties were required to define the stress strain curve of the concrete:

i) Ultimate Concrete stress, f'_c: This represents the unconfined concrete stress. This was taken from the value obtained from the cylindrical core sample test given in table. The tensile strength of the concrete was taken as $0.052\sqrt{f'_c}$ MPa.

ii) Elastic modulus, E_C: This was computed from this formula, $E_C = 5000\sqrt{f_{ck}}$ (MPa) from TSC[24].

iii) Shear modulus: The shear modulus is automatically calculated as approximately 40% of the modulus of elasticity.

iv) Coefficient of thermal expansion: It was taken as the default value of 9.9×10^{-6}.

v) Weight per unit volume: The unit weight is taken as 23 kN/m^3.

4.1.2.1.2 Steel Reinforcement

The properties of the reinforcements were defined based on the results obtained from the tensile test performed on the extracted reinforcement from the frame. The results are listed in Table 3.5. The model used for the nonlinear material properties is a simple parametric stress strain model.

i) Yield tensile strength: This was taken from the value obtained from the tensile test on the extracted reinforcements.

ii) Ultimate tensile strength: This was taken from the value obtained from the tensile test performed on the extracted rebars.

iii) Elastic modulus: This was taken as 200GPa.

iv) Shear modulus: The shear modulus is automatically computed.

v) Coefficient of thermal expansion: It was taken as the default value of 1.17×10^{-5}.

vi) Weight per unit volume: The weight is taken as $77\text{kN}/m^3$.

4.1.2.2 Pivot Hysteretic Model

SAP2000 offers various models for the hysteretic behaviour of structures under cyclic loading. Amongst them is the pivot hysteretic model which is capable to model the hysteretic behaviour of a structure based on defined pivot points and also capable to define the stiffness and strength degradation during the cyclic loading. It was proposed by Dowel et al [35] for nonlinear dynamic seismic analysis of bridge structures observing the nonlinear behaviour (force vs displacement and / moment rotation) of structural members under cyclic loading.

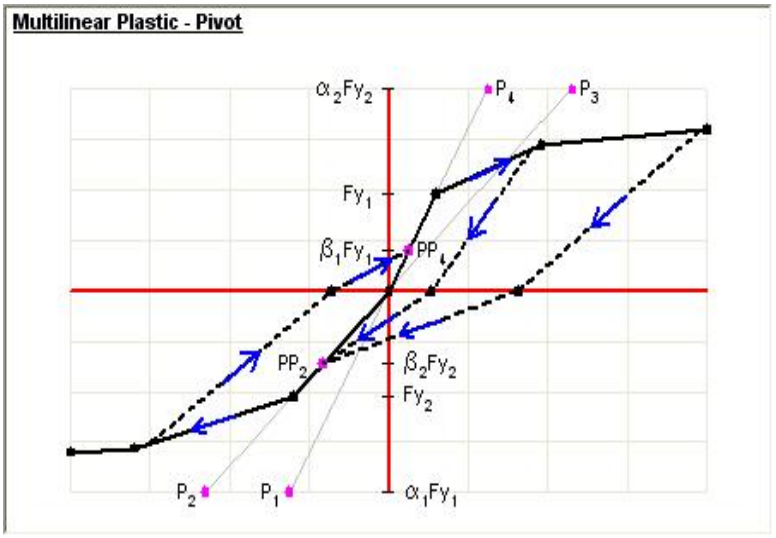

Figure 4.9: Pivot Hysteretic Model

Parameters are calibrated to define or locate pivot points to control the degrading hysteretic behaviour. From Figure 4.9, P_1 through P_4 are the pivot points on the elastic stiffness lines which controls the rate of softening, specifically P_1 and P_4 is on the positive elastic rigidity and P_2 and P_3 is on the negative elastic rigidity. Bal [36] further explains the points on the pivot hysteretic model. The parameters α_1, α_2, β_1 ,β_2 and η are obtained from experimental data which mainly depends on the yielding point.

4.1.2.3 Numerical Model

The model in Figure 4.11 was used in the cyclic analysis of the frame by SAP2000. The only exception is the replacement of plastic hinges with link elements. Link elements were assigned at regions with potential plastic hinge formation on the frame as shown in Figure 4.11. Link element was assigned multi linear plastic nonlinear two joint link element properties to define the nonlinear behaviour. It is normally recommended to assign link elements at a short length mostly the length of the plastic hinge hence considering the stresses almost the same along the length.

For link elements to represent structural elements, the six deformational degrees-of-freedom (DOF) or internal forces together with the stiffness must be assigned. The axial deformation, U_1 was considered to be linear, shear deformation (U_3), torsional deformation (R_1) and pure bending deformation (R_2) were considered to be fixed, where 1,2 and 3 corresponds to z, x and y axis respectively. The bending moment, R_3 and shear deformation U_2 are assigned nonlinear characteristics. The effective stiffness of the axial deformation, shear deformation and the bending deformation was obtained from equation 4.1

$$\begin{aligned} Bending\,stiffness &\rightarrow \frac{4EI}{L} \\ Shear\,stiffness &\rightarrow \frac{12EI}{L^3} \\ Axial\,stiffness &\rightarrow \frac{EA}{L} \end{aligned} \tag{4.1}$$

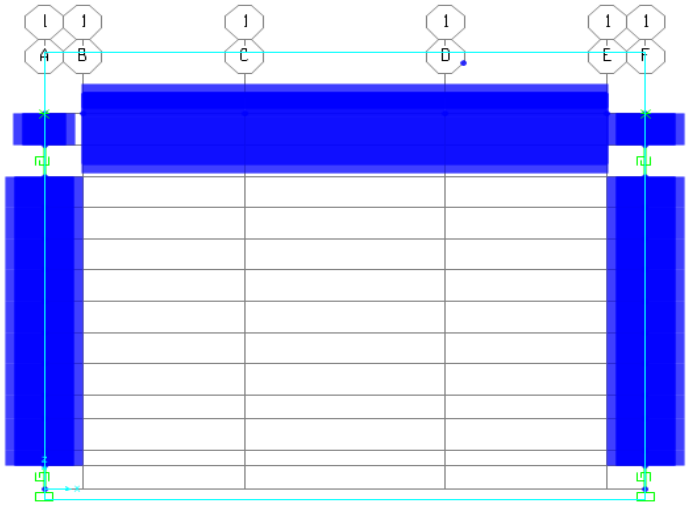

Figure 4.10: Frame model for cyclic analysis SAP2000

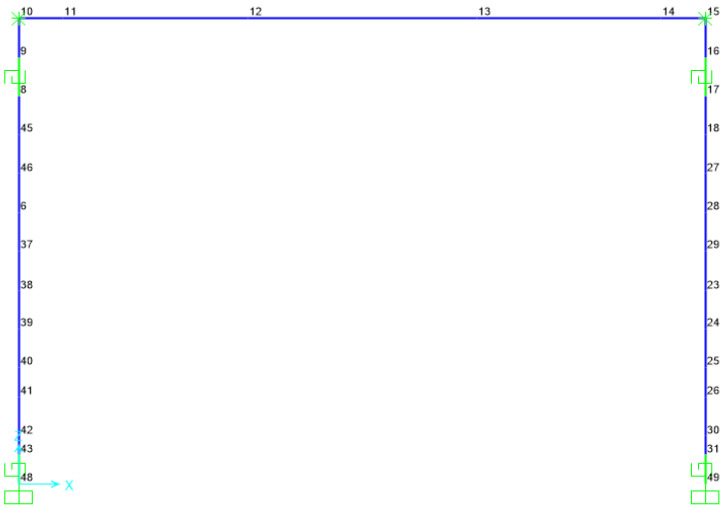

Figure 4.11: Frame model2 for cyclic analysis SAP2000

The cyclic loading was performed using nonlinear direct integration time history analysis. The experimental displacement protocol was assign as a time history function which was used in the analysis. This displacement protocol was considered as a support settlement of the top displacement by restraining translation of the top nodes in the x-axis.

4.1.2.4 Comparison of Results with Experimental Results

The loading protocol for the experimental work in Figure 4.12 was used in this analysis. The comparison of the analytical cyclic loading and experimental results is given in Figure 4.13

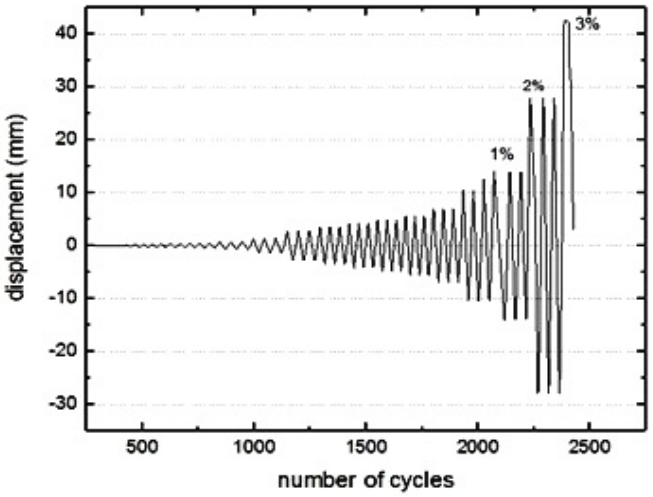

Figure 4.12: Loading protocol for cyclic analysis inSAP2000

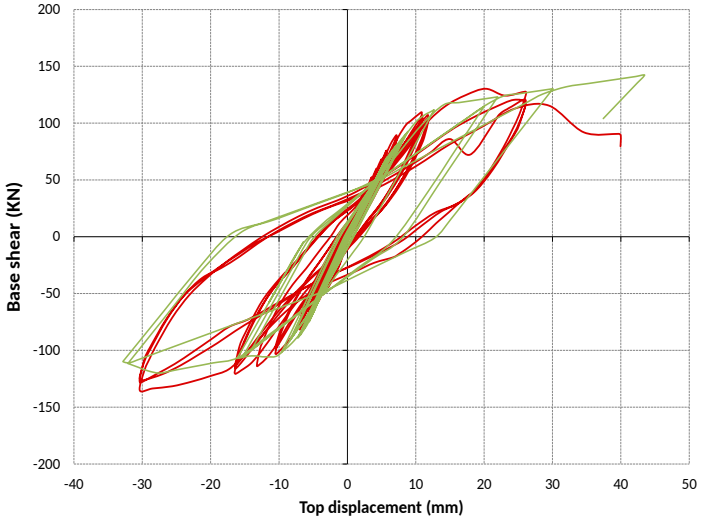

Figure 4.13: Comparison of hysteretic curves of analytical and experimental specimens

The structural response of the analytical model over estimates the loads and the displacement. It is observed that the ultimate load is over estimated at a target drift of 42 mm target displacement. Ultimate strength of 127.9 kN was obtaineds at 29 mm in the push cycle and 107.2 kN in the pull cycle at 28 mm. The initial stiffness of the analytical model is smaller than the expeimental hysteretic

crurves. The overall structural performance under seismic load was determined to be almost same as the experimental analysis.

4.1.3 Lateral Load Increments

4.1.3.1 SAP2000

Lateral load increment (Pushover analysis) is one of the theoritical works considered to study the preformance of the frame under static loads. Static-pushover analysis is a static nonlinear analysis where monotonic load increments are applied to the structure understudy in both the elastic and inelastic states until one section reaches its ultimate capacity or until a mechanism occurs. Plastic hinges are positioned on sections which have reached its inelastic state.

4.1.3.2 Description Of Elements in SAP2000

The frame elements are represented by a line element in SAP2000. Each frame element is composed of its elastic and inelastic properties. The inelastic properties are represented as concentrated plastic hinges.

Localization of plastic deformations is considered after the flexural members have yielded. This is known as the plastic hinge zone and it governs the capacity of the structure (strength and deformation). SAP2000 offers three options to define the hinge properties; default ,user defined and generated hinge properties. Inel [37] suggested that, for inelastic behaviour of elements, the user defined hinge properties is better than the default hinge properties option. The default hinge properties are defined automatically based on the section properties assigned to each element. SAP2000 built-in hinge properties are based on FEMA 273. User-defined hinge properties will be used for the column but default hinge properties for the beam.

The moment rotation relationship of each section is used to model the deformation of the plastic hinge of all the elements of the reinforced concrete frame so the

beam hinge property is assigned bending deformation M_3 while the columns are assigned user defined axial force, P and bending moment, M_3 interaction curves for hinges since the lateral force will change the axial force on the column. The detailing of reinforcements in the columns is not symmetric, hence different moment curvature along the length of the column.

Moment curvature for each element given below is from SAP2000 computer program. SAP2000 uses the idealized form of the moment curvature equivalent to FEMA 365 [38] for both ductile and brittle behaviours. For a ductile displacement based design, the general idealized force displacement graph from FEMA 365 [38] is shown in Figure 4.14.

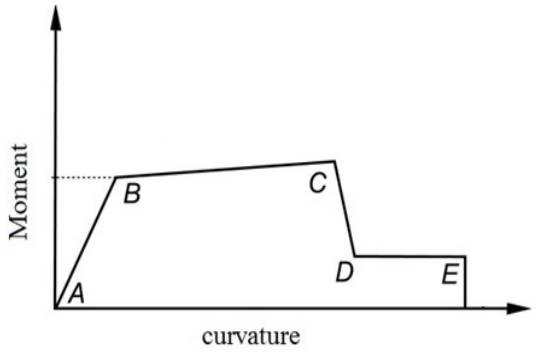

Figure 4.14: Force deformation relationship (FEMA[38])

where; B is the yıeld moment and the corresponding yield curvature. C is the ultimate moment and curvature. D is the residual strength of the member. The limit is taken as 20% of the yield strength at the ultimate curvature [37]. E is failure or extreme damage point. The strength limit is taken as D's and curvature as 10 times the yield curvature.

Considering the upper section of the column, the moment curvature for an axial force of 100KN and 350KN for positive and negative moment is shown in Figure 4.15 since the section is not symmetric about the x-axis. The moment curvature is obtained from Xtract software considering the same material properties. The moment rotation user defined hinge properties for all elements in SAP2000 are

the defined according to the moment curvature obtained for Xtract. The length of the plastic hinge was defined according to Priestley and Pauley [39] plastic hinge formulation.

Moment curvature relationships of the sections used in this study as mentioned above are obtained by using a cross sectional analysis program named XTRACT. XTRACT is a fully interactive program for the analysis of any cross section. It can generate moment curvatures, axial force and moment interactions diagrams for concrete, steel, prestressed and composite structural cross-sections.

$$x_P = x_U - x_Y \tag{4.2}$$

$$\theta_P = L_P \times x_P \tag{4.3}$$

where x_P is the plastic curvature, x_U is the ultimate curvature and x_Y is the yield curvature, θ_P is the plastic rotation and L_P is the length of the plastic hinge.

4.1.3.3 Analytical Model

The frame is modelled as a 2D structure with all elements drawn as line objects. The frame as discussed previously comprises of the beam and two columns. The beam is partitioned into 5 sections and each column was partitioned into 9 uneven parts with SAP2000 (Figure 4.17) automatically creating the joints between two sections. Each section on the frame was assigned hinges at both ends except the beam column connection which was assumed to be rigid at half the height of the element perpendicular to each member. The rigid span on both the beam and the column were set to be automatically computed by the computer program. The support of the frame was set to restrain translations and rotatons in all directions. The loads assigned on the frame were dead loads from the beam (distributed loads) and the points load from the assumed upper storey which was the experimental load assigned on the columns.

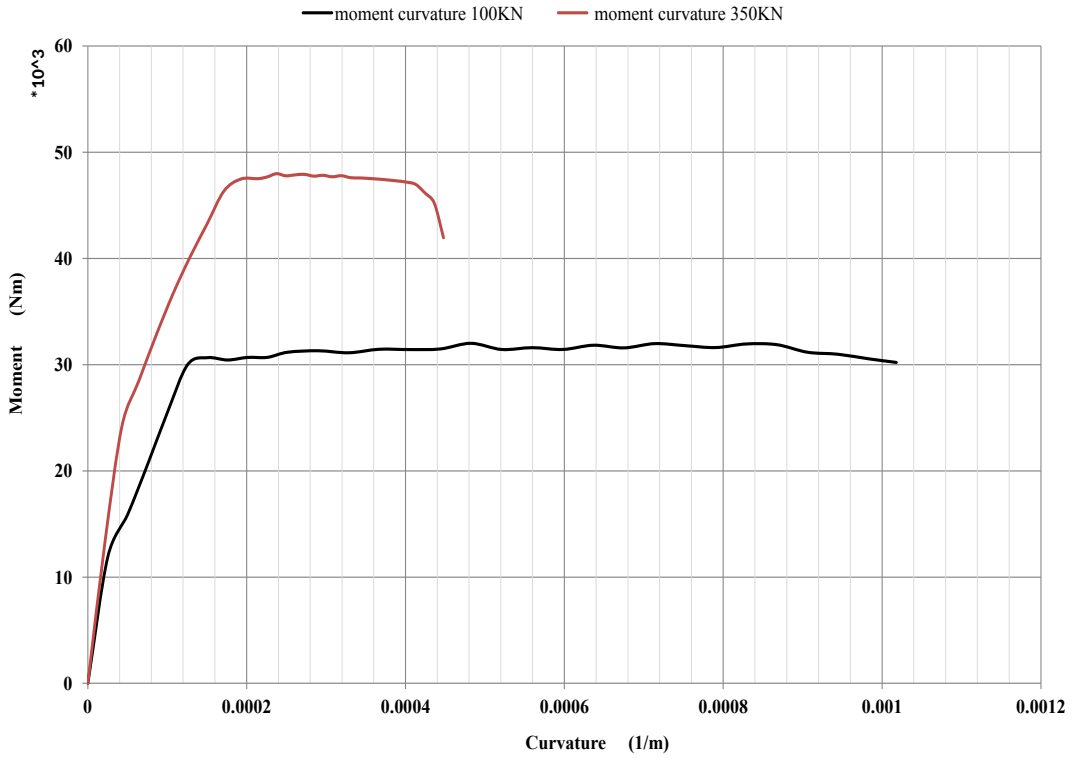

(a)

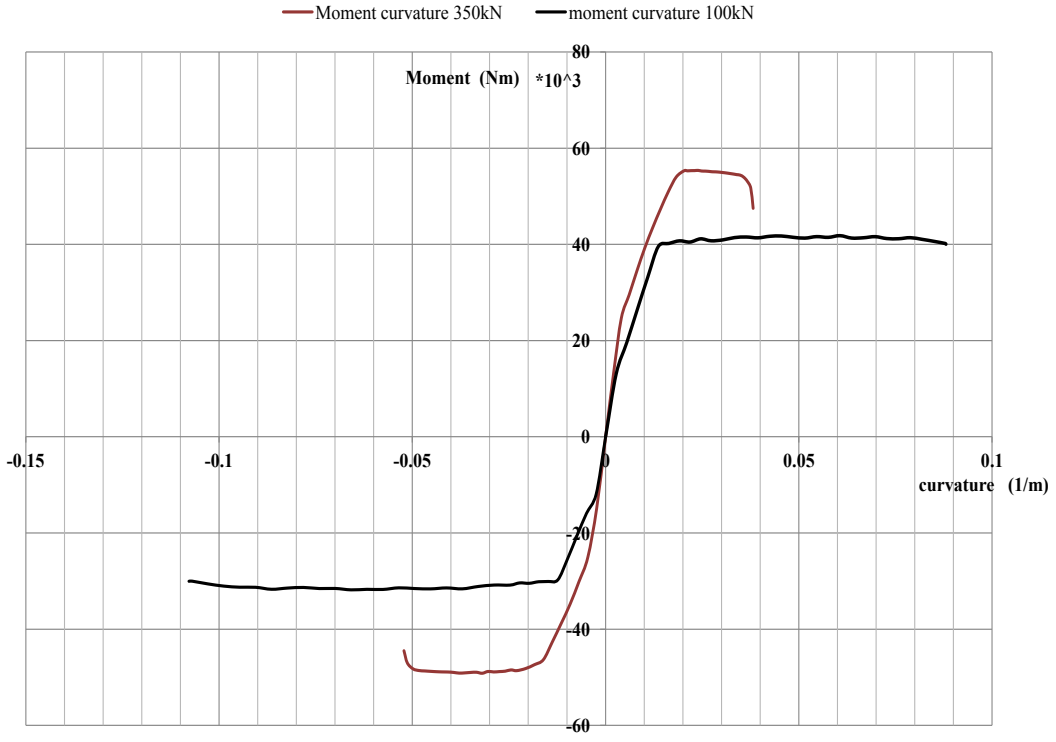

(b)

Figure 4.15: Moment curvature,M_3 of column sections: (a)Lower column section & (b) Upper column section

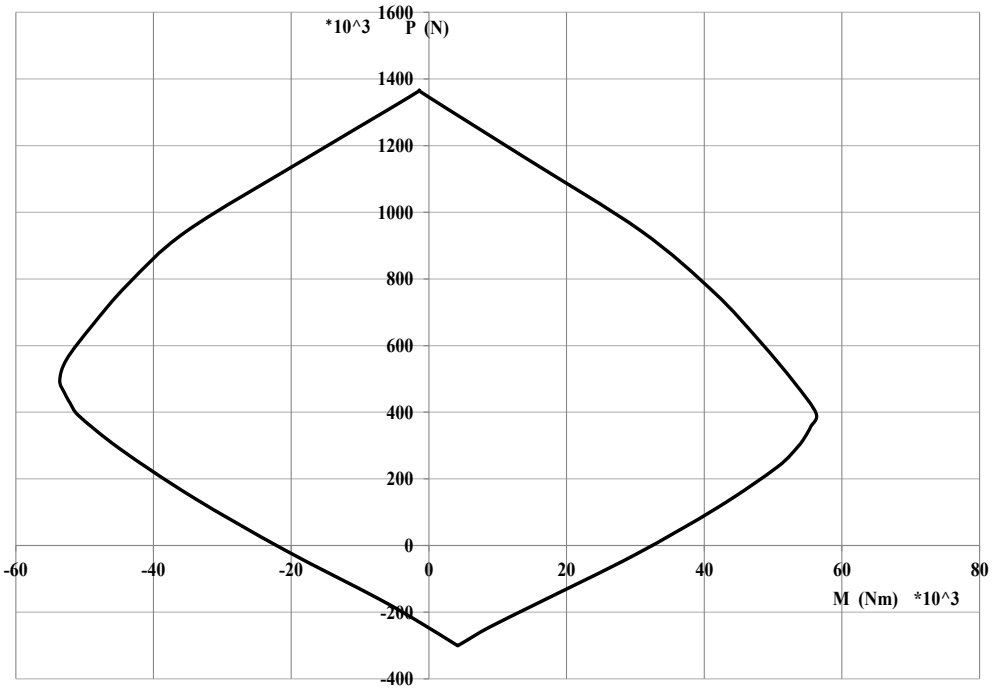

(a)

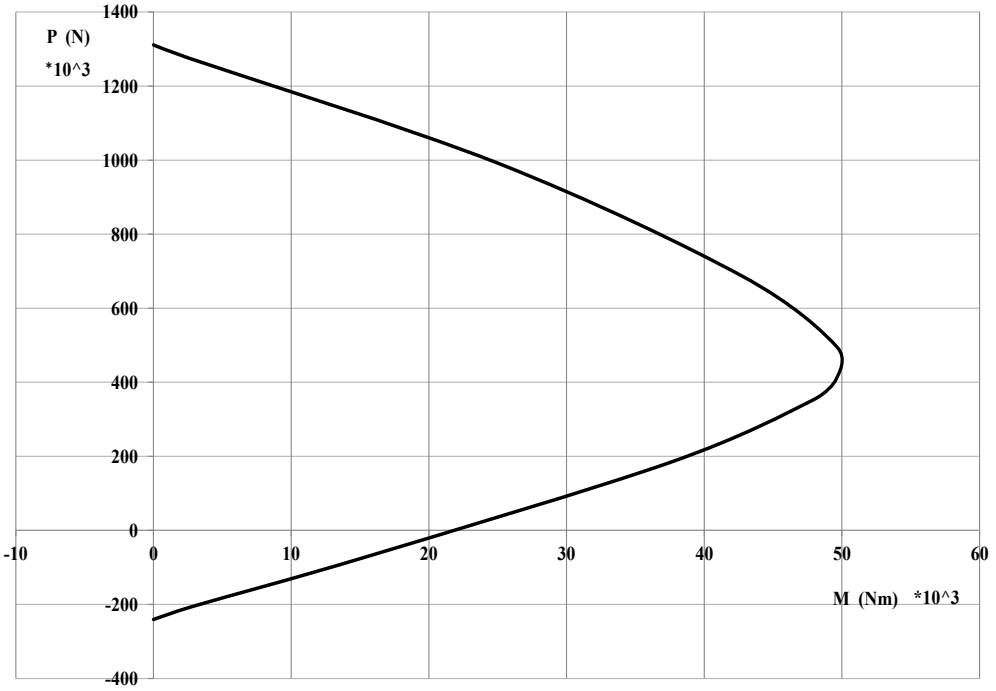

(b)

Figure 4.16: Axial force, P - Moment, M_3 interaction curves of column sections: (a)Upper column section & (b) Lower column section

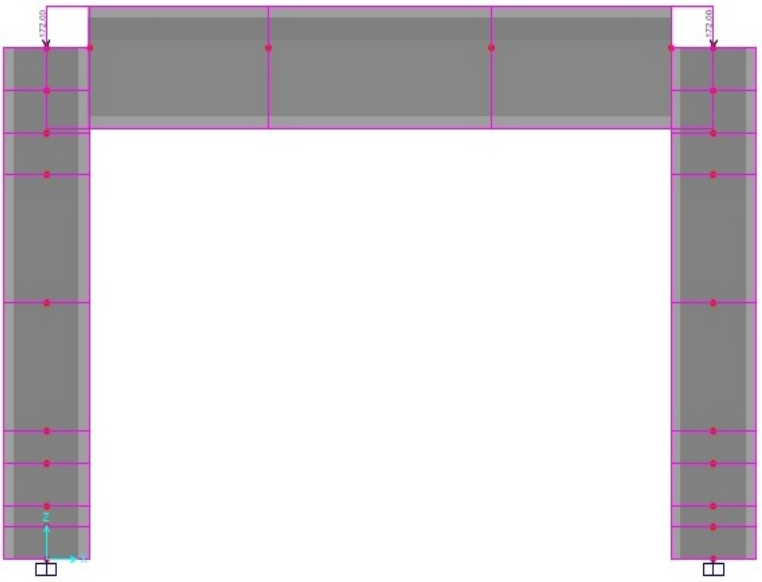

Figure 4.17: Frame Model

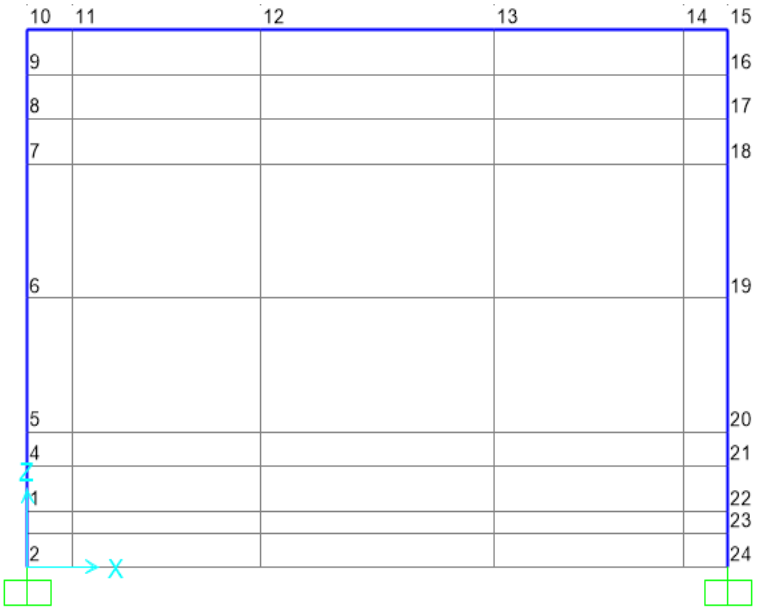

Figure 4.18: Frame Model

The sections were considered to have unmodified sectional properties (uncracked

flexural rigidity) which is discussed in Section 4.2.3. In this section of the theoretical works, cracked flexural rigidity was assigned to some sections using property modifiers at a plastic hinge length from the column ends. The static nonlinear pushover analysis was conducted considering first order theory of analysis with constant gravity loads as the initial conditions of the load increments and imposed incremental displacements. The analytical results of the program is given in the graph shown in Figure 4.19.

4.1.3.4 Analytical Results

The results of the pushover analysis is given in Figure 4.19. The black marked points indicate the yielding points of sections and the red marked ponts indicate sections that exceeded their ultimate rotational capacity. The first section to reach its yielding state (yielding of reinforcements) is section 2 which is the bottom of the left column as shown in Figure 4.18. The target lateral displacement at the yielding point and the corresponding base shear is 6.7 mm at 92 kN force respectively. This was procceded by the yielding of reinforcements at section 8 and 23 at a displacement of 8.17 mm with a base shear of108.4 kN and 8.57 mm with a base shear of 111.029 kN force respectively.

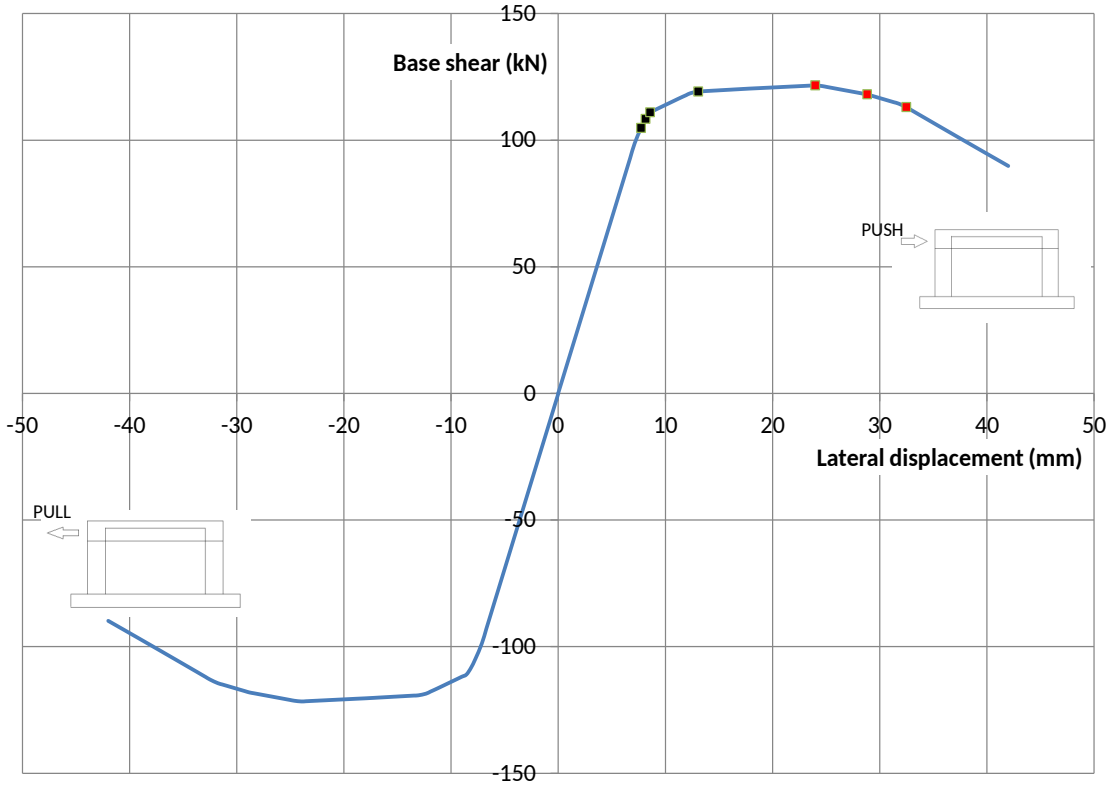

Figure 4.19: Force- displacement cuvre from the SAP2000

Although section 2 was first to reach its yielding flexural capacity, section 23 (the bottom of the right column) is observed to have first exceeded its ultimate sectional deformation capacity at a target displacement of 24.6 mm with a base shear of 121.398 kN force as shown in Figure 4.20(c) where yellow represents the collapse level of any section. The collapse state of all the hinges in Figure 4.20(d) occured at a target displacement of 32.5 mm with a base shear of 113 kN.

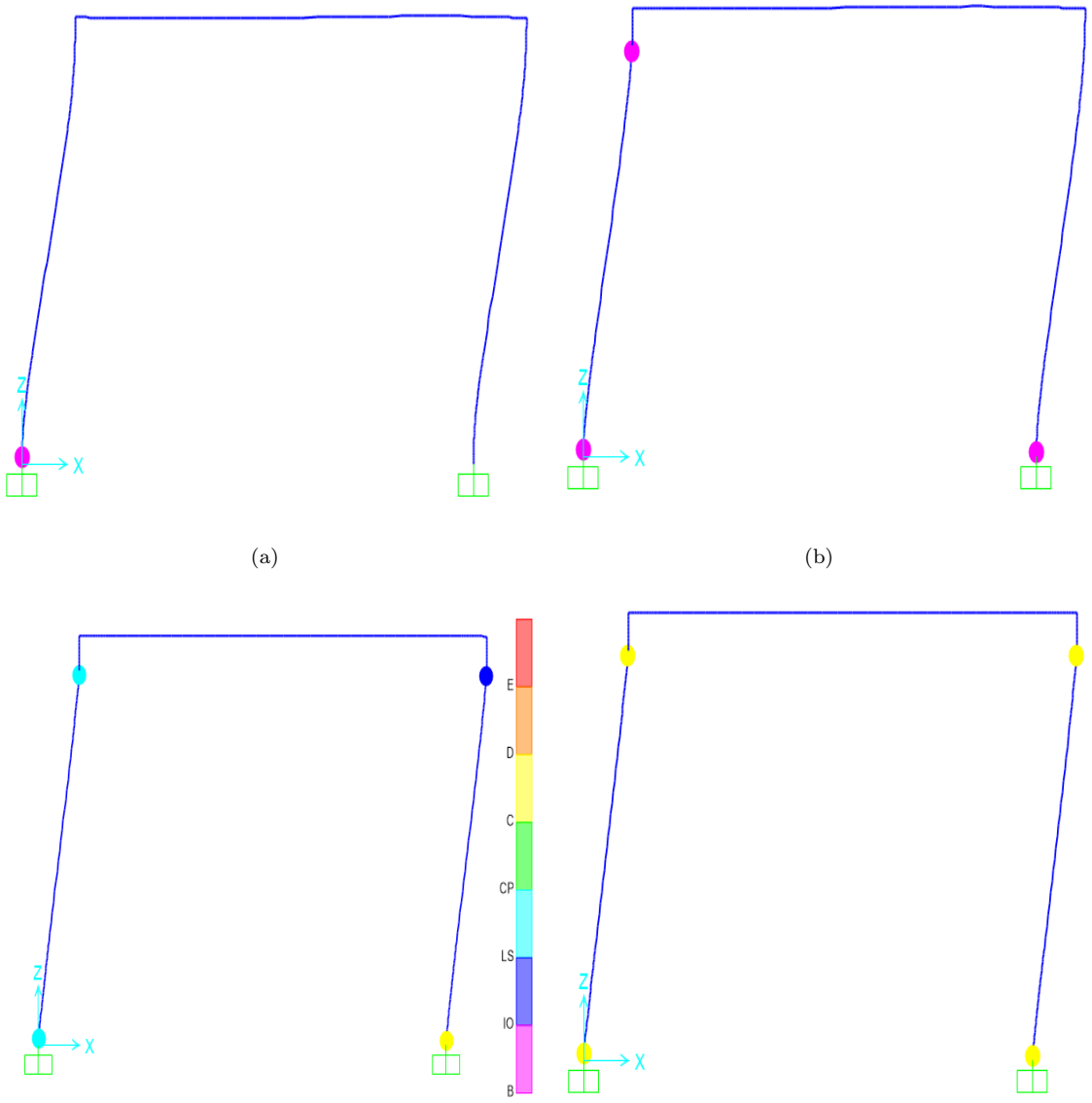

Figure 4.20: Damage states of the analytical model in SAP2000

Depending on the definition of the failure state of the structure, the ultimate structural displacement and structural ductility can be defined. In this case, the ultimate structural displacement of the sturcture is defined as the first occurance of any sectional collapse during the analysis, hence the ultimate displacement is 24.6 mm and the corresponding structural displacement ductility, μ is 4.1 while the experimental structural displacement ductility, μ is obtained to be 4.

4.1.4 Numerical Calculations

A numerical solution was performed by hand considering an axial force of 180 kN on each column. The axial force corresponds to half of the dead weight of the beam and 20% of the axial capacity of the column. The moment curvature of the column sections were obtained by considering the axial force on the columns but the moment curvature of the beams were obtained by with zero axial force. Figure 4.22 illustrates the respective moment curvatures and its idealized form. The idealized moment curvature was draw according to the caltrans specifications [40]. The cracked sectional rigidity is normally taken as a fraction of the uncracked rigidity. Priestly and Paulay [39] suggested that this fraction for rectangular beam, T beams and columns are 0.4 , 0.35 and between 0.4 - 0.8 respectively. For the columns, it is a factor of the intensity of the axial load.

According to the Turkish earthquake code TSC[24], the effective rigidity of the columns should be taken as 40% of its uncracked rigidity. Similarly, the effective rigidity of the beams are to be taken as 50% of the uncracked rigidity. In this present study,the moment curvature relationship was known hence the cracked flexural rigidity was obtained directly from the load-deformation curve relationship of each potential hinge formation section by using equation 4.4.

$$EI_{eff} = \frac{M_y}{X_y} \tag{4.4}$$

The beam was divided into three sections because of the use of bent bars and the assumed moment diagram is not totally positive along the beam in Figure 4.21. Hence both uncracked flexural rigidity of negative and positive moment curvature were assigned to the beam elements accordingly depending on the sign of the moment. The cracked flexural rigidity was not considered in the beams because the beams of the frame understudy are stronger than the columns hence the potential plastic hinge formation will only occur on the columns.

In the columns, the idealized moment curvature was used in the analysis. The moment diagram of a positive lateral load analysis can be seen in Figure 4.21.

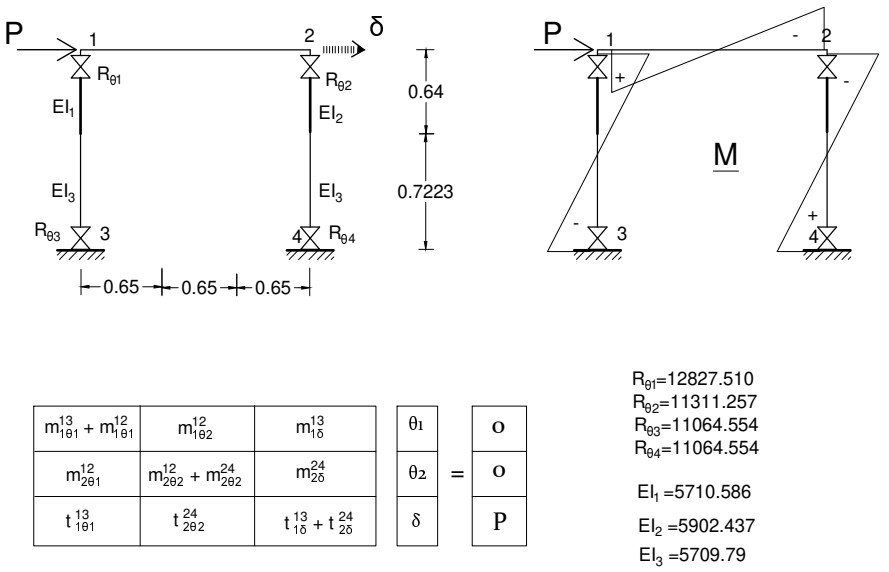

Figure 4.21: Representation of the frame

For sections with negative moments, the negative uncracked flexural rigidity was assigned and vice versa for positive moments. Semi rigid connections were used to represent weaken sections at the ends of the column at a plastic hinge length, L_p computed from equation 4.5 defined by Priestly and Paulay [39] and the value of the stiffness of semi rigid connections, R, was found by equation 4.6.

$$L_P = 0.08 \times L + 0.022 \times d_b \times f_y \tag{4.5}$$

$$R_\theta = \frac{EI_{eff}}{L_P} \tag{4.6}$$

The member stiffness of each column could be obtained by considering three methods:

1. Using inertia forces at member ends (applying 1 unit rotation at each end to obtain the flexibility matrix) the inverse of the flexibility matrix gives the stiffness matrix.

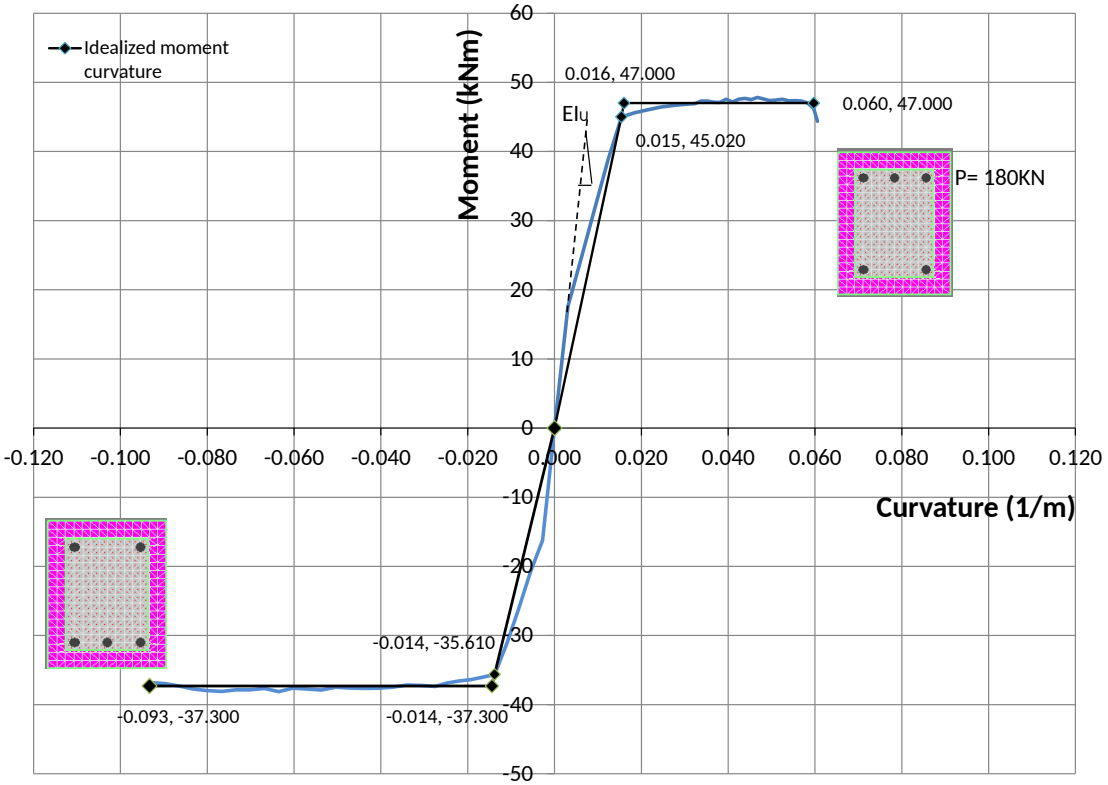

(a)

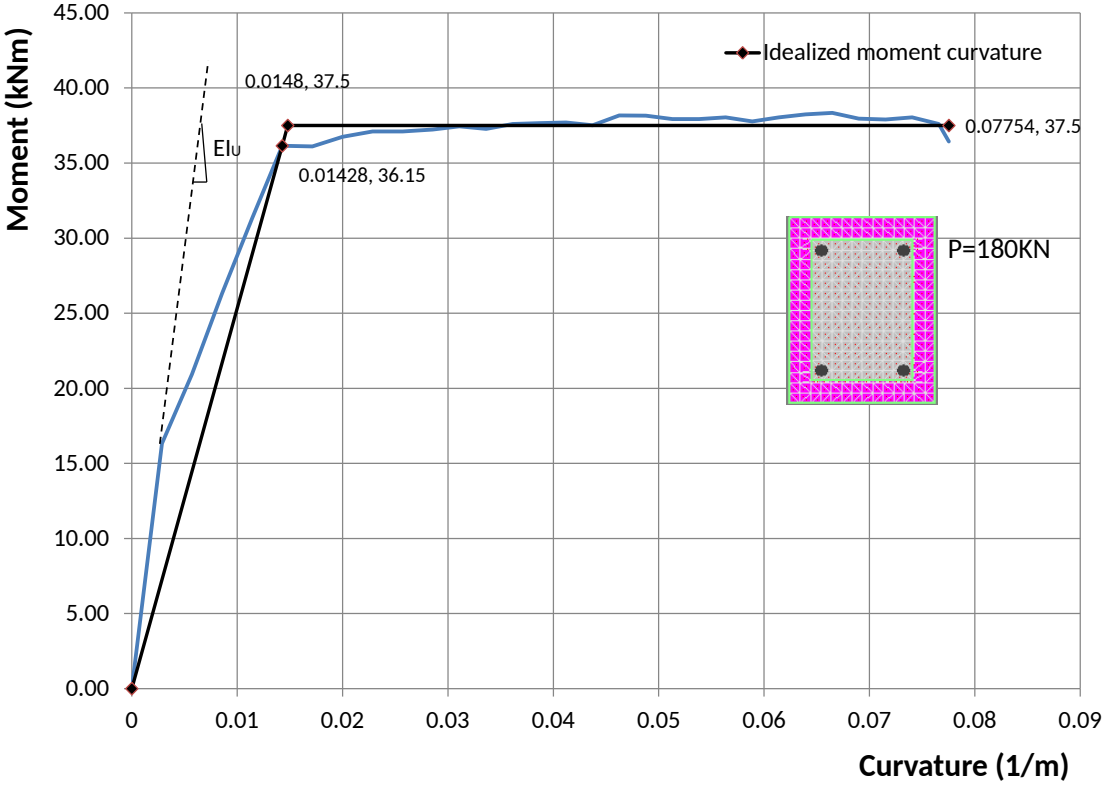

(b)

Figure 4.22: Moment curvature at P=180kN: (a)Upper column section & (b) Lower column section

2. Imposing support settlements at the column ends. The moments derived contributes to the stiffness matrix corresponding to the location on the support settlement. This was performed in DC2B.

3. Treating the column as a structure and eliminating the stiffness contribution of interior nodes.

The member stiffness of the beam was obtained from the first method. All three alternatives produced the same stiffness matrix in the column. The steps used in the numerical analysis is given below:

1. Each member stiffness was derived and the structural coefficient stiffness matrix in Figure 4.21 was determined and reduced by Gaussian elimination.

2. A unit load was imposed to determine the displacement (yield displacement) needed to cause the first plastic hinge.

3. A displacement increment from the yield displacement is then imposed and the moments at critical sections are determined.

4. If the moment obtained at any section is higher than the ultimate moment an iteration is performed on the rigidity (displacement unaltered), which changes the value of the stiffness of the semi rigid connections hence affecting the structural stiffness, until the moment is approximately equal to the ultimate moment of that section.

5. Analysis continues until all sections reach their ultimate rotation capacity.

This type of structural analysis affects the values of the semi rigid connections while the formation of hinges method adds a new row and a column together with one unknown and the ultimate moment as an external force to the structural stiffness matrix each time a hinge is formed. The results of the hand calculation is discussed in the proceeding chapters.

4.1.5 Concentrated plasticity - 1st technique

Concentrated plasticity is the accumulation of plastic deformations at a section while the remaining sections along the structural elements remains in its elastic state. The plastic deformation can be either due to bending, shear or axial force. In nonlinear analysis of structures, when sections of the structural elements exceed their yield limit, the plastic deformations are modelled as concentrated plastic hinges at the ends of the element. Often, when considering the lumped plasticity, semirigid connections are used which literally means including springs in the model at the end connections. This study takes into account the plastic deformation in only bending.

An algorithm is developed to perform the nonlinear static incremental lateral load analysis where the hinge formations are considered to occur at the ends of critical sections of the element. This algorithm is limited to a one bay, one storey structure with weak column strong beam concept as in the frame used in the experimental work.

Force controlled load increment is considered to be best applied in the elastic phase of the pushover anaysis of a structure while displacement control is known to be best considered in the inelastic phase of the stucture during load increments as seen in a typical force-displacement diagram in Figure 4.23. For a better comparison, the first aim of this algorithm is to compare the lateral response of the frame with concentrated hinges by force control and displacement-control analysis and secondly to determine the difference between in the structural response when the semi-rigid hypothesis is considered and the concentrated plastic hinge hypothesis of the frame in pushover analysis.

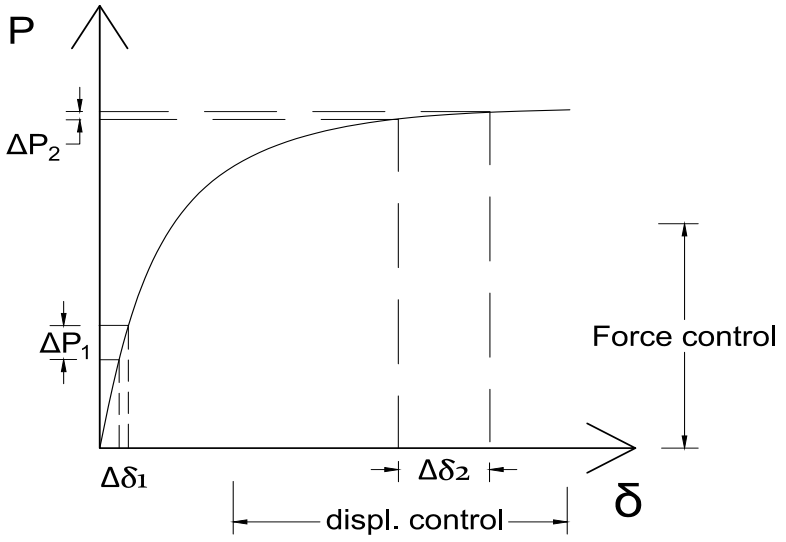

Figure 4.23: A typical force-displacment curve

4.1.5.1 Moment Curvature Relationship

By the use of material nonlinear stress-strain relationship, a defined moment curvature which represents the actual load deformation behavior of reinforced concrete sections is used. As mentioned earlier, the moment-curvature relationship can directly provide the cross-sectional stiffness. The sectional rigidity depends on the intensity of the axial load and the bending moment hence for a particular intensity of axial load and moment curvature, the cross-sectional rigidity is evaluated. The bi-linearized moment curvature used in this algorithm for expressing the nonlinear behavior of reinforced concrete section is given in Figure 4.24. The moment curvature relationship is obtained through Xtract and bilinearized with no strain hardening. It is assumed that the axial force is so small that its effect on the moment is neglected.

4.1.5.2 Flexibility Matrix

The flexibility matrix of each member is obtained by force method. From equation 4.7, the flexibility matrix is derived where M_i(x) and M_j(x) are the moment

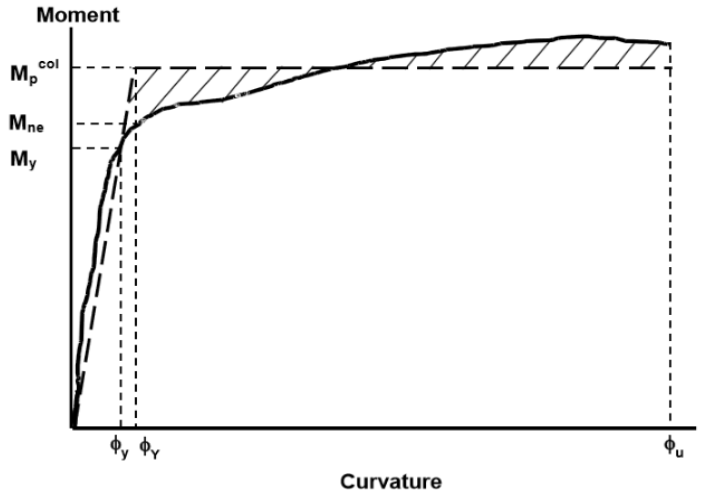

Figure 4.24: Assumed Bilinearized moment curvature relationship

distribution along the element due to a unit moment at node i and j respectively.

$$\delta_{ii} = \int_a^b M_i \frac{M_i}{EI} ds \quad \delta_{ij} = \int_a^b M_i \frac{M_j}{EI} ds \quad \delta_{jj} = \int_a^b M_j \frac{M_j}{EI} ds \tag{4.7}$$

By force method, for a member with both ends fixed has three redundant force hence making it statically indeterminate. The primary structure (statically determinate) of the member is decided and the three redundant unknowns are imposed individually unto the structures as unit loading as seen in Figure 4.25. The limits of the integral(a,b) in equation 4.7, depends on the rigidity along the span of the member.

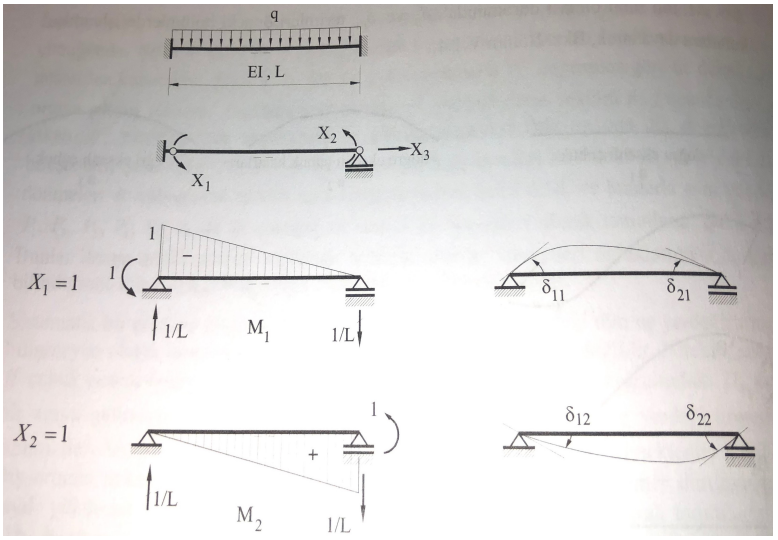

Figure 4.25: Flexibility matrix by force method

Considering the integral given in 4.7, to find the flexibility matrix, [f] due to the unit rotation at nodes 1 and 2, assuming the rigidity is constant along the span, the following integral in equation 4.9 can be derived.

$$[f] = \left[\begin{array}{c|c} \delta_{11} & \delta_{12} \\ \hline \delta_{21} & \delta_{22} \end{array}\right] \tag{4.8}$$

$$\delta_{11} = \int_0^L M_1 \frac{M_1}{EI} ds \quad \delta_{12} = \int_0^L M_1 \frac{M_2}{EI} ds \quad \delta_{22} = \int_0^L M_2 \frac{M_2}{EI} ds \tag{4.9}$$

δ_{21} is equal to δ_{21}. the inverse of the flexibility matrix [f] is the corresponds to the stiffness of the member due to the unit moment X_1 and X_2 shown in figure 4.25

4.1.5.3 Structural Coefficient Stiffness Matrix

Slope-deflection method is used in this algorithm. It relates end moments of members to their corresponding rotations and displacements. This method considers the deflection as the primary unknowns, while in the force method, the

primary unknowns as redundant forces. Flexural deformation is considered in this analysis by slope deflection method. Kinematically indeterminate structures correspond to the slope deflection method while statically indeterminate structures correspond to the force method.

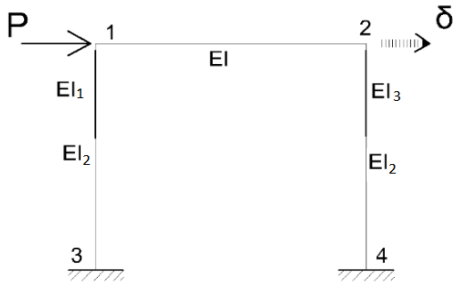

Figure 4.26: One bay one storey frame used in the algorithm

Slope deflection method is used to obtain the equilibrium equations of the structure by considering the relevant displacements on the structure. The structural matrix is assembled using the slope deflection equations which are the moment equilibrium equations and force equilibrium equation in the direction of the x-axis. For a one bay one storey portal frame and considering the assigned nodes in Figure 4.26, the following equilibrium equations can be written;

$$\sum M_1 = 0; \quad (m_{1\theta_1}^{1-3} + m_{1\theta_1}^{1-2})\theta_1 + m_{1\theta_2}^{1-2}\theta_2 + m_{1\delta}^{1-3}\delta = 0 \tag{4.10}$$

$$\sum M_2 = 0; \quad (m_{2\theta_2}^{2-4} + m_{2\theta_2}^{2-1})\theta_2 + m_{2\theta_1}^{2-1}\theta_1 + m_{2\delta}^{2-4}\delta = 0 \tag{4.11}$$

$$\sum F_x = 0; \quad t_{1\theta_1}^{1-3}\theta_1 + t_{2\theta_2}^{2-4}\theta_2 + (t_{2\delta}^{2-4} + t_{1\delta}^{1-3})\delta = P \tag{4.12}$$

4.1.5.4 Matrix Inverse by Partitioned Matrix Technique

For an assembled square stiffness matrix [A] of size n×n, the inverse can be determined by the inverse partitioning matrix technique. If the required inverse

matrix is $[B]_{n\times n}$ as shown below; the matrix [A] must be partitioned into 4 parts namely, $[A_{11}], [A_{12}], [A_{21}]$ and A_{22}.

$$[A] = \left[\begin{array}{ccc|c} a_{11} & a_{12} & \cdots & a_{1n} \\ a_{21} & a_{22} & \cdots & a_{2n} \\ \vdots & & \ddots & \vdots \\ \hline a_{n1} & a_{n2} & \cdots & a_{nn} \end{array}\right] = \left[\begin{array}{c|c} [A_{11}] & [A_{12}] \\ \hline [A_{21}] & A_{22} \end{array}\right] \tag{4.13}$$

$$[B] = \left[\begin{array}{c|c} [B_{11}] & [B_{12}] \\ \hline [B_{21}] & B_{22} \end{array}\right] = [A]^{-1} \tag{4.14}$$

$[A_{11}]$ is a symmetric matrix of size n-1 by n-1, $[A_{12}]$ is a vector of size n-1 $\times 1$, $[A_{21}]$ is the transpose of $[A_{12}]$ and $[A_{22}]$ is a single number at the nth row of the nth column. Several calculation steps are made to compute the elements in the inverse matrix. The following equations will be used.

$$[X] = [A_{11}]^{-1} \times [A_{12}] \tag{4.15}$$

$$[Y] = [A_{21}] \times [A_{11}]^{-1} \tag{4.16}$$

$$[Z] = [A_{22}] \times [A_{11}]^{-1} \tag{4.17}$$

$$[B_{11}] = [A_{11}]^{-1} + [X] \times [Z]^{-1} \tag{4.18}$$

$$[B_{21}] = -[Z]^{-1} \times [Y] \tag{4.19}$$

$$[B_{12}] = -[X] \times [Z]^{-1} \tag{4.20}$$

$$[B_{22}] = [Z]^{-1} \tag{4.21}$$

The sizes of the partitioned matrix can be same as the indicated sizes or smaller, but the smaller the size of A_{22} the more effective the technique. As seen in equation 4.15, the inverse of A_{11} is required for subsequent computations. The

order of multiplication and adiition should be exactly as shown in equations 4.15-4.21 .

4.1.5.5 Method of Analysis

i) **Force Controlled Pushover Analysis**

In this Pushover analysis strategy, the increments is done an external force (Figure 4.23) prescribed to the structure through the elastic and inelastic response on the struture until a section exceedes its ability to deform. The external force applied to the structure is indicated as P. The steps used in the nonlinear analysis are described below and illustrated by the flow chart in Figure 4.28.

(a) Element stiffness matrices are defined depending on the order of analysis is to be considered.

(b) The lateral load, P is intialized as 1 kN. To capture both the elastic behavior during the initial stages and plastic behavior of the member sections during loading before collapse, the incremental loads, ΔP is taken randomly small.

(c) By slope deflection method of analysis, assemble the structural coefficient stiffness matrix [A] from equations 4.10, 4.11 and 4.12.

(d) The inverse of the coefficient stiffness matrix, $[A]^{-1}$ is found from equations 4.15 - 4.21 by calling the inverse subroutine .

(e) Compute the nodal displacements ,[d] and the internal moments.

$$[d]_{n\times 1} = [F]_{n\times 1} \times {[A]_{n\times n}}^{-1} \tag{4.22}$$

(f) Compute the load factor μ, at each nodal point by dividing the sectional moment capacity by the internal nodal moment computed at a specific node of a member. Assume the smallest load factor is the force causing the formation of the first plastic hinge, $P = \mu$.

(g) With the occurrence of a plastic hinge, a new slope deflection equation is developed considering a new unknown rotation at that specific hinge formation location. Add the set of current equations to the coefficient matrix on a new row and column. A typical example is shown in Figure 4.27 and the equivalent modified structural coefficient stiffness matrix is shown in 4.24.

(h) Increase the magnitude of the lateral load and analyze the frame to determine the internal forces and corresponding lateral displacements.

(i) The algorithm shown in Figure 4.28 terminates when the rotational stiffness of the any critical section has reached its ultimate rotational capacity and if it occurs prior to column mechanism.

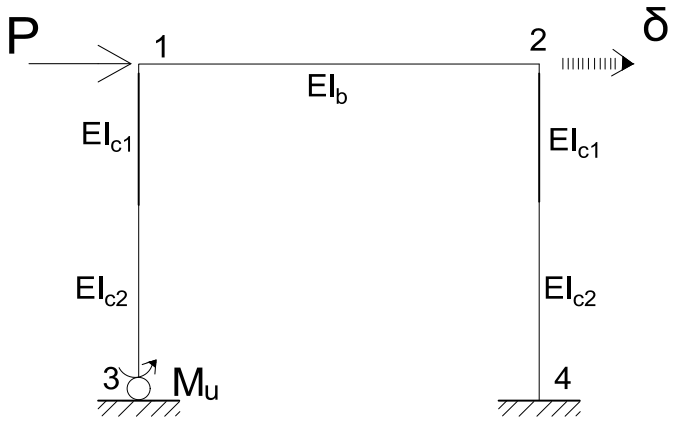

Figure 4.27: Formation of a plastic hinge at node 3 (plastic hinge hypothesis)

$$\left[\begin{array}{c|c|c||c} m_{1\theta_1}^{1-3}+m_{1\theta_1}^{1-2} & m_{1\theta_2}^{1-2} & m_{1\delta}^{1-3} & m_{3\theta_1}^{3-1} \\ \hline m_{2\theta_2}^{2-4}+m_{2\theta_2}^{2-1} & m_{2\theta_1}^{2-1} & m_{2\delta}^{2-4} & 0 \\ \hline t_{1\theta_1}^{1-3} & t_{2\theta_2}^{2-4} & t_{2\delta}^{2-4}+t_{1\delta}^{1-3} & m_{3\delta}^{3-1} \\ \hline\hline m_{3\theta_1}^{3-1} & 0 & m_{3\delta}^{3-1} & m_{3\Theta_3}^{3-1} \end{array}\right] \left[\begin{array}{c} \theta_1 \\ \hline \theta_2 \\ \hline \delta \\ \hline\hline \Theta_3 \end{array}\right] = \left[\begin{array}{c} 0 \\ \hline 0 \\ \hline P \\ \hline\hline M_u \end{array}\right] \quad (4.23)$$

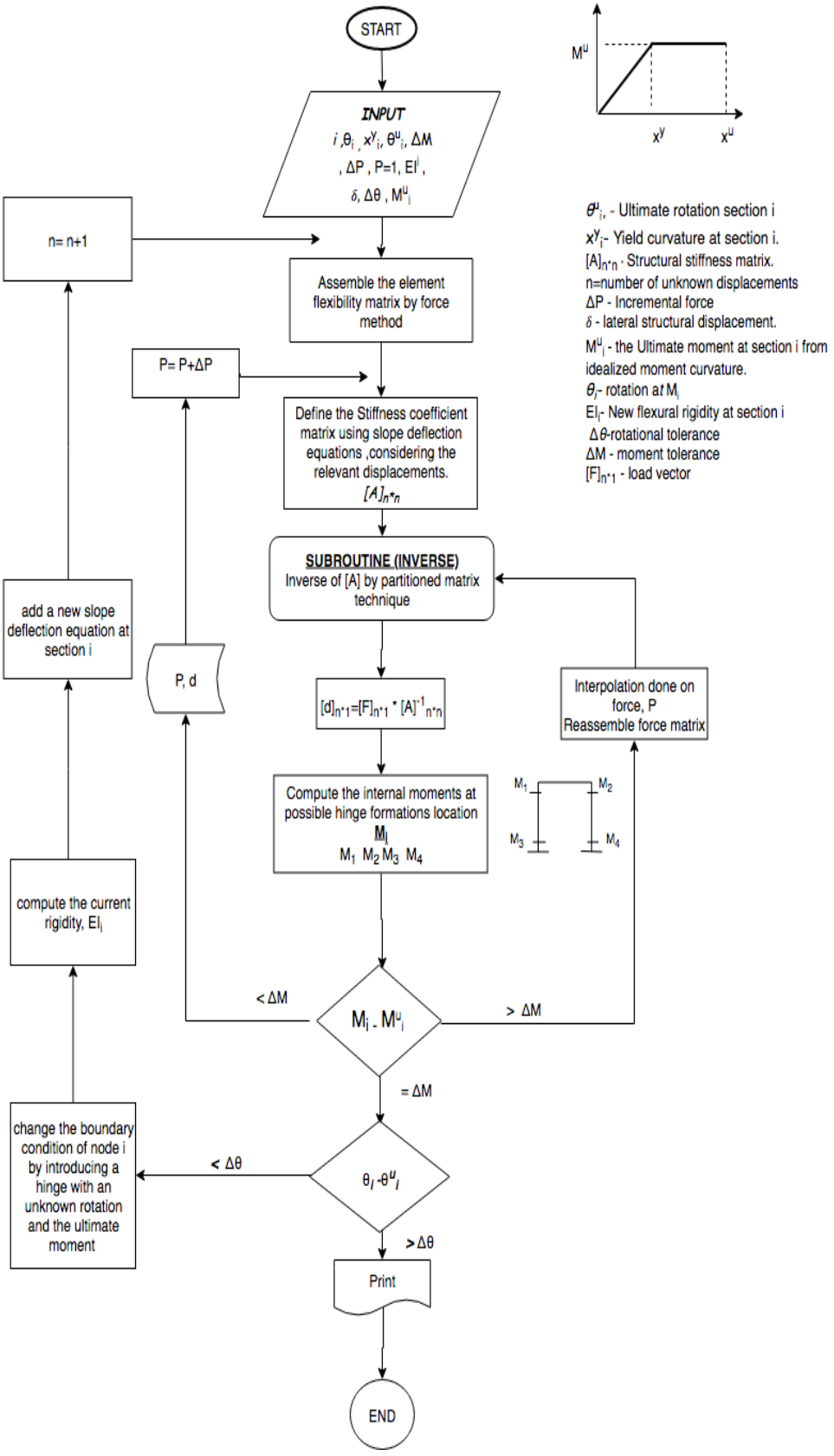

Figure 4.28: Flowchart for force control lateral load increment (plastic hinge hypothesis)

ii) **Displacement Controlled Pushover Analysis**

Displacement controlled non-linear incremental load analysis, the incremental parameter prescribed to the structures is displacement through out the the elastic and inelastic behaviour of the structure. This method of analysis is known to be very useful when nonlinearity begins in the pushover curve because at a small incremental force, the change in displacement increases (Figure 4.23). Based on a literature review, displacement method gives a better solution for nonlinear problems because it portrays great stability at critical sections. The steps used is the nonlinear analysis are described below:

(a) Element stiffness matrices are defined depending on the theory of analysis.

(b) The target displacement, δ is intialized as 0. To capture both the elastic behavior during the initial stages and plastic behavior of the member sections during loading before collapse, the incremental loads, $\Delta\delta$ is taken randomly small.

(c) By slope deflection method of analysis, assemble the coefficient structural stiffness matrix, [A] from equations 4.10, 4.11 and 4.12.

(d) Full Gaussian elimination is then performed on the coefficient matrix and the force matrix to determine the unknown lateral force at a specific target displacement.

$$\left[\begin{array}{c|c|c} \overline{A_{11}} & \overline{A_{12}} & \overline{A_{13}} \\ \hline 0 & \overline{A_{22}} & \overline{A_{23}} \\ \hline 0 & 0 & \overline{A_{33}} \end{array}\right] \quad \left[\begin{array}{c} \theta_1 \\ \hline \theta_2 \\ \hline \delta \end{array}\right] = \left[\begin{array}{c} 0 \\ \hline 0 \\ \hline P \end{array}\right] \tag{4.24}$$

(e) Compute the nodal displacements [d] by back substitution and the internal moments. Check if any critical section has not exceeded its ulimate maoment capacity.

(f) With the occurrence of a plastic hinge (M=M_u), a new slope deflection equation is developed considering a new unknown rotation at that

specific hinge formation location. Add the set of current equations to the coefficient matrix on a new row and column as shown in the matrix form 4.24.

(g) Increase the magnitude of the lateral displacement, and analyze the frame to determine the internal forces and corresponding base shear. Repeat Steps (d) and (f).

(h) The program is terminated after a column mechanism has occurred but the algorithm shown in Figure 4.28 terminates when the rotational stiffness of any critical section has reached its ultimate rotational capacity and if it occurs prior to column mechanism.

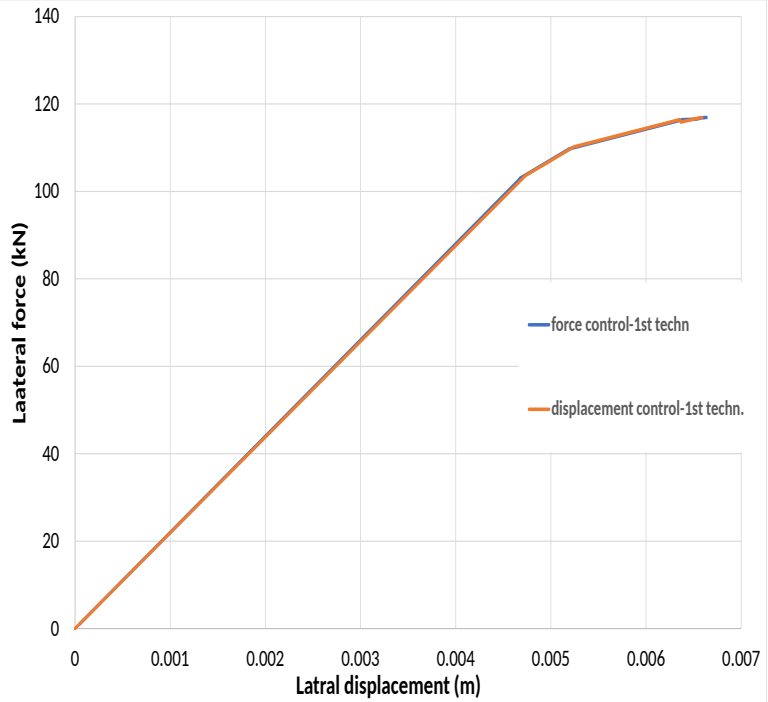

Figure 4.29: Force displacement curve (first technique

When comparing the results of the displacement controlled factor and the force control parameter, it is observed that there was no difference in this technique. At all target loads the resulting force or displacement was same for both analysis. The reason behind this similarity is because all elements are in their elastic

states. The analysis could not capture the post-elastic force deformation state of the sections. The analysis ended immediately the any section deformation has exceeded its ultimate deformation capacity.

4.1.6 Concentrated plasticity -2nd technique

This technique deals with the semi-rigid hypothesis, where the nonlinearity of sections at the ends of members are modelled as semi-rigid connections with zero length. The plasticity of the sections are accummulated at the semi-rigid connections.The basic concept of this technique is treating a section of a member with a potential formation of a plastic hinge as a semi-rigid connection. With this selected connection, during pushover analysis, the change in the rigidity of the section at any deformation state can be implemented in the stiffness of this connection to capture the structural behaviour both in the elastic and plastic phase.

Considering the frame understudy with weak column and strong beam, the semi-rigid connections will be considered for the potential plastic hinge locations at the column ends. A general algorithm was developed through Matlab for the non-linear analyisis (static push-over analysis) of the structure. The static push-over analysis considered in this algorithm is a nonlinear analysis where the lateral loads (displacement controlled) are increased monotonically while under constant gravity loads until the rotational capacity of any member section reaches its ultimate value. To validate the results obtained, hand calculations and DC2B computer program is utilized. For a better comparison of both techniques, the moment curvature was chosen to be the same as the first technique (bilinearized moment curvature with no strain hardening). First order lateral load increments, second order analysis for obtaining the stability loads and a second order theory of lateral load incremental analysis considering material nonlinearity will be studied in this section.

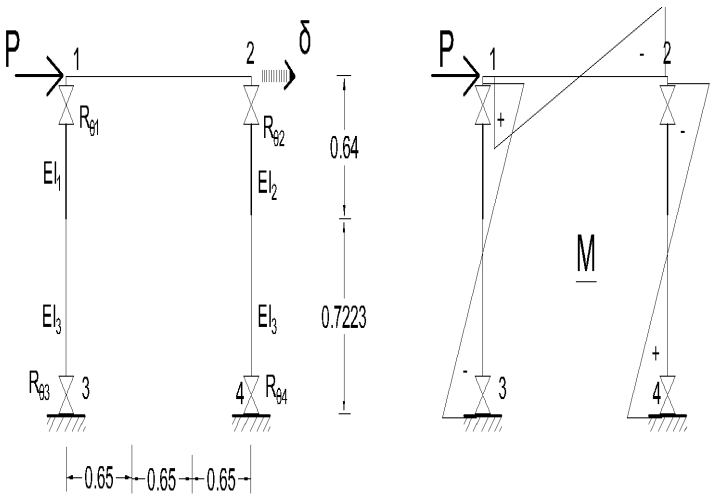

Figure 4.30: Frame with semi-rigid connection

4.1.6.1 First order theory

In first order theory, the axial loads acting on the columns of the structure is considered not effective on the structural stiffness hence the flexibility parameters of all elements are independent of gravity loads. By force method, the flexibility parameters for a member with both ends fixed has three redundant force hence making it statically indeterminate as explained in the previous technique. The difference between the flexibility parameters considered in this technique with that of the previous is the contribution of the plasticity of semi-rigid connections. The same procedure is used by obtaining the primary structure (statically determinate) of the member and having the three redundant unknowns imposed individually onto the structures as unit loading shown in Figure 4.31. Mechanical properites (flexibility parameters) in equation 4.25 are found by performing an integration along the span of the element, which is very useful for members with varying rigidity along its span.

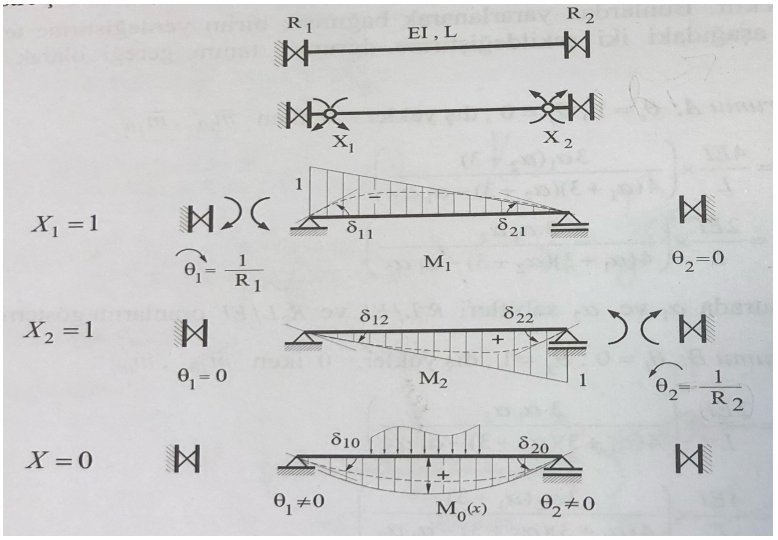

Figure 4.31: Flexibility matrix by force method for memebrs with semi-rigid connections

$$f_{11} = \int_0^L M_1 \frac{M_1}{EI} ds + \frac{1}{R_1} \quad f_{12} = \int_0^L M_1 \frac{M_2}{EI} ds \quad f_{22} = \int_0^L M_2 \frac{M_2}{EI} ds + \frac{1}{R_2} \tag{4.25}$$

$$\begin{gathered} f_{11} = \frac{L}{3EI} + \frac{1}{R_1} \quad f_{12} = (-)\frac{L}{6EI} \\ f_{22} = \frac{L}{3EI} + \frac{1}{R_2} \end{gathered} \tag{4.26}$$

Considering an member with fixed - fixed ends, when transitioning to a member with semi-fixed and fixed end (due to a plastic hinge on one end) and a member with semi - fixed and semi - fixed end (due to a plastic hinge on both ends), an element with the rigidity of the rotational stiffness of the semi-rigid connection at a relatively small distance is considered to represent the semi-rigid connection. Equation 4.27 represent a structural element with one semi-rigid end and equation 4.28 represents structural elements with semi-rigid connections at both ends, if

the same technique is applied.

$$
\begin{aligned}
m_{i_{\theta_i}} &= \frac{4EI}{L} \times \frac{\alpha}{\beta} \\
m_{i_{\theta_j}} = m_{j_{\theta_i}} &= \frac{2EI}{L} \times \frac{\alpha}{\beta} \\
m_{j_{\theta_j}} &= \frac{4EI}{L} \times \frac{\alpha + 3}{\beta}
\end{aligned}
\tag{4.27}
$$

$$
\begin{aligned}
m_{i_{\theta_i}} &= \frac{4EI}{L} \times \frac{3\alpha_1(\alpha_2 + 3)}{4(\alpha_1 + 3)(\alpha_2 + 3) - \alpha_1\alpha_2} \\
m_{i_{\theta_j}} = m_{j_{\theta_i}} &= \frac{2EI}{L} \times \frac{3\alpha_1\alpha_2}{4(\alpha_1 + 3)(\alpha_2 + 3) - \alpha_1\alpha_2} \\
m_{j_{\theta_j}} &= \frac{4EI}{L} \times \frac{3\alpha_2(\alpha_1 + 3)}{4(\alpha_1 + 3)(\alpha_2 + 3) - \alpha_1\alpha_2}.
\end{aligned}
\tag{4.28}
$$

where α=R/(EI/L) and $\beta = 4 + \alpha$. R_1 and R_2 are the rotational spring stiffness of the semi-rigid connections and it is defined as the sectional rigidity. For a member with constant rigidity along its span, equations 4.26 can be used. The corresponding stiffness parameters are given in equation 4.28 where α_1=R_1/(EI/L) and α_2=R_2/(EI/L) are the stiffness indeces of the flexural connections.

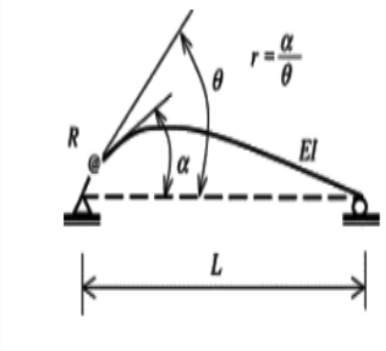

Figure 4.32: Rigidity factor of semi-rigid connection [41]

Incoporating the post elastic behaviour of a section when section property transitions from the linear state (fully rigid) to the nonlinear state (semi-rigid) in the

lateral load incremental analysis, the mechanical properties corresponding to that section is changed by correction factors [42]. The standard element stiffness matrix, S_e with rigid connection is modified by a correction matrix, C_e in Appendix B.2.

$$[K] = [S_e] \times [C_e] \tag{4.29}$$

With these correction factors, which uses the rigidity factor, r, the plastification of a section can be incoporated in the element stiffness matrix. Rigidity factor is the ratio of the rotation of the element to that of the semi-rigid connection as shown in Figure 4.32. The correction matrix, $[C_e]$, K and S_e are indicated in the appendix B.2 where r is defined in equation 4.30.

$$r = \frac{1}{1 + \frac{3EI}{RL}} \tag{4.30}$$

The rigidity-factor r, falls within the range of zero and one ($1 \geq r \geq 0$) while the rotational stiffness R varies between 0 and infinity. For a rigid connection, R=∞ making the rigidity factor, r=1 and for a pinned connection, R=0 making the rigidity factor, r=0, respectively. By taking on the nonlinear force-deformation relationship of a section that defines the change in rotational stiffness R under incremental loads, the effect of introducing a semi-rigid connection on the overall structural response can be studied. From Figure 4.33, if R=$\frac{dM}{d\varphi}$, then the range of R within the post elastic region (from yielding to plastification) varies from $\infty \geq R \geq 0$.

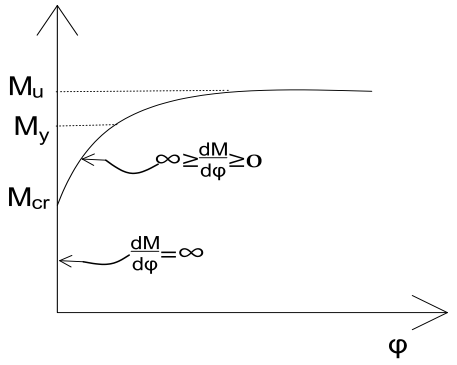

Figure 4.33: A typical post elastic load deformation relationship

where φ is considered to the rotational deformation of any reinforced concrete section. For the first order analysis, the following assumptions considered are:

- The material is nonlinear.
- The equations of equilibrium were written on the undeformed shape of the elements.
- The vertical loads are kept constant while the lateral loads are increased.

This analysis is performed to obtain the limit load according to the first order theory and to compare with the first technique of concentrated plasticity as discussed above. Since the rotational stiffness of the semi-rigid connections depends on the length of the plastic hinge, a parametric work was considered on the effect of the plastic zone length on the structural response in this theory.

4.1.6.2 Second order theory with material nonlinearity

Second order effects is considered when a structure is laterally loaded and with gravity loads on the column. The structure tends to sways hence creating a larger lateral translation of the frame in the direction of the applied lateral load causing an eccentricity for the vertical gravity loads which in turns creates additional moments at sections with moments.
Hence the well known element stiffness matrix is updated to include the geometric stiffness as seen in equation 4.31

$$K = K_e + G_e \tag{4.31}$$

$$K = K_e \times C_e + G_e \times g_e \tag{4.32}$$

K_e is the element stiffness matrix and G_e is the geometric element stiffness matrix. As the first order theory, for an element with a semi-rigid connection, the stiffness matrices are corrected with a correction matrix which is stated in equation 4.31.

C_e is the element stiffness correction matrix and g_e is the geometric stiffness correction matrix given in Appendix B.4.

The material is considered to be nonlinear and the equations of equilibrium are developed on the deformed state of the elements. The analysis is performed to obtain the limit load considering the effect of axial force on the collumns. The results is displayed in Figure 4.40.

4.1.6.3 Free Vibrational Analysis

The free vibrational analysis is incoporated in the algorithm to determine the natrual period and natural modes of vibration of the structure using the eigen value and eigen vector problem. The equation of motion of a multi degree of freedom structure given in equation 4.33, where K is the structural stiffness matrix, C is the structural damping, M is the lumped mass matrix of the structure and *u(t)* is the displacement vector.

$$Ku(t) + Cu'(t) + Mu''(t) = 0 \tag{4.33}$$

If damping is assumed to be zero and the displacement assumes a harmonic motion for a single degree of freedom, ie. $u(t) = de^{-i\omega t}$, $Kd - \omega^2 dM = 0$ in equation 4.34 since an exponential function is never equal to zero.

$$(Kd - M\omega^2 d)e^{-i\omega t} = 0 \tag{4.34}$$

From equation 4.35, d is the eigen vector (mode shape) and ω is the eigen value (angular frequency).

$$KM^{-1}d = \omega^2 d \tag{4.35}$$

An built-in eigen sover in Matlab is used for this analysis which takes in the lateral stiffness matrix and the mass matrix as inputs and produces a matrix containing eigenvectors and and a vector of the corresponding eigenvalues.

4.1.6.4 Method of Analysis

A detailed explanation of the steps of the flow chart in Figure 4.34 for the generalized displacement based pushover analysis is given in this section. For the analysis to be under taken the following assumptions are taken into consideration:

- Members of every storey level has the same lateral displacement.
- Force-deformation relationship of the structural elements have strain hardening
- No out-of-plane loading and displacement
- Supports are restrained for rotation and translation in both x and y cordinates.
- Axial load has no effect on the force-deformation relationship of structural elements
- Deflection is due to bending only for first order theory and for second order theory of analysis both bending and axial load effect

The input data is an excel format which requires i) the nodal data which are the x and y coordinates of each node to compute the length and orientation of the each element, ii) element data which includes the left and right nodes of each element, the flexural, axial and shear rigidity, the positive and negative force-deformation relationship of each element, length of plactic hinges, the length of members with infinte rigid ends and axial loads in each column only for second order anaysis, iii) booundary condition which requires the nodes at the supports and the restraints and iv) mass data which are the lumped masses at each floor for free vibrational analysis.
The following detailed steps were used in the displacement based pushover analysis;

1. The target displacement is intialized as 0. To capture both the elastic behavior during the initial stages and plastic behavior of the member sections during loading before collapse, the incremental displacement, $\Delta\delta$ should be taken randomly small.

2. Element stiffness matrices are defined depending on whether first or second-order theory of analysis is to be considered. Each element stiffness matrix is corrected by the correction matrix given in the appendix based on the theory of analysis.

3. Global stiffness matrix is assembled according to the chosen global cordinate system.

4. The boundary conditions are applied to the Global structural stiffness matrix.

5. The lateral stiffness matrix is obtaiend through the condensed and reduced global stiffness matrix and the free vibrational analysis is performed to obtain the period of the structure.

6. With back substitution, the unknown nodal displacements are found and the corresponding internal forces in the local coordinate axis are obtained transforming the nodal displacement on an element level from global cordinates and multiplying with the assembled element stiffness matrix in the local axis.

7. During each displacement step before plasticity, the rotational stiffness is taken as infinity until it reaches the post elastic region where the slope is changed.

8. If any sections internal force, $M_i<M_u$, the curvature is taken as zero, if $M_i>M_u$ then the post elastic curvature is computed from the equation below.

$$\chi = M_i/EI \tag{4.36}$$

where EI is the preceeding rigidity of that section. Secant method is used to achieve convergence of the internal forces.

9. In turn, the χ value is used to obtain the inelastic flexural stiffness, $dM/d\chi$ of the section which is kept constant at the begining of a target displacement.

10. Two checks are conducted in this analysis; the ultimate moment capacity and the curvatures of critical sections. When a section reaches its ultimate moment, the rigidity of the section is computed from the moment curvature using the secant method. The rotational stiffness of the semi-rigid connections is the adjusted accordingly. The flexibility matrix is computed using the new rotational stiffness.

11. The displacement and corresponding lateral load is saved provided the moment has not exceeded the ultimate moment. A further increase in displacement, δ by incremental displacement, $\Delta\delta$ and a rerun of the analysis is performed using the newly obtained rotational stiffness.

12. Note: The internal forces, target displacements and base shear corresponding the last incremental parameter before a section reached the post elastic region is saved and the target displacement is reinitialized as zero and increased during the analysis. All internal forces and base shear obtained after a hinge occurance is superimposed with the last saved data including the target displacement.

13. This analysis ends when the ultimate rotational capacity of one section is exceeded or reached.

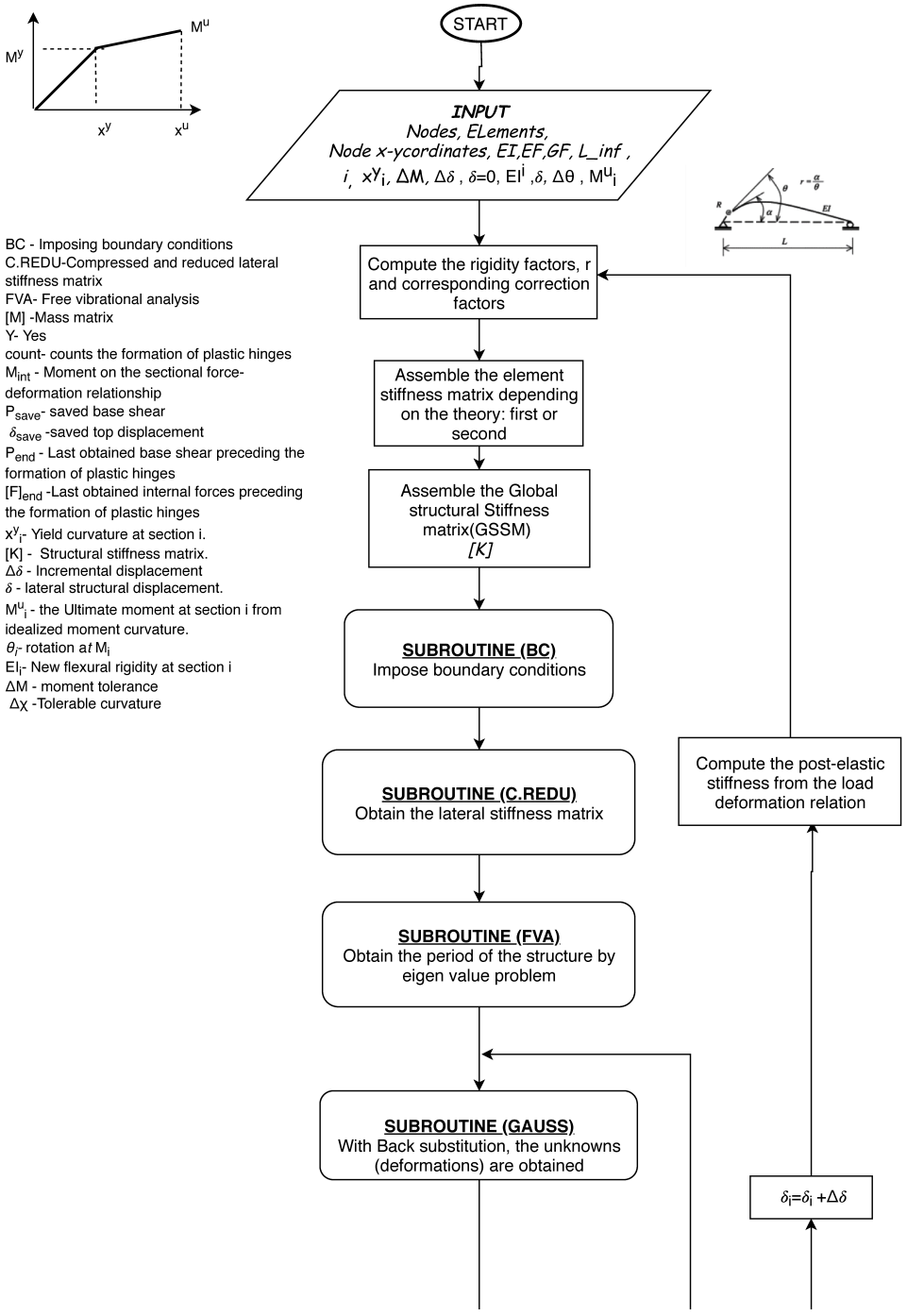

Figure 4.34: Flow chart of the lateral load increments with concentrated plasticity- 2nd technique

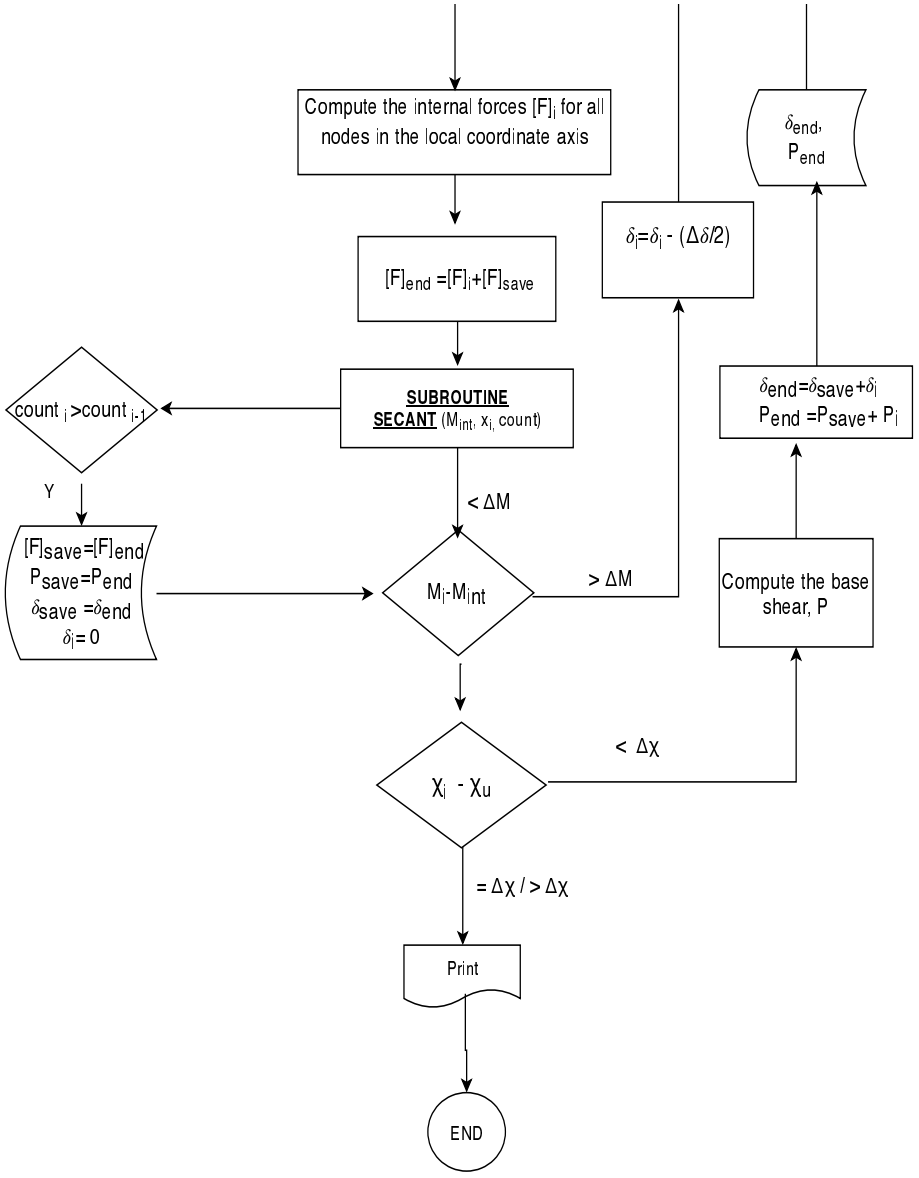

Figure 4.35: Continuation of the flow chart of the lateral load increments with concentrated plasticity- 2nd technique

4.1.6.5 Comparison of results of the analytical work with experimental results

Three cases were considered in the second technique namely; i) case 1 - all members of the frame structure were assumed to have uncracked rigidities; ii) case 2 - only the column was assumed to have a cracked rigidity and case 3- Uncracked rigidity on the columns with semi-rigid connections representing the cracked cracked sections. The results of the force displacement curves obtained for cases are shown in Figure 4.38. DC2B computer program, SAP2000 and hand calculations were used for the pushover analysis to validate the results obtained from this algorithm. DC2Bs' program for pushover analysis is force-controlled while the algorithm is displacement based, hence the differences observed will be discussed in this section. The idealized moment curvature relationship defined for the sections in DC2B is trilinear. Displacement controlled pushover analysis was performed in SAP2000 with all members having uncracked rigidity. The force deformation behaviour was defined by using the axial force and moment interaction diagram. Figure 4.36 shows the structural response for all analysis.

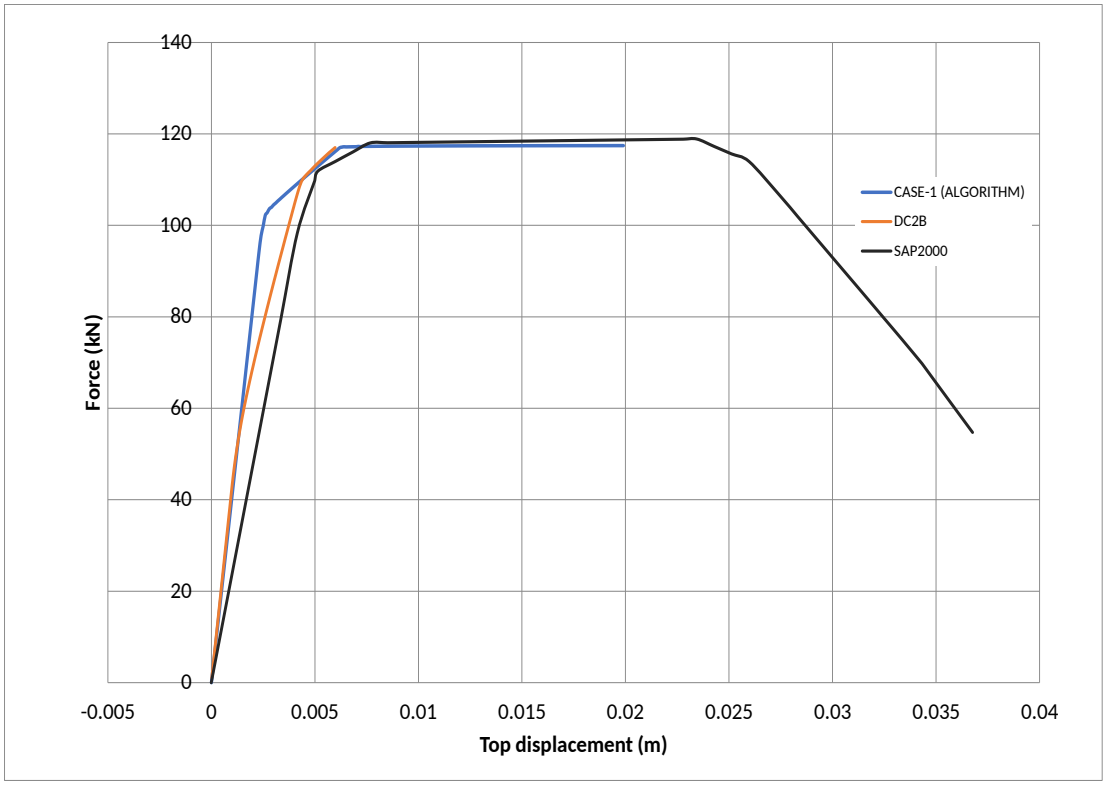

Figure 4.36: Comparison of the structural response of different computer programs

It is observed that the results obtained from algorithm is same as the results obtained from DC2B at the onset of the loading but the stiffness changed when cracking in the concrete begun hence making it deviate from the inital stiffness. The structural stiffness is highly dependent on the moment curvature relationship. The analysis in DC2B ended because the next step of incremented force was high and making a section reach its ultimate load earlier than was expected. This explains the difference between force-control and displacement control in lateral load increaments.

Comparing the results obtained by SAP2000 and the results of the algorithm, the initial stiffness of the algorithms results is higher than the result obtained by SAP2000. The only similarity observed is that the load carrying capacity of all programs are almost equal.

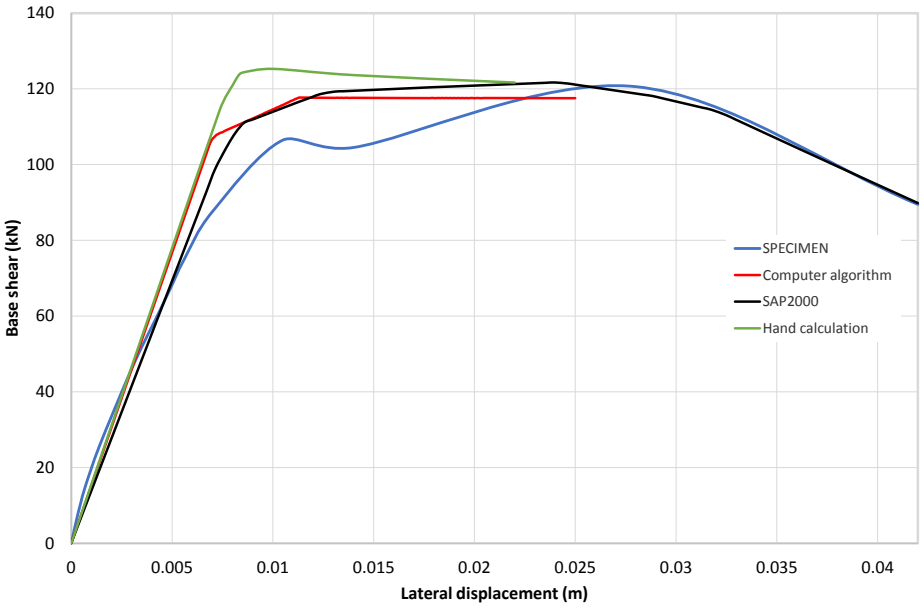

Figure 4.37: Comparison of the structural response with assigned effective rigidity

In Figure 4.37, the results in the graph are based on the an analysis performed by considering cracked rigidities. Based on the results obtained from the hand calculations in Figure 4.37, the lateral stiffness of the structure is the same with that of the algorithm.

For case 1(uncracked rigidity) and case 2, the initial stiffness is observed to be very high. Element sections seem to reach their inelastic state very quickly and the ultimate load is 117 kN which is the same as the other cases. As the rigidity of the column elements decreases, the yield and ultimate displacements increases hence increasing the ductility and decreasing the lateral stiffness of the structure which can be seen in the gradual descent in the slope considering the elements with semi-rigid connections in Figure 4.39. If the rotational stiffness, R of the semi-rigid ends are reduced to approximately zero, the stiffness of the structure

noticeably decreases with the formation of a plastic hinge. The structural stiffness affects the period inversely.

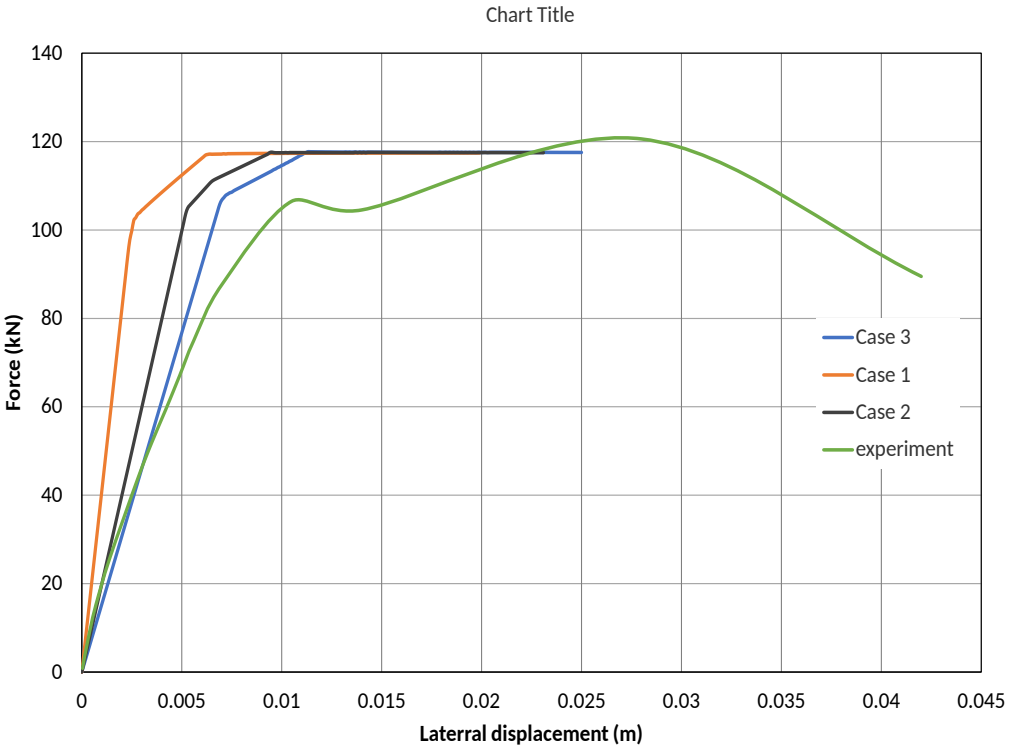

Figure 4.38: Force- displacement cuvre for concentrated plasticity- 2nd technique

From Figure 4.40 of case 3, the black marked points signify the formation of plastic hinges and the red points shows the achieved threshold of ultimate curvatures in the third case. Yielding occurs when the first plastic hinge was formed, in this case, at section 4 at a target displacement of 6.71 mm with a corresponding force, P =104 kN. The first section to exceed the ultimate curvature threshold was section 1 at a target displacement of 25 mm corresponding to a force of approximately 117 kN. With the second order effects on the element stiffness matrix and material nonlinearity considered, the limit loads after lateral load increment was carried out was found to be 110.8kN at a displacement of 25.4 mm. When compared with the results of the first order theory which is a limit load of 117.5 kN at a displacement of 25.3 mm, the second order effect reduces the loads at

each displacement.

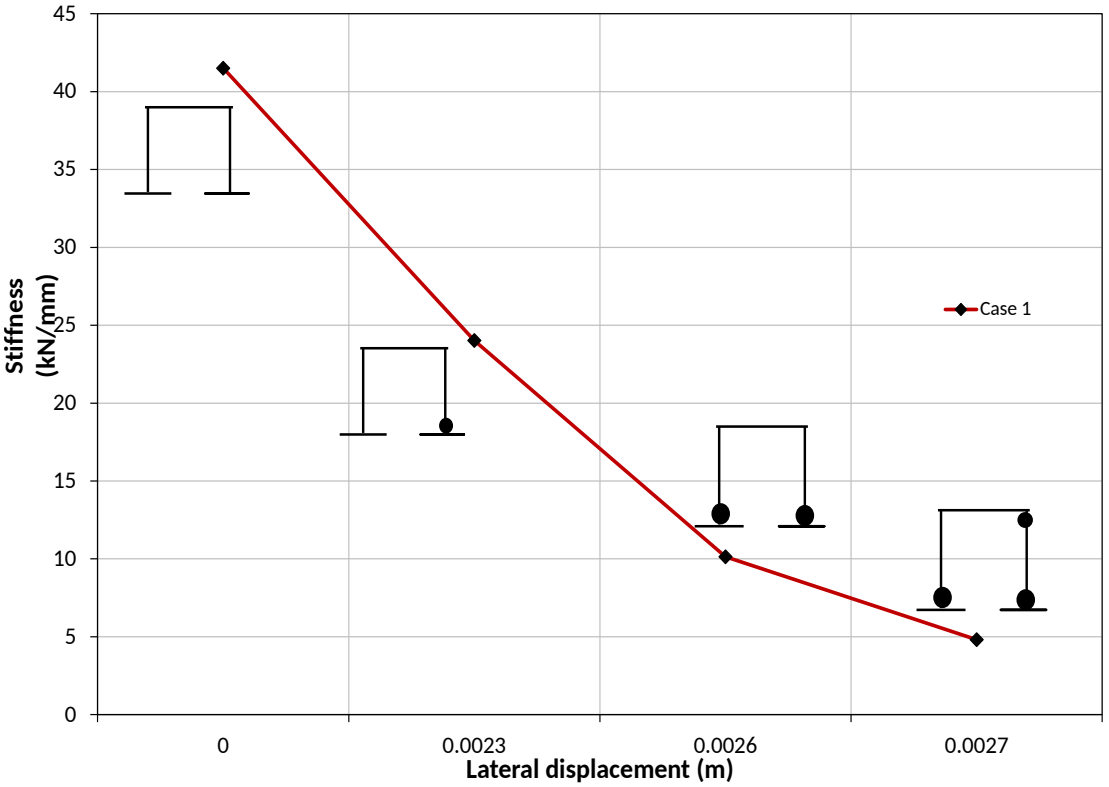

Figure 4.39: Lateral stiffness vs lateral displacement

At the early stages of the analysis, the loads are considered to be approximately equal because of the small displacements. The states of the sections after the formation of hinges is shown in Figure 4.45. The failure occured when the hinge at section 1 reached its ultimate rotation for both first order and second order theory analysis and the states of the other hinges are shown in 4.45 at hinge state 5.

Comparing the analytical results with experimental results, case 3 gives a better curve compared to case 1 and case 2. However the ultimate load is underestimated and the ultimate displacement is lower than the experimental results. The analytical results assumes the shape of the idealized force-deformation relationship.

Figure 4.47 is the compilation of the first order analysis of both techniques and

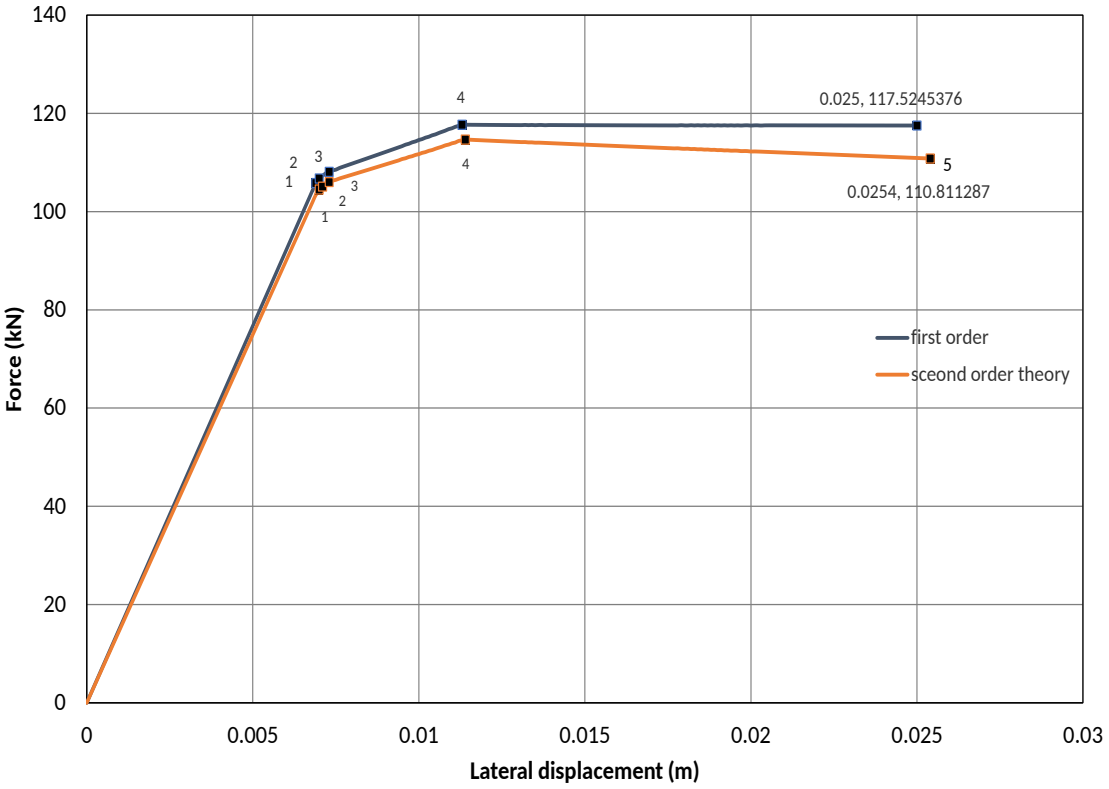

Figure 4.40: Lateral load increment with nonlinear materials -first order and second order theory

the experimental results. The results obtained from all techniques assumes the shape of the biliniearized moment curvature relationship considered above. The ultimate loads for all analysis can also be seen as the same. The analysis of the first technique cannot incoporate the plasticity since the hinge formation affects just the node, hence incoporating the change in the rigidity means changing the stiffness of the member. For both displacement and force control, there were no difference in the output. The rigidity of the elements has an effect on the structural behaviour as seen from Figure 4.47.

For the results obtained from the second technique where the length of the plastic hinge is taken as L_p, the difference when compared the experimental envelope curve is not large as compared to the first technique. the difference might be attributed to stiffness degradation during cyclic loading which is not incorporated in the algorithm.

4.1.6.6 Buckling Load Analysis

Buckling analysis determines the maximum compressive axial load that a structure can support before it collapses. Buckling can happen in two ways (local buckling and the global buckling) or both ways during the life cycle of the structure. Local buckling can reduce the load carrying capacity of a section due to reduction in the stiffness and strength in the post-elastic region of the force deformation relationship and global buckling is identified by the distortion of the axis of the member. When buckling occurs, a minimal increment in the axial load can result in a disastrous failure.

A closed form mathematical equation for critical buckling load for a column with pinned support in equation 4.37 was first developed by Euler but it could not be applied to framed structures due to the additional horizontal forces.

$$P_b = \pi^2 EI/L^2 \tag{4.37}$$

To minimize the effects of axial loads, codes suggest that the second order theory of analysis should be used in the determination of the buckling loads. Second order effects increases the deflection or displacement, δ which increases the internal forces (Moment). The second order analysis is also known as the P-δ analysis, where P refers to a gravity load and δ refers to a displacement. Second order effect could occur as combined effect of axial load and bending or it could occur due to the effect of just the axial loads. In this section, the second order effect of the combined effect will be the focus of this study.

An algorithm is developed to perform a buckling analysis to obtain the buckling load parameter of the frame. The second order stiffness parameters discussed above will be used in this analysis. In the attempt to obtain the buckling load, two techniques were considered. The first was to assign a small force, 0.01 P as lateral load where P is the buckling load parameter. The second technique is the determinant criteria, where the determinant of the coefficient structural stiffness matrix is found for every load increment until the determinant is zero

provided there are no external loads. Figure 4.42 shows the flow chart for the first technique and Figure 4.41 gives the flowchart for the determinant criteria technique. Case 1 of section 4.1.6.5 is used in the buckling analysis to discuss the effect plastic hinge formation on buckling safety factor.

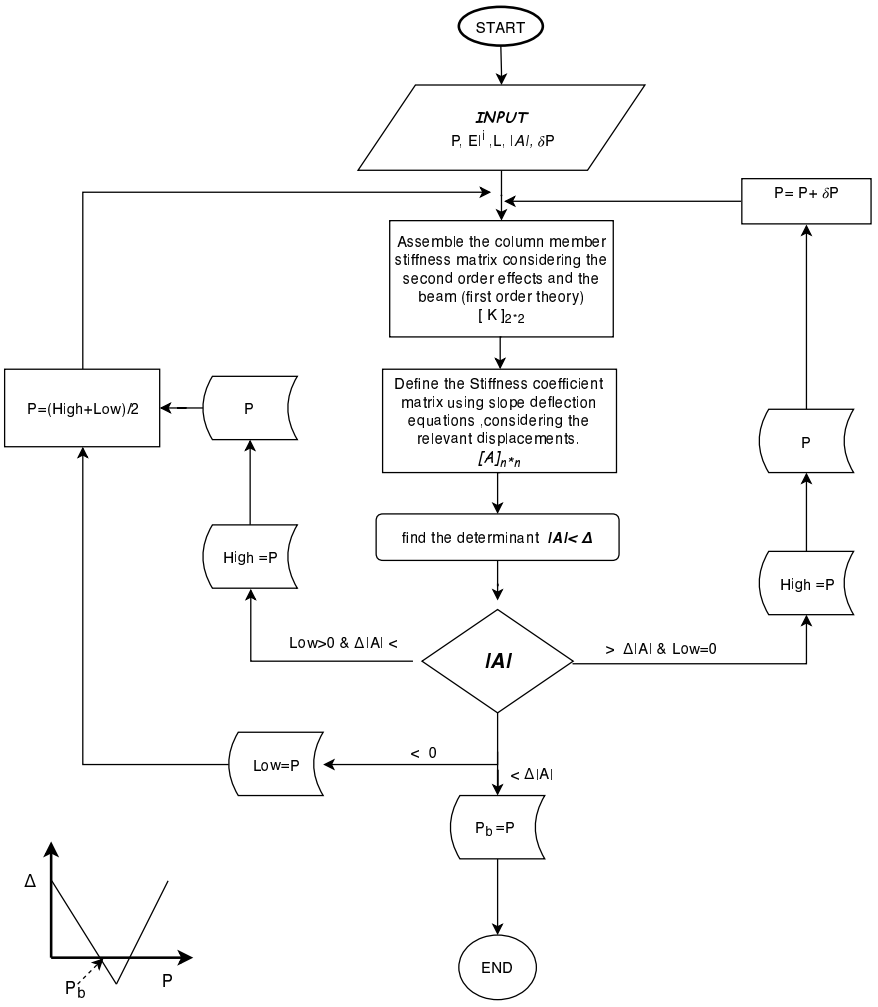

[A]$_{n*n}$ - Structural stiffness matrix.
Δ - determinant of the structural coefficient matrix
δP - Incremental force
EI$_i$- rigidity of members
L - Length of members
P- Axial force in columns
Δ|A| -Tolerance of the determinant of the structural coefficient matrix
P$_b$ - Buckling load
High - force when Δ >0
Low - force when Δ <0

Figure 4.41: Flow chart for buckling load -determinant criteria

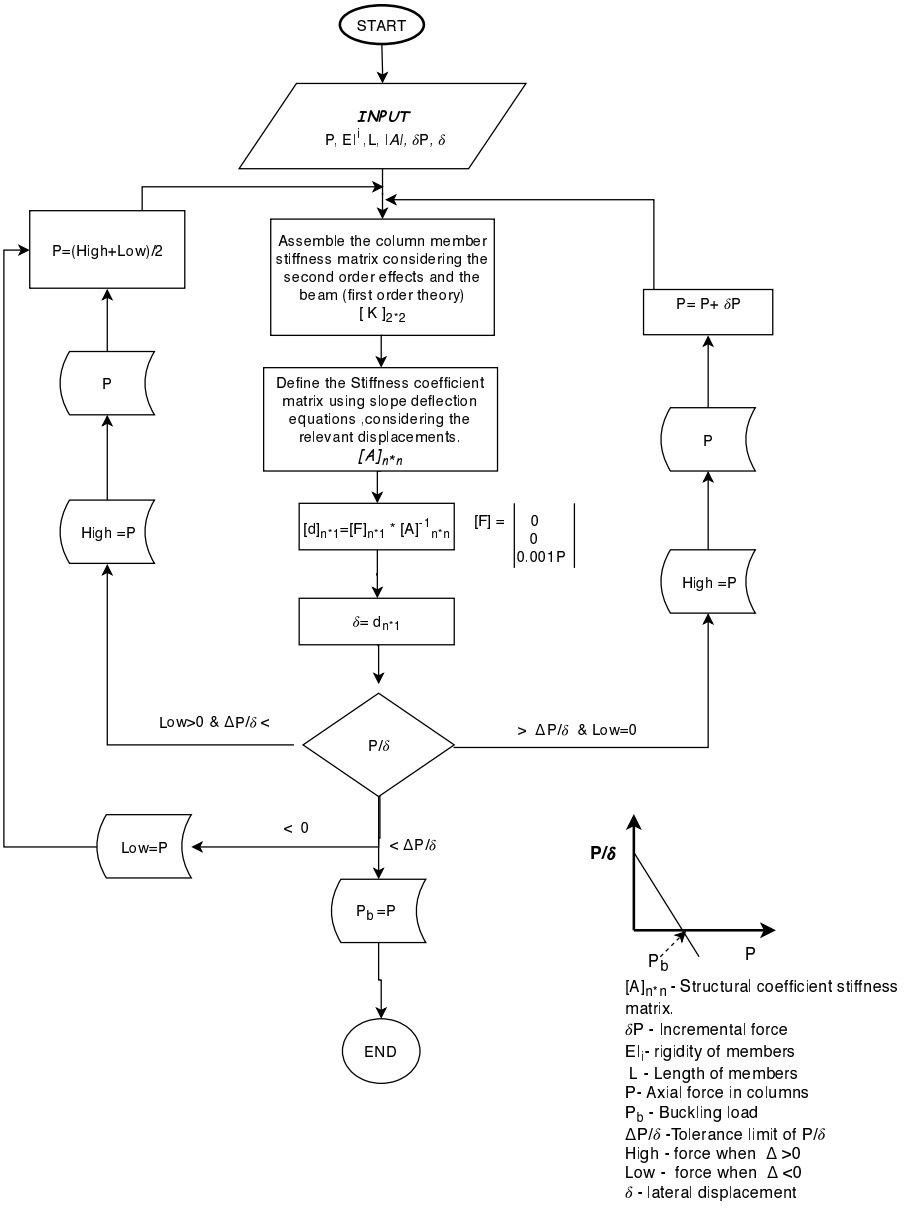

Figure 4.42: Flow chart for buckling load -displacement criteria

Considering the first technique, the buckling load or the stabiliity load is determined from an asymptote of the resulting P-δ curve or another approach is to obtain the P-intercept (in other words, the point where P/δ =0) on the P/δ vs P

graph as obtained in Figure 4.43. The stability load or P_b for case 3 is obtained as 24682kN with a buckling length of 1.511 m greater than the length of the column (1.3623 m). Hence, the safety against buckling, P_b /P is 137.122. When considering the determinant criteria technique the buckling load, P_b is obtained as 24079kN. The results obtained for P-δ is slightly higher than the results obtained from determinant criteria. To verify the validity of this results, one condition was checked by assuming the rigidity of the beam to be very small (0.001EI). This condition then make the columns of the frame act like a cantiliever with a buckling length of 2L. The buckling load obtained through the P-δ and the determinant criteria algorithm were 7618 kN and 7580 kN respectively while through the theoritcal euler critical buckling load formula ($P_b = \pi^2 EI/(2L^2)$), the buckling load was obtained to be 7591.5 kN. This is difference is considered acceptable because of the presence of the beam.

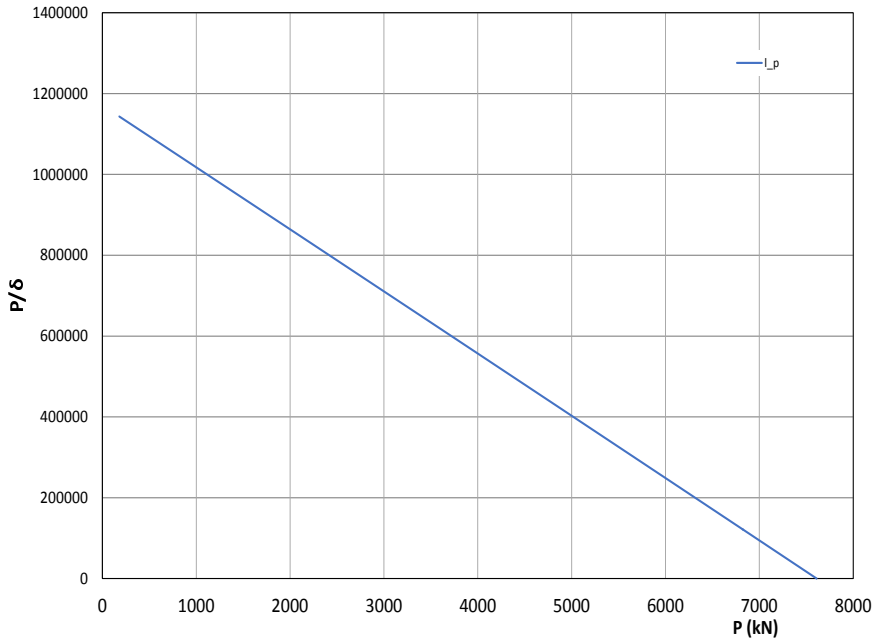

Figure 4.43: Second order analysis: P/δ vs P

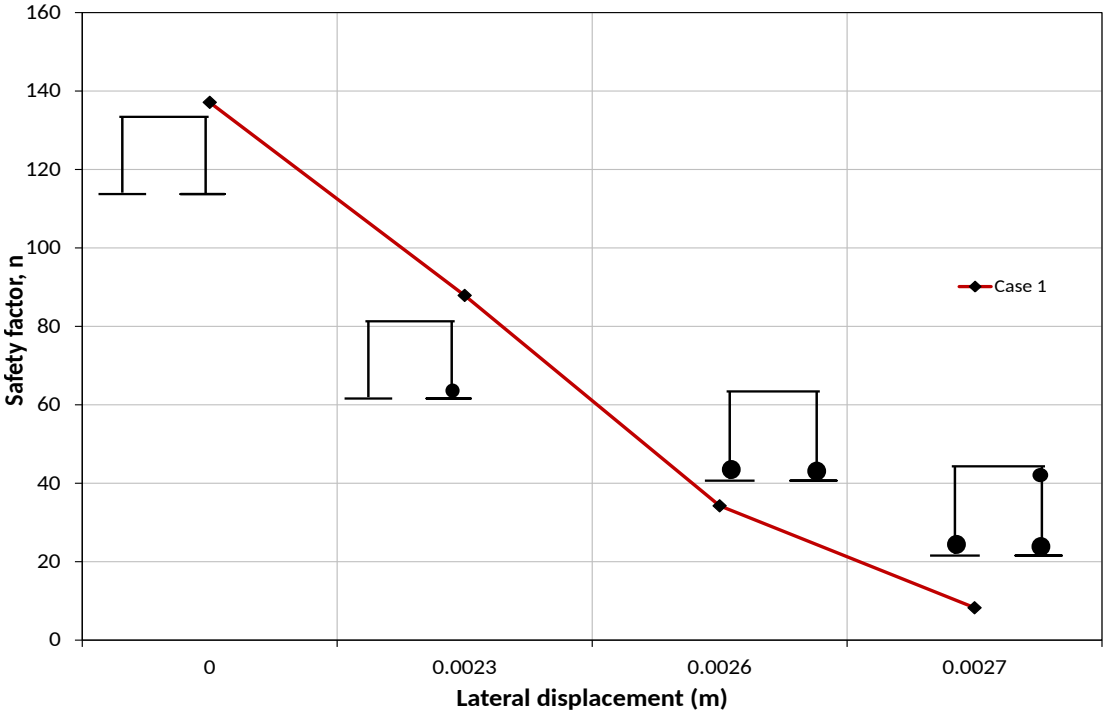

Figure 4.44: Stability loads at every hinge formation stage

During the material nonlinearity analysis, with the occurance of plastic hinges, the change of rigidity of semi-rigid springs at sections with accumulated plastic deformation, the buckling loads are recalculated after a new hinge formation because of the possibility of loss in the safety margin against local buckling or global buckling. Considering the graph shown in Figure 4.44 for case 1 which shows the hinge states and the safety buckling factors and Figure 4.45 which shows the hinge formations and the stability loads for case 3, it is agreeable that the hinge formation at sections affects the buckling load parameter. For the third hinge formation in case 3, the safety factor drops down as much as approximately 94% of the buckling saftety factor at the elastic state.

Hinge state	Critical Sections				first order theory		second order effect	
	1	2	3	4	P_b	n	P_b	n
0.01P P δ 1	$M_1 < M_u$	$M_2 < M_u$	$M_3 < M_u$	$M_4 = M_u$	5600.20	31	5587	31
0.01P P δ 2	$M_1 < M_u$	$M_2 < M_u$	$M_3 = M_u$	$M_4 = M_u$	5578.50	30.99	5553.90	30.86
0.01P P δ 3	$M_1 < M_u$	$M_2 = M_u$	$M_3 = M_u$	$M_4 = M_u$	5507.00	30.59	5480.50	30.48
0.01P P δ 4	$M1 = M_u$	$M2 = M_u$	$M_3 = M_u$	$M_4 = M_u$	4207.90	23.38	4182.80	23.24
0.01P P δ 5					2139.60	11.89	2143.50	11.90

Figure 4.45: Stability loads at every hinge formation stage

4.2 Parametric Studies on Pushover analysis

4.2.1 Effect of Plastic Hinge Formation on the Period of the Structure

When a structure is excited by seismic forces, it starts to vibrate. The lowest natural frequency of vibration of a structure corresponds to the longest time period (T) of vibration, as frequency and time period are inversely propotional to the frequency. The period of the structure is obtained from the first mode shape of the strucutre. In this section, the effect of the plastic hinge formation in structures on the period of structures during nonlinear pushover analysis is discussed.

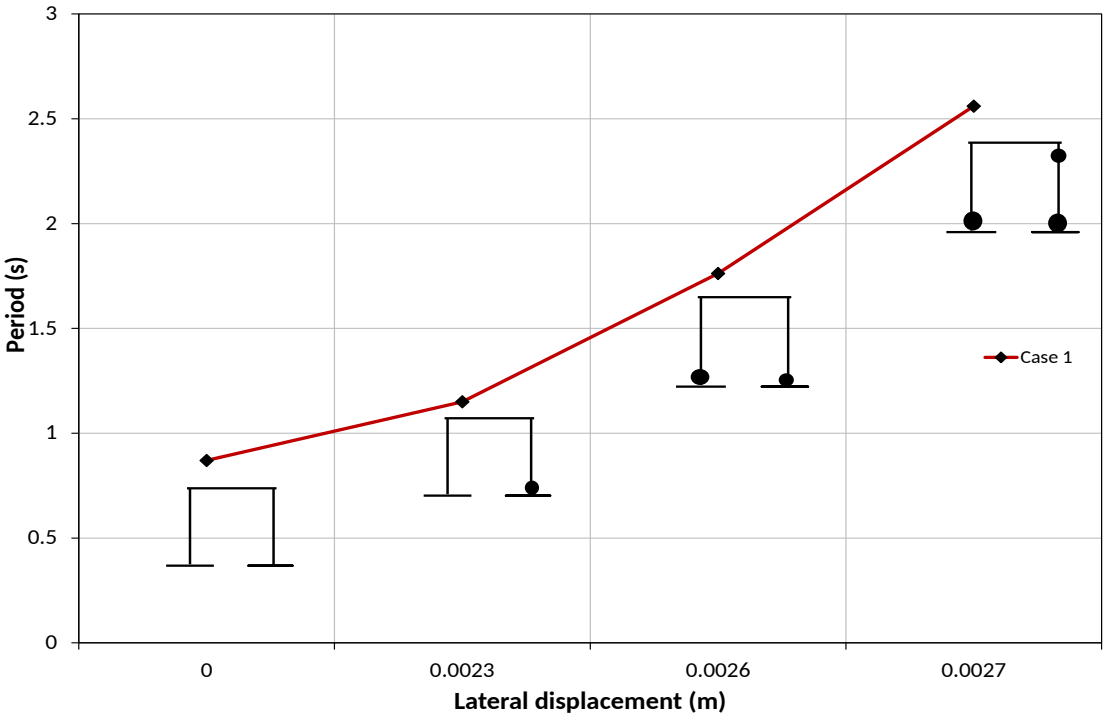

Figure 4.46: Periods at plastic hinge formation

From Figure 4.46, period of the structure increases rapidly as plastic hinges form. As metioned earlier, period is the inverse of frequency, hence the higher the period, the lower the frequency. From the elastic state to the first, second and third occurance of the plastic hinge, the period increases while the frequency decreases

by 67%, 102% and 194% respectively. During an earthquake, the closer the frequency of an earthquake is to the natural frequency of a building, the more energy is introduced into the building structure causing severe damages to structures. From TSC [24], the design spectrum shows that at high seismic accelerations, structures have short periods, hence attracting highers seismic forces. As the period increases, it attracts smaller seismic forces.

4.2.2 Effect of Length of Plastic Hinge

A parametric work is done on the length of the plastic hinge assigned to the semi-rigid connection to determine the effect it has on the pushover curve. The length of the plastic hinge is computed from the formula given in equation 4.5. The parameters considered were half the plastic hinge length and full computed plastic hinge length. The results of this analysis is shown in Figure 4.47.

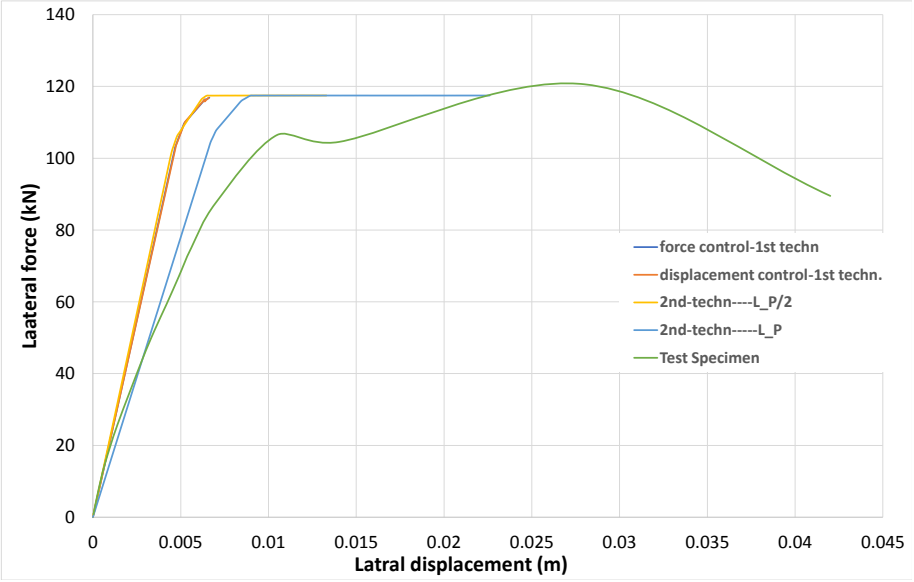

Figure 4.47: Results of theoritical work on lateral load increments (First order theory)

As the length of the plastic hinge decreases, the intial stiffness of the structure increase. From the parametric work on the period, it is understandable that the

higher the structural stiffness, the lower the period with a high natural frequency. The displacement ductility decreases with a decrease in the length of plastic hinge region. The formation of plastic hinge occur at lower target displacements when the length of the plastic hinge region is decreased but the load carrying capacity of all plastic hinge length were the same.

4.2.3 Effect of Flexural Rigidity

Flexural rigidity of a structure determines the ability of all members to resist bending. The effect of the flexural rigidity of the frame is studied in two categories. Under category I, the beams are assigned uncracked rigidities and columns have altered rigidities at the plastic hinge length while in category II, both beam and columns are assigned cracked rigidities as specified by TSC [24]. According to TSC [24], for RC columns, the range of the cracked sectional rigidity is between 0.4EI and 0.8EI which depends solely on the intensity of the axial load on the column and for beams, 40%EI is stated. Table 4.2 below outlines the intensity of the rigidity for each member in all the analyses performed. For F_I-1, the subscript represents the category and the number represents the column rigidity factor

Figure 4.48 shows the force displacement relationship of the two categories and

	Analysis	**Flexural Rigidity modifier(EI)**	
		Beam	Column
Category I	F_I-1	1.0	1.0
	F_I -2	1.0	0.8
	F_I -3	1.0	0.6
	F_I -4	1.0	0.4
Category II	F_{II}-1	0.4	1.0
	F_{II}-2	0.4	0.8
	F_{II}-3	0.4	0.6
	F_{II}-4	0.4	0.4

Table 4.2: Factors considered in parametric work of flexural rigidity

the results are summarized in Table 4.3. Yield displacement, δ_y is defined as the

displacement at the first occurrence of a plastic hinge,δ_u is defined as the ultimate displacement when two or more hinges reach their ultimate rotational capability to cause a mechanism or failure. F_y and F_u are the corresponding forces at the yield and ultimate displacements respectively. μ is the displacement ductility ratio of ultimate displacement to yield displacement.

	Analysis	Δ_y(mm)	F_y(kN)	Δ_u(mm)	F_u(kN)	μ	ratio
Category I	F_I-1	4.149	106.143	25.453	122.576	6.134	1
	F_I-2	4.950	106.42	26.323	122.569	5.318	0.867
	F_I-3	6.2896	106.865	27.704	122.566	4.405	0.718
	F_I-4	8.977	107.581	31.10	122.587	3.464	0.565
Category II	F_{II}-1	4.4675	102.983	25.304	122.369	5.664	1
	F_{II}-2	5.248	104.312	26.106	122.168	4.974	0.878
	F_{II}-3	6.587	104.983	28.4248	122.535	4.315	0.762
	F_{II}-4	9.24	105.607	30.628	122.444	3.315	0.585

Table 4.3: Results of parametric work on flexural rigidity

For category I, the result shows an increase in yield displacement as the effective flexural rigidity decreases. The percentage increase of the yield displacement in F_I-2, F_I-3, F_I-4 compared to F_I-1 are 19.3% ,51.6% and 116.43% respectively, and percentage increase in the ultimate displacement with respect to F_I-1 is 3.4%, 8.8% and 22% respectively . Figure 4.48(c) reveals that displacement ductility, μ decreases as the rigidity reduction factor decreases because of the rate of increase in the yield displacement is higher compared to the ultimate displacement. The yield force, F_y and ultimate force, F_u is almost constant for all analysis.

In category II, the result displays an increase in yield displacement and a decrease in ductility ratio. The percentage increase of the yield displacement in F_{II}-1, F_{II}-2, F_{II}-3, F_{II}-4 compared to F_I-1 are 7.7% , 26.49%, 58.76%and 122.7% respectively. In F_{II}-4 analysis, the yield displacement becomes more than 2 times the yield displacement of the unaltered rigidity analysis(F_I-1).

Comparing category I and II; when the cracked rigidity of the beam was imposed, the effect on the yield and ultimate displacement was huge. One reason could be that the beams were stronger than the columns. Considering analyses with constant column effective rigidity but different beam rigidity;F_I-1 and

F_{II}-1, F_I-2 and F_{II}-2, F_I-3 and F_{II}-3 and F_I-4 and F_{II}-4, there was a decrease in yield force by 3%, 2%, 1.76% and 1.8%. This concludes that, for structures with strong beams, it is almost insignificant to impose cracked rigidities during nonlinear analysis. In seismic analysis, ductility is known to affect the response modification factors. Load reduction factors are used to scale down the elastic response to the desired ductility demand of a structure. Aside from ductility being a factor, period and overstrength factor plays a major role. Overstrength factor

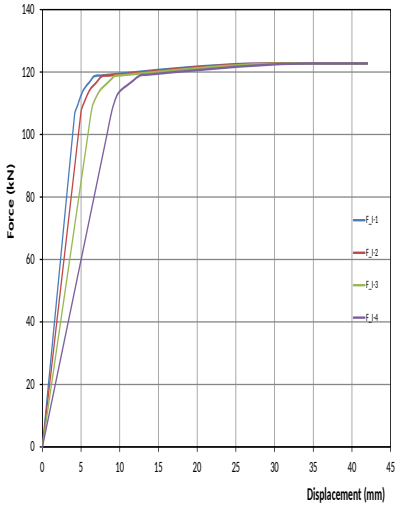

(a) Category I

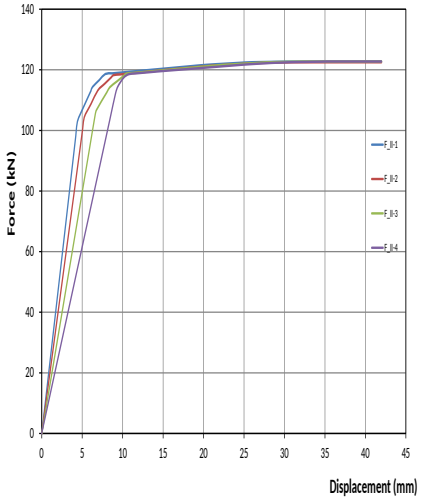

(b) Category II

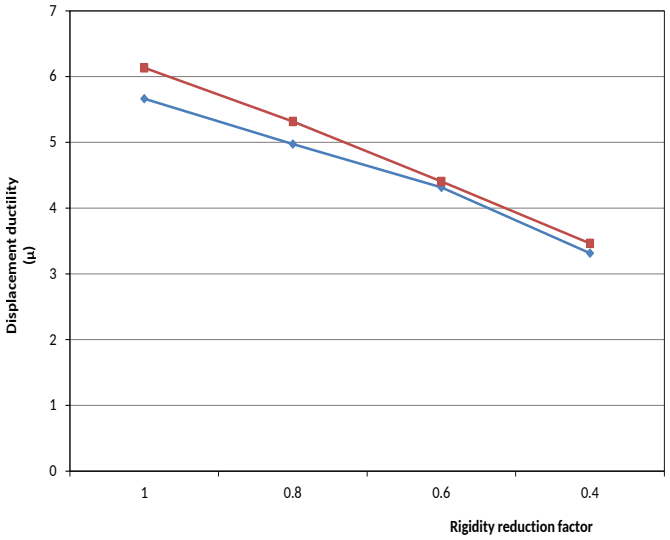

(c) Displacement ductility of category II

Figure 4.48: Force-displacement graph

is the residual strength from the first hinge formation to the structural yield. Over strength factor is affected by factors like strain hardening, the amount and position of flexural reinforcements and storey drift (chia-ming uang).

To conclude, decrease in flexural rigidity increases the yielding displacement which decreases the ductility demand, although the ultimate displacement is increases. Since the ductility is a factor of the response modification factors (force reduction factors and displacement amplification factors), the selection of the flexural rigidity reduction factor affects the modification factors. The smaller the flexural rigidity reduction factor, the smaller the ductility, hence the smaller response modification factors.

4.2.4 Effect of Sectional Ductility

To determine the extent of the effect of sectional ductility on the structural performance (ductility) under incremental loads in nonlinear analysis, the material properties of first section to reach its ultimate deformation threshold is changed. The material properties taken into consideration is concrete quality, reinforcement quality and quantity.

There are several methods which can be used in improving the sectional strength and ductility of columns which includes jacketing, retrofitting and using carbon fiber reinforced polymer for wrapping. In this study, as mentioned above, the sectional ductility will be improved by altering the material properties. This method is quite unfeasible on the field but theoretically it is altered to study the effect it has on the overall structural ductility.

This parametric work is performed by the help of the computer programs SAP2000 and Xtract. Xtract software was used to obtain the moment curvature after changing the material properties and SAP2000 was used in the pushover nonlinear analysis.

Tables 4.4, 4.5 & 4.6 shows the stages at which the materials properties were changed and the specific section which had reached the ultimate curvature. Stage 1 is the reference stage where all the section are have a lower deformation state

compared to their ultimate deformational capacity. During the analysis, section 1 in Figure 4.26 was first to reach its ultimate curvature so the material property of section 1 was changed, specifically concrete quality of section 1 was increased from 20.17 MPa to 30 MPa which increased in sectional ductility as shown in Table 4.4 at stage 2. The analysis was performed again and subsequent checks and material alteration were performed which is evident in the change in ductility in Table 4.4.

In Tables 4.5 & 4.5, the same procedure was used but the concrete quality remained the same as the reference stage (stage 1) but the reinforcement quality was change to S420 and the quantity was changed respectively. From Figure

Stages	**Sectional Ductility**				η
	section 1	section 2	section 3	section 4	
1	3.75	6.46	5.24	5.24	3.324
2	5.714	6.46	5.24	5.24	3.879
3	5.714	6.46	7.159	5.24	4.109
4	5.714	6.46	7.159	7.159	4.484

Table 4.4: Effect of sectional ductility by altering concrete quality

Stages	**Sectional Ductility**				η
	section 1	section 2	section 3	section 4	
1	3.75	6.46	5.24	5.24	3.324
2	2.362	6.46	5.24	5.24	3.232

Table 4.5: Effect of sectional ductility by altering reinforcement quality

Stages	**Sectional Ductility**				η
	section 1	section 2	section 3	section 4	
1	3.75	6.46	5.24	5.24	3.324
2	4.986	6.46	5.24	5.24	3.836
3	4.986	6.46	7.87	5.24	4.175
4	4.986	6.46	7.87	7.87	4.219

Table 4.6: Effect of sectional ductility by altering reinforcement quantity

4.49 and Table 4.4, an increase in concrete quality increases the sectional ductility and structural ductility. The results obtained in Figure 4.49 and Table 4.6 helps to draw a conclusion that an increase in reinforcement quantity also increases

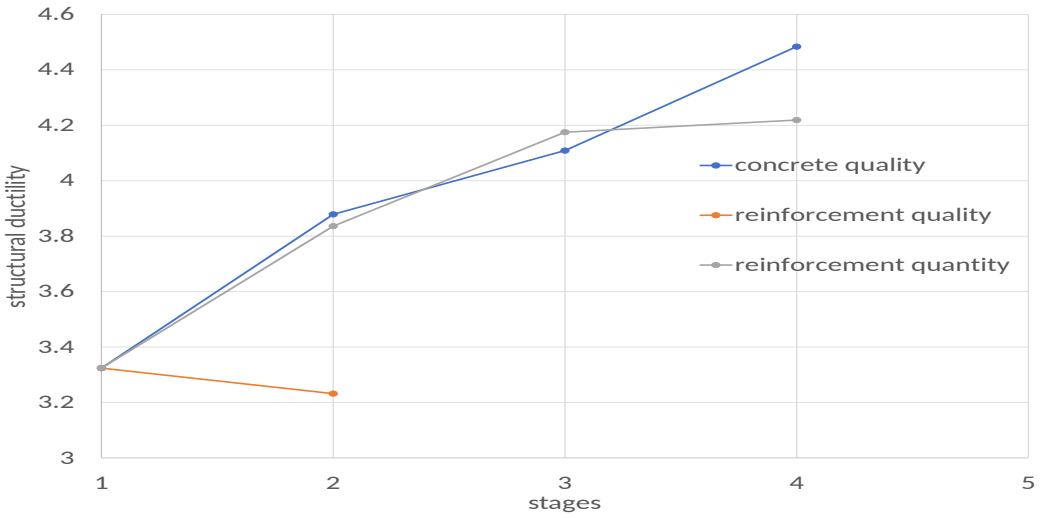

Figure 4.49: Effect of section ductility on structural ductility

the structural ductility. To be specific, an increase in compression reinforcement increases the sectional ductility and structural ductility. Considering the reinforcement quality graph in Figure 4.49 and Table 4.5, the opposite can be said about an increase in reinforcement quality. The higher the strength of the reinforcement, the higher the moment capacity of the section but the more brittle the section becomes, hence the lower the sectional ductility which eventually decreases the structural ductility.

To conclude, increasing the sectional ductility of a section increases the structural displacement ductility and vice versa. To obtain a high target displacement ductility of a structure, an increase in the concrete quality and the quantity of compression reinforcement should be taken into consideration because it influences the sectional ductility hence increasing the structural ductility.

4.3 Application of the Adapted Algorithm to a Representative Frame

To determine the extent of the developed algorithm for pushover analysis, in this section, it is applied to a 2D frame of an unsymmetrical building presented in Figure4.50. It is a 3 storey 3 bay structure with a height of 9 m. Inter-storey

height is 3 m for all storey levels. The distance between two successive columns is not equal and the structural members include beams, columns and shear walls.

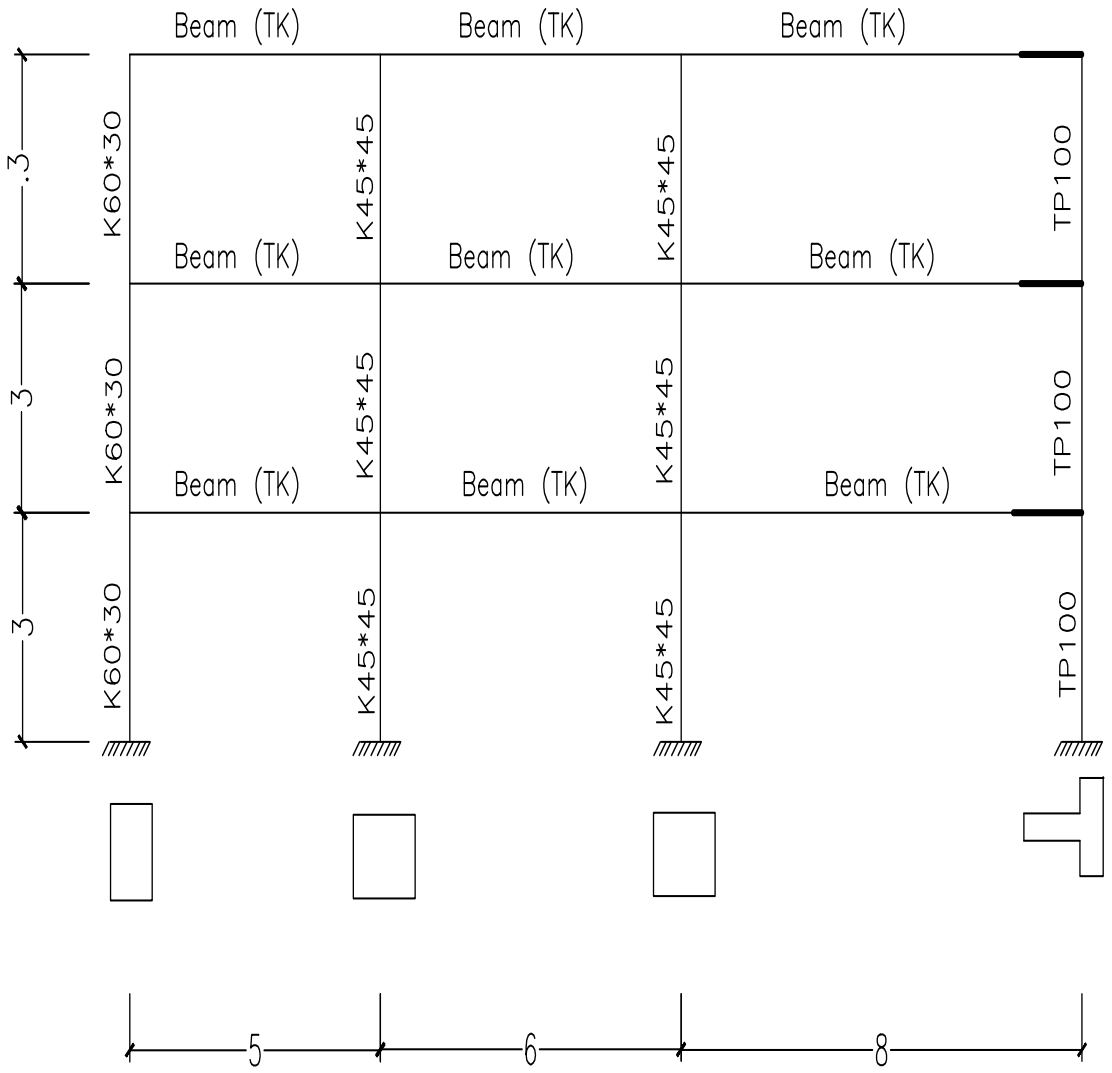

Figure 4.50: Representative Frame

The structural members have different cross-sections and reinforcement detailing which are detailed in Figure 4.51. The shear walls are located at the external columns on the right end of the representative frame which spans into the beam creating a rigid zone. The concrete cover is 30mm for all members and the material strength used in this analysis were C20 for concrete and S420 for the reinforcements. The beams cross-sections and mechanical behaviour are the

same on all storey floors and the external columns have different cross-section compared to the interior columns.

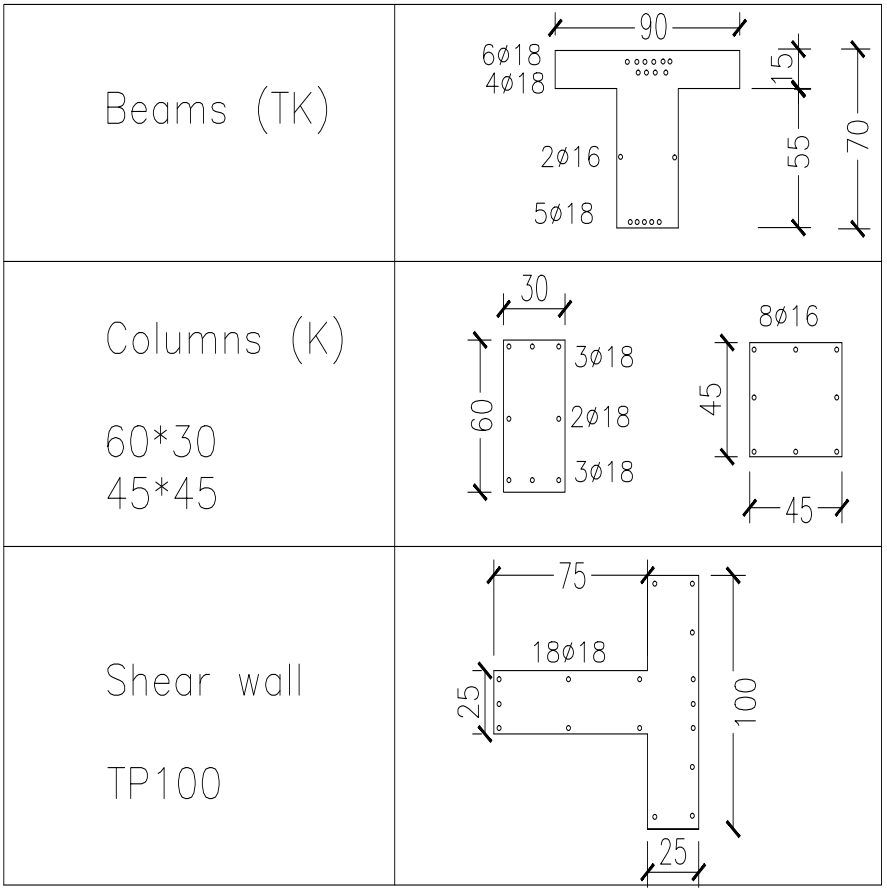

Figure 4.51: Cross-sections of members in the representative frame

The moment curvature relationship for all sections are presented in the Table 4.8. The column moment curvature is obtained by taking into consideration the compressive axial force in each column and the zero axial force is considered for the force deformation on the beams. Both the positive and negative deformation capacities are detailed in the table. Since columns have a symmetric arrangement of reinforcements across the cross-section, the positive force deformation characteristics are same in the negative moment direction.

The stiffness parameters of beams with infinitely rigid end and shear walls are incorporated into the computer program.

Sections	Axial Force	yield		Ultimate	
		Curvature	Moment	Curvature	Moment
	[kN]	[1/m]	[kNm]	[1/m]	[kNm]
Beams	0	0.004	400	0.1182	410
60×30	400	0.014	148	0.08889	150
	250	0.01394	133	0.1177	136
45×45	1200	0.010	290	0.0312	300
	1000	0.0099	275	0.0344	293
	720	0.0099	255	0.0437	271
	550	0.0080	245	0.0533	251
100×100	750	0.004	770	0.0774	831
	580	0.0035	730	0.0827	795
	410	0.004	710	0.0888	741

Table 4.7: Positive Momnet curvature relationships of members of representative frame

Sections	Axial Force	yield		Ultimate	
		Curvature	Moment	Curvature	Moment
	[kN]	[1/m]	[kNm]	[1/m]	[kNm]
Beams	0	-0.006	-658	-0.04	-660
100×100	750	-0.045	-1227	-0.0147	-1271
	580	-0.004	-1171	-0.0159	-1222
	410	-0.0045	-1123	-0.0174	-1166

Table 4.8: Negative moment curvature relationships of members of representative frame

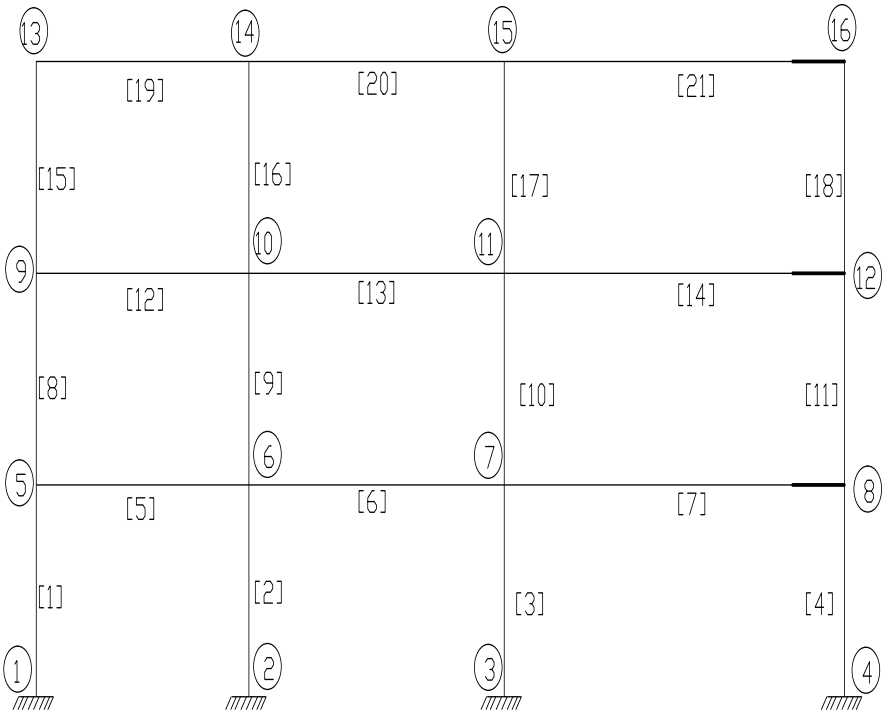

Figure 4.52: Nodes and members considered in the representative frame

Two analyses were conducted; first order theory of analysis and second order theory of analysis. In the first order theory,the effect of axial forces is not taken into consideration. With the second order theory of analysis, the axial force on each column was taken from the static load analysis of the external forces conducted in DC2B. Based on the algorithm developed for pushover analysis in this thesis, the program terminates after any section reaches its ultimate force and deformation capacity. The identified node and member numbers in Figure 4.52 are used in the pushover analysis. To validate the results of the algorithm, the global structural stiffness matrix and the structural reponses under 1 kN lateral force from an analysis by DC2B is compared with the results by the algorithm. The global stiffness matrix were found to be equal for both the algorithm and DC2B. The comparison if the internal forces of analytical results for 1 kN lateral force is given in Figure 4.53.

Although the global stiffness matrices were the same, a slight difference was observed in the comparison of the internal forces by DC2B and the algorithm (Figure 4.53). This is attributed to one assumption considered in the algorithm which states that all structural elements of each floor have equal lateral displacements. The base shear and the coressponding top displacement for the first order and second order theory of the pushover analysis is shown in Figure 4.54 and the tabulated results in Figure 4.56 presents the initiation of plastic hinges in elements (members) of the frame and their respective top displacement. The results of this analysis is independent of the external forces.

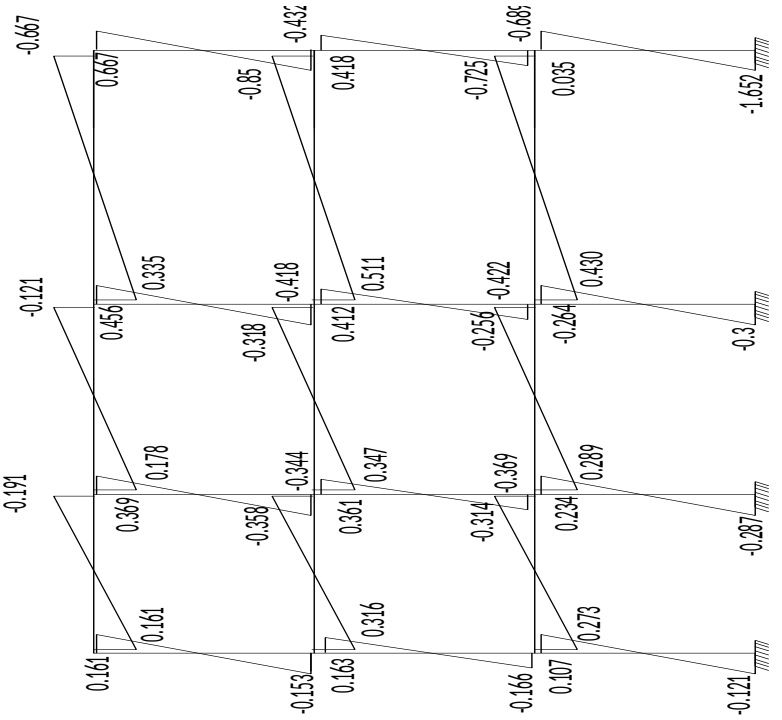

(a) DC2B

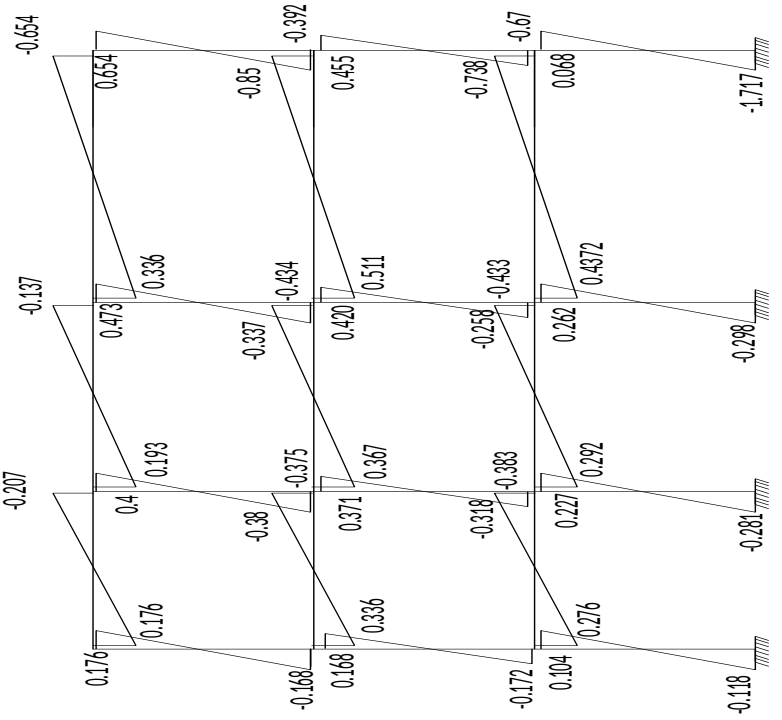

(b) Algorithm

Figure 4.53: Comparison of Internal forces

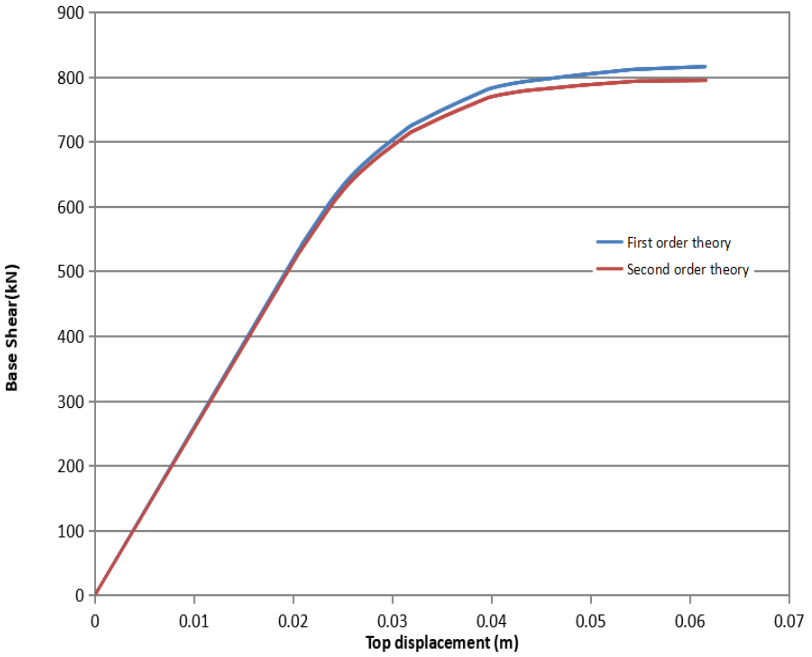

Figure 4.54: Structural response of the representative frame

The first structural limit load carrying capacity corresponding to the first order theory of analysis was obtained as 815.7kN at an ultimate displacement of 61mm and the second limit load of the second order theory of analysis with material nonlinearity is 794kN at an ultimate displacement of 61mm. This explains the effect of axial loads on the load carry capacity of structures. The first section to reach its ultimate moment and deformation capacity was the bottom section of the shear wall.

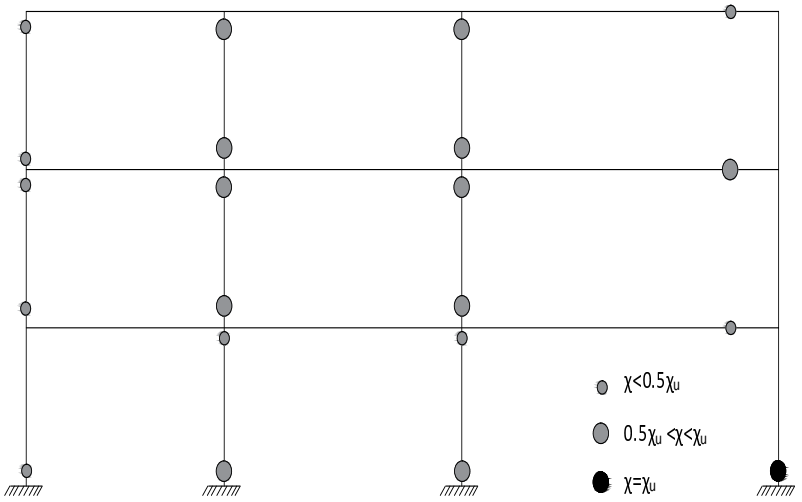

Figure 4.55: Plastic hinge formation in the representative frame

The hinge states in terms of their deformation at failure are shown in Figure 4.55 for first order analysis. The first section to excced its elastic state was in element 17 at a displacment of 20 mm and the last hinge to form was at the base column at a top displacement of 54 mm. The beams in the first and second bay of the representative frame remained in their elastic state but the sections of beams with infinte end in the last span of the frame were in the post-elastic region of their respective force deformation characteristics.

Structural element	Node	Displacement (m)
17	15	0.02045
17	11	0.02338
16	14	0.02398
10	7	0.02511
10	11	0.02561
16	10	0.02624
9	6	0.02675
9	10	0.02810
15	13	0.02876
15	9	0.03093
4	4	0.03164
14	12	0.03195
8	5	0.03508
8	9	0.03687
21	16	0.03973
7	8	0.04081
3	3	0.04222
2	2	0.04310
3	7	0.04885
2	6	0.05385
1	1	0.05442

Figure 4.56: Intiation stage of Plastic hinges in the representative frame

4.4 Expansion ratio of the descending branch of 15 year old concrete specimen

The cylindrical specimens were tested to obtain the stress-strain curves. The lateral deformation and longitudinal deformation were obtained simultaneously during the experiment to determine the poison ratio. Poisson's ratio, ν describes the extent of expansion in materials and it is defined as the ratio between the lateral strain, ε_L and the longitudinal or axial strain, ε_A as shown in equation 4.38.

$$\nu = -\frac{\varepsilon_L}{\varepsilon_A} \tag{4.38}$$

The stress- strain curves obtained after the experimental test is shown in Figure 4.57.The stress is computed from the ratio of force over the surface area (πr^2), the longitudinal or axial strain is obtained from the average of the recorded axial deformation divided by 1/2 the height and the lateral strain is the average of

the recorded lateral deformation divided by the radius. The measure ment of the lateral expansion after spalling was excluded since there was difficulty in obtaining correct lateral displacement of the transducers. The spalling strain is defined as 0.005 axial strain as defined in codes.

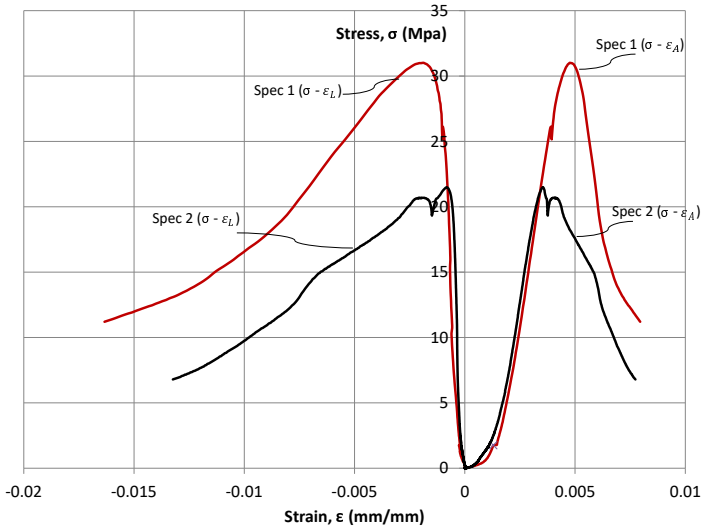

Figure 4.57: Stress strain curves of 15 year old concrete cylinder specimens under uniaxial compression

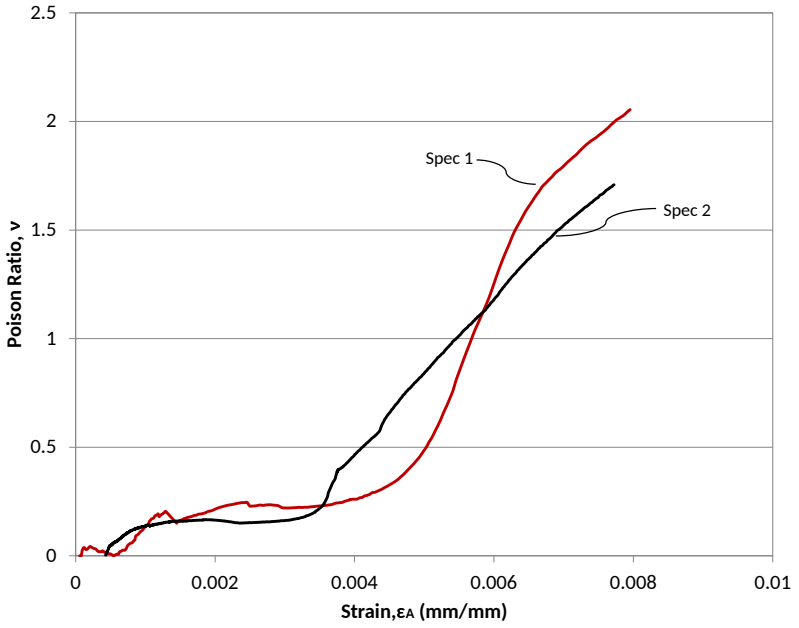

Figure 4.58: Relationship between Poisson's ratio and axial strain

Jinlong et al [22] considers Poisson's ratio in three segments. Firstly, between 0 to $0.3f_c \approx 0.4f_c$, the Poisson's ratio is considered to be approximately constant, from $0.3f_c$ - $0.9f_c$, the Poisson's ratio assumes the shape of a second order polynomial and lastly the from $0.9f_c$ to X_b , can assume the shape of a third order polynomial. X_b is the stress at which the volumetric strain is zero. Volumetric strain is the ratio of the change in volume at the deformation stage to the original volume of the specimen. Jinlong et al [22] deduces an equation for volumetric strain showing a relationship between axial strain, lateral strain and volumetric strain. Volumetric strain, ε_V is defined as the two times the lateral strain plus the axial strain 4.39.

$$\varepsilon_V = 2 \times \varepsilon_L + \varepsilon_A \tag{4.39}$$

From Figure 4.59, the relationship between Poisson's ratio and axial strain of specimen 1 for segments within the interval $0.3f_c$ - $0.9f_c$ and $0.9f_c$ to X_b were obtained from graph fitting curve using second order and third order polynomial respectively. The zero volumetric strain occurred when the axial strain had

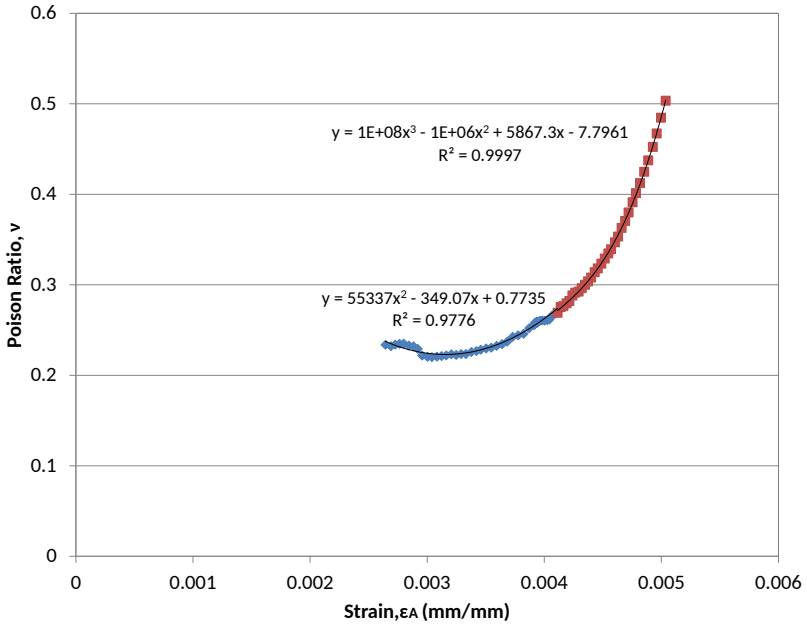

Figure 4.59: Proposed relationship between Poisson's ratio and axial strain

reached approximately 0.005 mm/mm at a a stress of 30.6 MPa. The Poisson's ratio within these two intervals are defined as cracking Poisson's ratio by Jinlong et al [22].

For the descending region on the stress strain curve, a relationship between non-linearity index and expansion ratio is developed as shown in Figure 4.60.

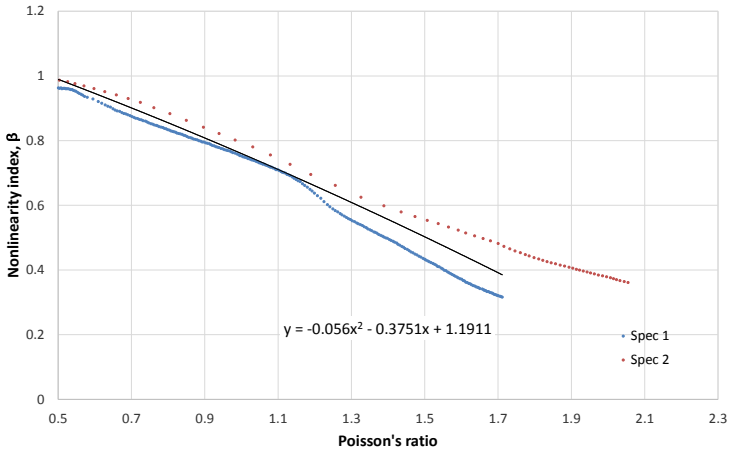

Figure 4.60: Proposed relationship between expansion ratio and nonlinearity index

The equation derived to model the descending curve is given in equation 4.40 This was obtained by taking the average of the curve fitting equations of the two specimens.

$$\beta = -0.056\nu^2 - 0.375\nu + 1.191 \tag{4.40}$$

Chapter 5

Conclusion

5.1 Conclusion

Corrosion of reinforcements in old buildings like historic reinforced concrete buildings is inevitable. This thesis researches on the effects of natural corrosion on the earthquake behavior of existing RC buildings. This study encompassed both the theoretical and experimental work. The experimental work was done on a 15 year old 1/3 frame to study the possible changes that exist on load carrying capacity, energy dissipation capability, damping rate and the stiffness of the frame. It is important to note that the test specimen was made of sea sand and gravels and mild steel for reinforcing the concrete and it has been subjected to natural corrosion in open field. On the theoretical methodology side of this study a computer program based on displacement method was developed to analyze the structural response of the model. The main conclusions of the study on are summarized as follows:

i) Contrary to the expectations even after 15 years, the corrosion observed in the specimens was minimal, the structural behavior when compared to the reference frame was minimal as well.

ii) Natural corrosion is a gradual process.The corrosion observed in this analysis was very minimum after 15 years under natural environmental conditions. Hence accelerated corrosion experiments cannot be used to study the behaviour of on-shore structures.

iii) Age has an effect on the compressive strength of concrete and concrete core extraction and Schmidt hammer readings helps to estimate the concrete strength of existing buildings.

iv) The load bearing capacity of 15 year old corroded structure is not very much affected but the displacement ductility is reduced.

v) Based on the comparison with the reference frame, corrosion has an effect on the energy dissipation capacity and the rotation capacity of the column ends of structures. The empirical relationship

vi) The experimental results revealed that the stiffness of the corroded frame is lower at the elastic state compared to the frame with no corrosion.

In the theoretical part of this thesis, analytical models were developed by existing computer programs and a developed computer algorithm to determine the capacity curve of the structure. Conclusion through theoretical and parametric works:

i) The analytical results obtained from SeismoStruct indicates the ultimate load capacity is equivalent to that obtained through the experimental works but it could not capture the target displacement of the ultimate base shear. The model showed a high lateral stiffness at the onset of the cyclic loading compared to the experimental results. Most of the damage states agree with the damage states observed in the experimental work. SAP2000 was able to define the structural performance under cyclic loading.

ii) The capacity curves of the pushover analysis attained through SAP2000 and DC2B was compared with the results of the developed computer programs.

The analytical results indicate that the adapted computer algorithm could be used in the analysis of nonlinear static analysis. The type of idealized moment curvature affects the structural response.

iii) Force-controlled incremental load analysis cannot capture the post elastic response of the structure while displacement-controlled incremental loads acn capture the nonlinear behaviour of structures.

iv) Plastic deformation affects the margin of safety against local or global buckling. The buckling safety factor decrease as hinges form at sections.

v) Considering the period of the structure, as hinges form due to plastification, the period increases meaning the natural frequency of the structure decrease, hence attracting less seismic force due to the low spectral acceleration.

vi) Parametric work on the length of the plastic hinge indicates that the smaller the length, the higher the structural stiffness but the smaller the ultimate displacement.

vii) Mechanical properties of materials has an effect of the structural response. Increase in concrete quality and reinforcement quantity has a beneficial effect on moment capacity. Higher reinforcement strength also means lower sectional ductility if the reinforcement ratio is not reduced. High reinforcement quantity increses the strength but does not significantly affect sectional ductility.

viii) For a strong beam weak column analysis, imposing cracked rigidity in the beam does not affect the structural response on the other hand, analysing a structure by using the effective rigidity for the columns, the structural ductility is increase.

References

[1] D. Amry, H. Hidenori, S. Yasutaka, and Y. Daisuke, "Deterioration progress and performance reduction of 40-year-old reinforced concrete beams in natural corrosion environments," *Construction and Building Materials*, vol. 149, pp. 690–704, 2017. [Online]. Available: http://www.sciencedirect.com/science/article/pii/S0950061817310620

[2] H. Jiang, "Seismic pefrormance of corroded reinforced concrete moment-resistance frames," *Journal of Civil & Environmental Engineering*, vol. 8, 2018. [Online]. Available: https://www.omicsonline.org/proceedings/seismic-performance-of-corroded-reinforced-concrete-momentresistingframe-structures-973 html

[3] Fib, "Bond of reinforcement in concrete," *Federation internationale du beton, Lausanne. State of the art report,prepared by Task Group Bond Models*, 2000.

[4] I. Saether, "Bond deterioration of corroded steel bars in concrete," *Structure and Infrastructure Engineering*, vol. 7, pp. 415–429, 06 2011.

[5] D. C. Candappa, J. Sanjayan, and S. Setunge, "Complete triaxial stress-strain curves of high-strength concrete," *Journal of Materials in Civil Engineering - J MATER CIVIL ENG*, vol. 13, 06 2001.

[6] F.-Y. Yeh and K.-C. Chang, "Size and shape effect on frp confinements for rectangular concrete columns," 02 2019.

[7] K. Tuutti, "Corrosion of steel in concrete," Ph.D. dissertation, 01 1982.

[8] P. Broomfield, *Corrosion of steel in concrete: understanding, investigation ang repair*. Taylor and francis, 2007.

[9] S. Popovics, "A numerical approach to the complete stress-strain curve of concrete," *Cement and Concrete Research*, vol. 3, no. 5, pp. 583 – 599, 1973. [Online]. Available: http://www.sciencedirect.com/science/article/pii/0008884673900963

[10] J. B. Mander, M. J. N. Priestley, and R. Park, "Theoretical stress‐strain model for confined concrete," *Journal of Structural Engineering*, vol. 114, no. 8, pp. 1804–1826, 1988. [Online]. Available: https://ascelibrary.org/doi/abs/10.1061/%28ASCE%290733-9445%281988%29114%3A8%281804%29

[11] M. Quraishi, D. Nayak, R. Kumar, and V. Kumar, "Corrosion of reinforced steel in concrete and its control:An overview," *J Steel structures and construction*, vol. 3, p. 214, 2017.

[12] L. Bertolini, B. Elsener, P. Pedeferri, and R. Polder, *Corrosion of steel in concrete prevention, diagnosis, repair*. Wiley-VCH, 2013.

[13] H. Böhni, *Corrosion in Reinforced Concrete Structures*, 01 2005.

[14] E. Hussain, A. Al-Gahtani, and R. , "Chloride threshold for corrosion of reinforcement in concrete," *ACI Materials Journal*, vol. 93, pp. 534–538, 11 1996.

[15] G. Loreto, M. Di Benedetti, R. Iovino, A. Nanni, and M. A. Gonzalez, "Evaluation of corrosion effect in reinforced concrete by chloride exposure," in *Nondestructive Characterization for Composite Materials, Aerospace Engineering, Civil Infrastructure, and Homeland Security 2011*, vol. 7983, Apr. 2011, p. 79830A.

[16] A. Verma, "Evaluation of sea sand and river sand properties and their comparison," 11 2015.

[17] R. Mahendran, K. Godwin, T. Gnana Selvan, and M. Murugan, " Experimental study on concrete using sea sand as a fne aggregate," *International journal of scientific and engineering research*, vol. 7, pp. 49–52, May 2016.

[18] İsmail H. Çağatay, "Experimental evaluation of buildings damaged in recent earthquakes in turkey," *Engineering Failure Analysis*, vol. 12, no. 3, pp. 440 – 452, 2005. [Online]. Available: http://www.sciencedirect.com/science/article/pii/S1350630704001165

[19] Y. Ma, Z. Guo, L. Wang, and J. Zhang, "Experimental investigation of corrosion effect on bond behavior between reinforcing bar and concrete," *Construction and Building Materials*, vol. 152, pp. 240 – 249, 2017. [Online]. Available: http://www.sciencedirect.com/science/article/pii/S0950061817313107

[20] H. Lin and Y. Zhao, "Effects of confinements on the bond strength between concrete and corroded steel bars," *Construction and Building Materials*, vol. 118, pp. 127 – 138, 2016. [Online]. Available: http://www.sciencedirect.com/science/article/pii/S0950061816307632

[21] K. Zandi, D. Coronelli, and K. Lundgren, "Bond capacity of severely corroded bars with corroded stirrups," *Magazine of Concrete Research*, vol. 63, pp. 953–968, 12 2011.

[22] J. Long Pan, J. Jia Zhou, Z. Li, and C. Leung, "A novel constitutive model for concrete under uniaxial compression," *Materials Science Forum - MATER SCI FORUM*, vol. 650, pp. 47–55, 05 2010.

[23] P. Inci, "Retrofitting of vulnerable reinforced concrete frames with shotcrete walls," Ph.D. dissertation, Istanbul Technical University,(ITU), 2009.

[24] TSC, "Turkish code for earthquake resistant design,Specification for Structures to be Built in Disaster Areas," Turkish Ministry of Public Works and Settlement, Turkey, Standard, 2007.

[25] BS1881-120, "Testing Concrete Method for Determination of Compressice Strength of Concrete Cores," British Standards Institute, London, Standard, 1983.

[26] ACI-Committee-214, "Guide for obtaining core and interperating compressive strength results (ACI 214.4R–10)," American Concrete Institute, 38800 Country Club Drive Farmington Hills, MI 48331,USA, Standard, June 2010.

[27] M. Ispir, K. Dalgic, C. Sengul, F. Kuran, A. Ilki, and M. A Tasdemir, "Modulus of elasticity of low strength concrete," 09 2010.

[28] TS500, "Requirements for design and construction of reinforced concrete structures ," Tuskish Standards Institute, Turkey, Standard, 2000.

[29] FEMA440, "Improvement of Nonlinear Static Seismic Procedures , ATC-55 Draft," Washington,USA, Standard, 2005.

[30] H. Krawinkler, A. Gupta, R. Medina, and N. Luco, "Development of loading histories for testing steel beam-to-column assemblies," no. CA 94305-4020, August 2000.

[31] N. Gibson, A. Filiatrault, and A. Ashford, " PEER 2002/24, Performance of Beam to Column Bridge Joints Subjected to a Large Velocity Pulse," April 2002.

[32] M. J. N. Priestley, G. Calvi, M. Kowalsky, and G. H. Powell, "Displacement-based seismic design of structures," *Earthquake Spectra - EARTHQ SPECTRA*, vol. 24, 05 2008.

[33] H.-S. Lee, T. Kage, T. Noguchi, and F. Tomosawa, "An experimental study on the retrofitting effects of reinforced concrete columns damaged by rebar corrosion strengthened with carbon fiber sheets," *Cement and Concrete Research*, vol. 33, no. 4, pp. 563 – 570, 2003. [Online]. Available: http://www.sciencedirect.com/science/article/pii/S0008884602010049

[34] Seismostruct, *A computer program for static and dynamic nonlinear analysis of framed structures*, 2018. [Online]. Available: http://www.seismosoft.com

[35] K. Dowell Robert, F. Seible, and L. Wilson Edward, " Pivot Hysteresis Model for Reinforced Concrete Members," *ACI– Structural journal*, vol. 95, pp. 607–617, 09 1998.

[36] A. Bal, E. Yuksel, and F. Karadogan, "Evaluation of a macro model proposed for a non-symmetrical precast beam to column connection," 2014.

[37] M. Inel and H. B. Ozmen, "Effects of plastic hinge properties in nonlinear analysis of reinforced concrete buildings," *Engineering Structures*, vol. 28, no. 11, pp. 1494 – 1502, 2006. [Online]. Available: http://www.sciencedirect.com/science/article/pii/S014102960600068X

[38] FEMA356, "Prestandard and Commentary for the Seismic rehabilitation of buildings ," Washington,USA, Standard, 2000.

[39] M. Priestley and T. Paulay, *Seismic design of reinforced concrete and masonary buildings*. John Wiley and Sons, INC, 1992.

[40] "Caltrans seismic design criteria, version 1.4," Tech. Rep. [Online]. Available: http://www.dot.ca.gov/hq/esc/techpubs/manual/othermanual/other-engin-manual/seismic-design-criteria/sdc.html

[41] R. Hasan, L. Xu, and D. Grierson, "Push-over analysis for performance-based seismic design," *Computers & Structures*, vol. 80, no. 31, pp. 2483 – 2493, 2002. [Online]. Available: http://www.sciencedirect.com/science/article/pii/S0045794902002122

[42] Z. H. Yan and F. T. K. Au, "Nonlinear dynamic analysis of frames with plastic hinges at arbitrary locations," *The Structural Design of Tall and Special Buildings*, vol. 19, no. 7, pp. 778–801, 2010. [Online]. Available: https://onlinelibrary.wiley.com/doi/abs/10.1002/tal.513

Appendix A

Preparatory Works

Reinforced concrete structures often shows nonlinear behavior because of the nonlinear stress-strain relationship of its materials. Structural ductility is the degree to which a structure can undergo deformations until failure or without a huge reduction in the flexural capacity. This extent of deformation depends on the sectional ductility which is the shape of the moment-curvature. Constructions in earthquake prone regions, the main objective is to ensure that the structure undergoes high displacements without complete collapse of the building that is the reason for the importance of ductility. The main objective is to determine the factors that affect the moment curvature relationship (flexural capacity) which in turn affects the ductility of a T-section Reinforced concrete beams. The parametric analysis performed considers the effect of concrete quality, flange width, reinforcement quality and quantity of reinforcement. Using DC-2B computer program, an algorithm was developed for this analysis.

A.0.1 Properties of Concrete and Reinforcing Steel

The major constituents of RC are concrete and steel. Concrete used for its compression properties and it is important to define the right stress-strain relationship. Many models have been developed for both confined and unconfined

concrete but before the constructions, uniaxial compressive test is commonly performed to know the yield and ultimate compressive strength of the concrete. The stress strain curve of concrete is similar for all concrete but the shape at the peak stress can take many forms depending on its strength but mostly it begins with a linear increase which is the elastic region and later begins to curve (nonlinear region) which occurs when cracks extend to the surface of the concrete. After the ultimate compressive capacity is attained, it decreases with a negative slope. The behavior of concrete is often represented by a second-degree parabola for both the ascending and descending branch. The present stress-strain curve utilized in this parametric work is parabolic until the peak strength and after the strength is kept constant as shown in FigureA.1(a) with yield and ultimate strain of the concrete is taken as 0.002 and 0.004.

Reinforcement is known for its good tensile properties. The stress-strain curves

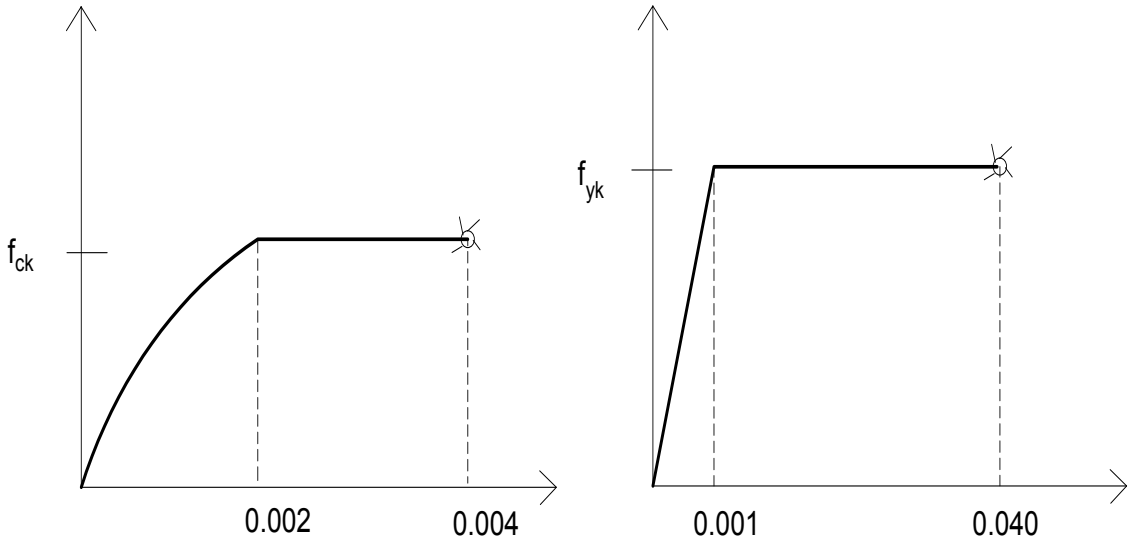

Figure A.1: a)Concrete stress-strain relationship b)Reinforcement stress-strain relationship

for reinforcing steel bars used in structures all have almost the same curve. It starts with the linear elastic region, the yield and strain hardening. The bi-linearized elastic perfectly plastic stress strain relationship was considered for the reinforcements given in Figure A.1(b)

The cross-section of the T-beam used in this analysis is shown in Figure A.2.

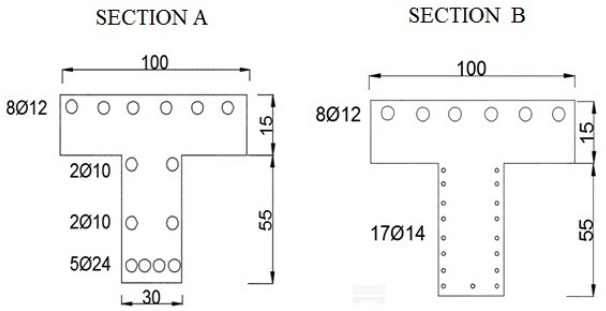

Figure A.2: Cross-section of RC T-beam

Double reinforcements together with be reinforcement were considered according to the specifications of Turkish building code. The width of the flange is 1m, beam width is 0.3m, flange height is 0.15 and total beam height is 0.7m. The material properties are concrete crushing strength, 30 MPa, concrete crushing strain 0.002, ultimate concrete strain 0.004, yield strength of steel 420 MPa and yield strain of steel 0.001.

A.0.2 Moment Curvature Response of RC

A typical moment curvature shows the first cracking and the first yielding. After cracking the slope decreases as observed. Theoretical moment-curvature (M-curvature) curves for RC sections under flexure can be derived on the assumptions used in the material models. The rigidity of a section at any intensity of internal moment can be obtained directly from the moment-curvature diagram . As the internal moment of a section increases, cracking of the concrete reduces the flexural rigidity of the sections. The curvature is directly related to the depth of the neutral axis, hence with a change in internal moment intensity, the depth neutral axis changes causing different curvatures. An already built up computer program was used to obtain the moment curvature and the depth of neutral axis. A hand calculation was performed to verify the authenticity and accuracy of the computer program. With the hand calculation, for a given curvature, the depth

of the neutral axis can be determined by trial and error. Firstly, the depth of the neutral axis is assumed and the strain and stress at different points of the sections was calculated and the compressive and tensile forces were equalized. After the neutral axis depth is determined, the moment, M can be calculated by summing the moments of all forces on the section.

A.0.3 Effect of Reinforcement Quantity

The effect of the quantity of reinforcement is studied in this section. Using section A for this analysis, the quantity of both the bottom and top reinforcement are increased as shown in Table A.1.

The sectional ductility $\eta = X_u/X_y$, where X_u is the ultimate curvature and X_y is the yield curvature and the moment index is defined as the fraction of ultimate moment over yield moment. With an increase in bottom reinforcement, the positive moment capacity increases. For 20% increase in the bottom reinforcement, the moment capacity increased approximately 18% compared to section A and 40% increase in bottom reinforcement caused a 35% increase in moment capacity. It is observed that an increase in the top reinforcement does not alter the moment capacity. The ductility of the section is not really affected by the quantity of the reincorcement.

Beam	Percentage increase (bottom)	Percentage increase (top)
B-I	0%	0%
B-II	20%	0%
B-III	20%	10%
B-IV	40%	0%
B-V	40%	20%

Table A.1: Percentage Increase of Reinforcement Ratio in T-section Beam

Considering a beam section subjected to negative moment, the increase in top reinforcement affects the moment capacity considerably. From Figure A.3, it can

be observed that the increase in the bottom reinforcement did not alter the moment capacity of section A but an increase in the top reinforcements (B-III and B-V) increased the moment capacity and the yield moment, but the ductility and the moment index are negligibly affected.

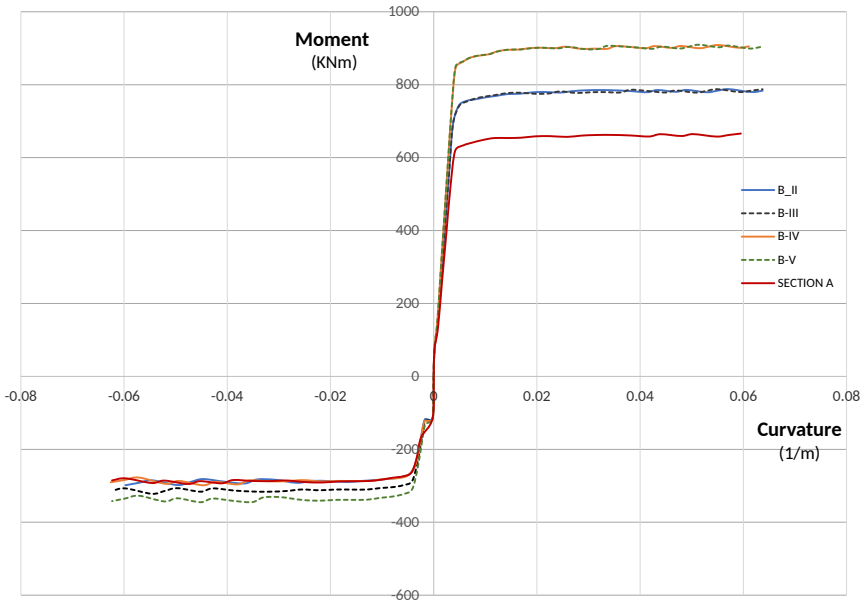

Figure A.3: The effect of reinforcement ratio on the beam capacity

A.0.4 Effect of Concrete Quality

To investigate the effect of Concrete quality on sectional ductility and moment capacity, concrete classes of C25, C30 and C35 were utilized. Maintaining all sectional properties of Section A, the concrete quality was changed to determine its effects. The sectional ductility was defined as the curvature ductility $\eta = X_u/X_y$, where X_u is the ultimate curvature and X_y is the yield curvature and the moment index is defined as the fraction of ultimate moment over yield moment. Beams B-I, B-II and B-V were used in this study. The properties of the concrete classes were taken from TS500[28]. A summary of the analysis results is shown in table A.2. Concrete quality is seen to have minimal effect on the sectional moment capacity.The percentage increase in positive yield and ultimate moment is 0.116

and 1.12 respectively which is almost negligible. For the negative moment, the percentage increase for yield and ultimate moments is 1.2 and 3.32 respectively. The sectional ductility of the beam section is observed to increase with positive moment but decrease in negative moment as concrete quality increases. In the positive moment, the percentage increase in sectional ductility is 18.6% from C30 to C35 and the percentage decrease ın the sectional ductility is 3.32%.

The moment lever arm sometimes called the lever arm decreases with an increase in concrete quality in both positive and negative moment. The lever arm is the distance were both compressive and tensile forces act as a couple hence with an increase in the concrete quality, the compressive forces become higher than the tensile forces because only reinforcement are assumed to act in tension since concrete has a low tensile strength. The moment arm then has to decrease to balance out forces. In addition, moment arm is always higher for positive moment than in negative moment.

	S420 $F_w = 100cm$					
Concrete quality	$M_y{}^+$	$M_u{}^+$	$X_y{}^+$	$X_u{}^+$	c^+	η_+
30	590.8545	641.1018	0.004565	0.037736	0.21	8.27
35	591.54	648.2952	0.00443	0.043478	0.196	9.81

	S420 $F_w = 100cm$					
Concrete quality	$M_y{}^-$	$M_u{}^-$	$X_y{}^-$	$X_u{}^-$	η	C
30	264.098	285.215	0.03835	0.06234	16.26	0.1225
35	267.29	297.61	0.00379919	0.05974	15.72	0.11725

Table A.2: Effect of concrete quality on T-section beams

The major conclusions that can be made from this preparatory works include:

1. An increase in the compressive strength of concrete increases the moment capacity and the stiffness of the section.

2. The higher the strength of steel, the higher the moment capacity but the lower the sectional ductility

3. Increasing compressive strength of concrete does not significantly affect the ductility of the section.

4. The ductility of a section can be maintained by increasing the strength of the reinforcement but with a low reinforcement ratio.

Appendix B

Correction Martix for Semi-rigid Connections

The details of the correction matrix by Hasan etal [41] for modifying the member stiffness matrix is given in this appendix. For a structural element with six degrees of freedom, the correction matrix for a standard structural stiffness matrix in given in matrix form shown in equation B.1.

$$[C_e] = \frac{1}{4 - r_1 * r_2} \left[\begin{array}{c|c|c|c|c|c} e_{33} & 0 & e_{32} & 0 & 0 & 0 \\ \hline 0 & e_{11} & 0 & 0 & 0 & 0 \\ \hline e_{23} & 0 & e_{22} & 0 & 0 & 0 \\ \hline 0 & 0 & 0 & e_{66} & 0 & e_{65} \\ \hline 0 & 0 & 0 & 0 & e_{44} & 0 \\ \hline 0 & 0 & 0 & e_{56} & 0 & e_{55} \end{array}\right] \tag{B.1}$$

Where r_1 and r_2 are called the rigidity factors and L is the length of the member.

$$r_1 = \frac{1}{1 + \frac{3EI}{R_1 L}} \quad r_2 = \frac{1}{1 + \frac{3EI}{R_2 L}}$$

$$e_{11} = 4 - (r_1 r_2) \quad e_{23} = -2Lr_1(1 - r_2)$$

$$e_{22} = 4r_2 - 2r_1 + r_1 r_2 \quad e_{66} = 3r_2(2 - r_1) \tag{B.2}$$

$$e_{65} = 6/L(r_2 - r_1) \quad e_{44} = 4 - (r_1 r_2)$$

$$e_{56} = -2Lr_2(1 - r_1) \quad e_{55} = 4r_1 - 2r_2 + r_1 r_2$$

When considering the second order effect on the stiffness parameters for a structural member with a semi rigid connection, the following parameters are used to develop the geometic stiffness correction matrix.

$$[g_e] = \frac{1}{5(4 - r_1 * r_2)^2} \begin{bmatrix} g_{33} & 0 & g_{32} & g_{36} & 0 & g_{35} \\ 0 & 0 & 0 & 0 & 0 & 0 \\ 0 & 0 & g_{22} & 0 & 0 & 0 \\ g_{63} & 0 & g_{62} & g_{66} & 0 & g_{65} \\ 0 & 0 & 0 & 0 & 0 & 0 \\ 0 & 0 & 0 & 0 & 0 & g_{22} \end{bmatrix} \tag{B.3}$$

where;

$$g_{32} = -\frac{4}{L} \times ((8{r_1}^2 r_2) - (13 r_1 {r_2}^2) - (32{r_1}^2) - (8{r_2}^2) + (25 r_1 r_2) + 20) \tag{B.4}$$

$$g_{33} = r_1((16r_2^2) + (25 r_1 r_2^2) - (96 r_1 r_2) + (128 r_1) - (28 r_2)) \tag{B.5}$$

$$g_{63} = (4r_1)((16r_2^2) - (5 r_1 r_2^2) + (9 r_1 r_2) - (28 r_2) + (8 r_1)) \tag{B.6}$$

$$g_{66} = r_2((16r_1^2) + (25 r_1^2 r_2) - (96 r_1 r_2) + (128 r_2) - (28 r_1)) \tag{B.7}$$

$$g_{36} = 4r_2((16r_1^2) - (5 r_1^2 r_2) + (9 r_1 r_2) - (28 r_1) + (8 r_2)) \tag{B.8}$$

$$g_{62} = -(4/L) * ((8 r_1 r_2^2) - (13 r_1^2 r_2) - (32 r_2^2) - (8 r_1^2) + (25 r_1 r_2) + 20) \tag{B.9}$$

$$g_{22} = 5(4 - (r_1 r_2))^2) \qquad g_{35} = -g_{32} \qquad g_{65} = -g_{62} \tag{B.10}$$